# General size effect in the Hall-Petch effect and in micromechanical deformation

**Yuan Li**

**October 2016**

**School of Physics and Astronomy**

**Queen Mary University of London**

**Supervisors: Prof. David Dunstan and Dr. Andy Bushby**

**This is thesis is submitted in partial fulfilment of the requirements for the degree of Doctor of Philosophy from Queen Mary, University of London**

# Declaration

I, Yuan Li, confirm that the research included within this thesis is my own work or that where it has been carried out in collaboration with, or supported by others, that this is duly acknowledged below and my contribution indicated. Previously published material is also acknowledged below.

I attest that I have exercised reasonable care to ensure that the work is original, and does not to the best of my knowledge break any UK law, infringe any third party's copyright or other Intellectual Property Right, or contain any confidential material.

I accept that the College has the right to use plagiarism detection software to check the electronic version of the thesis.

I confirm that this thesis has not been previously submitted for the award of a degree by this or any other university.



Signature: Yuan Li

Date: 25/10/2016

# Abstract

This thesis is a study of the size effect. Improvements on both theoretical work and experimental design are involved in this thesis. The theoretical section focuses on the grain size effect, while the experimental section is related to the micro-foil bending test. Both classic experimental data and theories for the Hall-Petch relationship are reviewed comprehensively. The fitting of the datasets show that the inverse square-root dependence and simple inverse expressions are equally good. The fully Bayesian analysis strongly suggests that the latter is correct. Since the physical mechanism underlying the simple inverse dependence is a general size effect, the precise description of the Hall-Petch effect is that it is a manifestation of the general size effect, instead of having its own special character.

Improvements on the classic Stolken and Evans' micro-foil bending experiments are also carried out in this thesis. The smart design of the new equipment eliminates the big risk of error in the classic experiment. By using the new device, precise datasets from the elastic region through the yield point and to high plastic strain area can be obtained. The initial results correspond well with the old published data.

# Acknowledgements

Foremost, I would like to express my sincere gratitude to my supervisors, Prof. David Dunstan and Dr. Andy Bushby, for the encouragement, patient guidance and advice they has provided during my research in QM. Without their constant support my PhD project would not have been achievable. In particular, I would like to thank the beer every Tuesday evening. Cheers!

I would like to thank Geoff Gannaway and Geoff Simpson for fabricating micro-foil experimental devices, Dr. Ken Scott for technical help, George Nevill for sample preparation, Prof. William Gillin for RTA, Prof. Paul Anderson for the profilometer.

I extend my thanks to my colleagues Dr. Dong Dong, Dr. Yiwei Sun, Dr. Haizhou Lu and Dr Yuanpeng Zhang, Shankui Chang, Wenda Shi, Miao Gu, Luwei Yang, for their discussion and great help in my life in London. Especially, I would like to thank to Dr Dabiao Liu for the valuable suggestions on my thesis.

I must express my special gratitude to my wife, Shumeng Jiang, for her continued support, encouragement and unselfish dedication.

I would like to thank CSC scholarship for giving me the precious opportunity to study in the UK and their funding for my living expenses.

Finally, I would like to thank my family for their endless love.

# Table of Contents

# List of Figure Captions

Fig.1.15 The example of grain boundary ledge acting as donor of dislocations. (Reproduced from Y. Li & Dunstan)

Fig.1.16 Schematic illustration of slip distance model: dislocation slip length is less in a smaller grain, the dislocation density is higher. (Reproduced from Y. Li & Dunstan)

Fig.1.17 The effects of crystalline elastic or plastic anisotropy in forcing stress and strain gradients, in which anisotropic grains are subject to a homogenous stress field. (Reproduced from Y. Li & Dunstan)

Fig.2.1 Datasets for iron, steel and silicon steel are plotted against (a) the inverse square-root of grain size, (b) the simple inverse of grain size, and (c) in normalised form on a double logarithmic plot. The normalization constants: $Y$=211GPa, $a_0$=0.287nm. In (a), the solid lines are fits to Eq.2.1; in (b) the solid lines are fits to Eq.2.3 with the exponent $x$= -1; in (c) the solid lines are plots of Eq.2.2 with k = 0.72 and $\sigma_0$ chosen so the lines for each dataset are below most of the data. The heavy black line is for Eq.3.2 with $\sigma_0$ = 0. Fe(1) is the classic dataset of Petch (1953); Fe(2) represent the silicon steel datasets from Douthwaite and Evans (1973); Fe(3) is data from Agraie-Khafri et al. (2012); Fe(4) are data sets for 316L stainless steel from Kashyap and Tangri (1997); Fe(5) come from the EN2 steel datasets in Douthwaite (1970); Fe(6) represent data sets from Armstrong (1962); Fe (7) is the classic dataset of Hall (1951).

Fig.2.2 Datasets for brass are plotted against (a) the inverse square-root of grain size, (b) the simple inverse of grain size, and (c) in normalised form on a double logarithmic plot. The normalization constants: $Y$=115GPa, $a_0$=0.361nm. B(1) and B (2) are Bassett and Davis (1919) data for 68-32 and 69-31 brass; B (3) is Babyak (1960) data for 70-30 brass; B(4) are the Armstrong (1962) 70-30 brass data at yield stress and at 20% strain; B(5) are the data sets from Douthwaite (1970) for the yield stress and the flow stress at 5% and 7.5% strain. The solid curves are as in Fig.2.1.

Fig2.3 Data sets for copper are plotted against (a) the inverse square-root of grain size, (b) the simple inverse of grain size, and (c) in normalised form on a double logarithmic plot. The normalization constants: $Y$=115GPa, $a_0$=0.361nm. Cu(1) and Cu(2) are data sets from Hansen and Ralph (1982) liquid nitrogen temperature and room temperature at 5%, 10% and 20% strain, respectively; Cu(3) indicate the data for copper at 0.5% strain from Armstrong et al. (1962). The solid curves are as in Fig.2.1.

Fig.2.4 W Data for tungsten Vashi et al. (1970); Ti(1) Data from titanium Hu and Cline (1968); Cr Data is chromium Brittain et al (1985); Ti(2) Data reproduced from titanium Jones and Conrad (1969) are plotted against (a) the inverse square-root of grain size, (b) the simple inverse of grain size, and (c) in normalised form on a double logarithmmic plot. The normalization constants: for tungsten, $Y$=411GPa, $a_0$=0.316nm; for chromium, $Y$=279GPa, $a_0$=0.228nm; for titanium, $Y$=116GPa, $a_0$=0.295nm. The solid curves are as in Fig.2.1.

Fig.2.5 (a) The reproduced original Hall-Petch type plot of flow stress for Ni data. (b) The linear fitting of both the mechanical flow stress data and electrical resistivity method data. The black filled circles indicated the flow stress data points of (a), the red filled circles represented the electrical resistivity measurements data which reproduced from the Fig.5 and Fig.8 of the original reference, 10% and 20% strain at 77K data were reproduced.

Fig.2.6 The $k_{HP}$ values were plotted against square root strain from the data of Table 2.5. The red filled circles are low strain data, the red crosses are high strain data, and the black line is linear relationship indicated by Eq.13 of Narutani's paper.

Fig.2.7 Data for silver, gold and nickel are plotted against (a) the inverse square-root of grain size, (b) the simple inverse of grain size, and (c) in normalised form on a double

logarithmic plot. The normalization constants: for silver, $Y$=83GPa, $a_0$=0.409nm; for gold, $Y$=79GPa, $a_0$=0.408nm; for nickel, $Y$=200GPa, $a_0$=0.352nm. Ag(1) and Ag(2) indicated the silver data of Aldrich and Armstrong (1970) at 20% strain and yield stress; Ni(1) is the data set of Thompson (1977); Ni(2) from Keller and Hug (2008); Ni(3) from Narutani & Takamura (1991). The solid curves are as in Fig.2.1.

Fig.2.8 Data for aluminium are plotted against (a) the inverse square-root of grain size, (b) the simple inverse of grain size, and (c) in normalised form on a double logarithmic plot. The normalization constants: $Y$=70GPa, $a_0$=0.316nm. Al(1) and Al(2) are from Hansen (1977) for 99.5% and 99.999% aluminium at 0.2, 1, 5, 10, 20% strain at room temperature; Al(3) show the Carreker and Hibbard (1957) aluminium data; Al(4) are the data of Tsuji et al. (2002); Al(5) and Al(6) come from Yu et al. (2005) at 77K and at room temperature, respectively. The solid curves are as in Fig.2.1.

Fig.2.9 Normalised datasets from the literature for flow or yield stress against grain size. The heavy line in all panels is for Eq.2.2 with k = 0.72 and $\varepsilon_0$ = 0. The thin solid lines are for Eq.2.2 with k = 0.72 and $\varepsilon_0$ as the only fitting parameter. The black dashed lines are fits using Eq.2.3 with x = 1, k and $\varepsilon_0$ as fitting parameters. The black chain-dotted lines are fits using Eq.2.1, normalised, so that kHP and $\varepsilon_0$ are the fitting parameters. The purple solid lines are the minimum strength predicted by the Eq.2.8 with the yield strain equal to 0.002. The purple chain-dotted lines are Eq.2.8 at yield strain plus the elastic strain which describe the bulk strength. The red heavy line and chain-dotted line in Fig. iv come from Eq.2.8 with the plastic strain equal to 0.04. The dark yellow line in Fig. v is the plot of Eq.2.4 at 20% strain.

Fig.2.10 The probability distribution of Eq.2.2 and Eq.2.8 in the log$\sigma_0$–log$d$ space. In (a), the Eq.2.2 have a probability density of 1 for datasets above the $d^{-1}$ line (black heavy line) and 0 for data dramatically below the $d^{-1}$ line. In (b), for the Eq.2.8, the relative probability density above the $d^{-1}$ line is 0.7 due to 0.3 of the gap between

modified Ashby theory (purple chain-dotted line) and CTT theory (black heavy line).

Fig.2.11. The schematic of the four classic models: (a) Dislocation pile-up model, (b) Grain boundary source model, (c) The slip distance model, (d) The GNDs and elastic anisotropy model.

Fig.2.12. (a) The predictions of the pile-up model (Eq.2.8) (heavy black line), the grain-boundary ledge model (Eq.2.10) (dashed blue lines indicating the range of the upper limit of the predictions) and the slip-distance model, Eq.2.12 (chain-dotted red lines) are compared with the data. The depth of shading indicates schematically the probability according to these models that data will fall in the various regions; white corresponds to a probability close to zero. In (b), the Hall-Petch slopes are plotted against the normalised anisotropy factor. The large data points indicate that only one data set is available for a metal; the small data points represent many results for the same metal. The red filled circles indicate the yield datasets. The solid black line is a least-squares fit of $y = ax + b$ to the averaged data and the dashed blue line a fit of $y = ax$ as described in Section 2.4.4.

Fig.2.13. (a) The schematic of Eq.2.2 plots against the inverse square root abscissa. The black heavy parabola represents the Eq.2.2. The three regions datasets in different ranges of grain size are shown by different colours: large (L), mid-point (M) and small (S) grains region, which are represented by blue, green and red, respectively. Fitting to the large-grain-size dataset (L, blue) will give the blue straight line with a small slope $k_{HP}$, while fitting to the green (M) and red (S) datasets with medium and small grain sizes will give the green and red straight lines with larger slopes (larger values of $k_{HP}$). (b) This is an example from the data of Emery's gold films tension experiment. The blue dashed line is the best fit parabola of Eq.2.2. The black solid straight line is the Hall-Petch fitting of Eq.3.1. The red solid line is fitting with the upper and lower halves of the dataset.

Fig.2.14. The normalised HP factors are plotted against the normalised average grain size.

Fig.2.15. Normalised values of $k_{HP}$ for the data from the pure metal datasets are plotted against the normalised inverse square root of grain size. The heavy black line indicates that the smaller grain size datasets have a higher value of the $k_{HP}$.

Fig.3.1. Schematic of the Stolken and Evans' micro-foil bending equipment. (a) mounted the foil, (b) load process, (c) unload (elastic recovery). (Reproduced from Stolken)

Fig.3.2. Schematic of the calculation of stress-strain behaviour from measured bend radii. (Reproduced from Stolken)

Fig.3.3 The normalized bending moment were plotted against the surface strain for all three foil thickness ranging from 12.5 to 50μm . (Reproduced from Stolken and Evans)

Fig.3.4 Schematic of the 4-Point micro-foil bend rig reproduced from P.Moreau, M.Y.P'ng. The red line is thin metal foil, which is restricted on the shim by two weighted bars on both side.

Fig.4.1 Schematic of the load-unload formers bend rig. (a) Introduction of the different components of the rig. (b) (c) show the details of how to control the wedge and former.

Fig.4.2 (a) The top-view of the cover plate is shown. The middle part is removed to expose the foil. (b) The shape of the load rubber.

Fig4.3 Schematic of the two face mode of the rig. In (a), the flat foil is measured

horizontally. In (b), the whole profile couldn't be obtained since the measurement on the end of the foil exceed the height limitation. In (c), with the rotation of the rig, the full information could be obtained.

Fig.4.4 (a) The profilometer used in the surface profile measurement. (b) Schematic of the optical profilometer. There is a measuring range of profilometer.

Fig.4.5 (a) 3D plot of the surface profile of No.7# Former (low strain). X-axis is scan length in mm, Y-axis is the different scanned line, Z-axis is the height of the surface profile in μm. (b) Fitting of each line of data. The light blue line is the measured surface profile data, while the red line from the fitting of Mathematica© software. (c) The deviations check of the fitting demonstrates the fitting is relatively accurate.

Fig.4.6 The Mathematica fitting of the surface profile of No.14# Former (high strain). The fitting to the profile is focus on the circle component, two fitting tangent lines are used to determine the cutting range of the profile data.

Fig.4.7 Schematic of the main components of the RTA. The foil samples are placed between two graphite strips and the temperature is measured and controlled by optical thermocouple. The samples are annealed in either high vacuum environment or inert Nitrogen gas atmosphere to prevent oxidation.

Fig.4.8 Schematic of the load-unload bending test process. (b) is the zoom in detail of the foil. Since the former and thin foil fully contact, load radius is the former radius $R_1$. The foil is then unloaded, it elastically recover to a larger radius $R_2$.

Fig.4.9 The examples of SEM images of the annealed Ni foil samples. (a) The 125μm thickness, annealing temperature 1000ºC, annealing time 5s. (b) The 50μm thickness, annealing temperature 700ºC, annealing time 30s.

Fig.4.10 The measured surface profile of the unload sample. X-axis is the scan length of the sample in mm, Y-axis is different scan of the sample. Z-axis represented the profile in micron.

Fig.4.11 (a) The normalized bending moment was plotted against the surface strain. The red data is the new data, the blue data is the old published data. The sample thicknesses of filled squares, circle, triangle and cross are 10μm, 50μm, 50μm and 125μm, respectively. Thinner foils are stronger than thicker foils.

# Introduction

Smaller is stronger. This is the so called size effect. The size effect is that the mechanical properties of materials depends on the size dramatically when the size is below 100 microns. The strength of a material increases when the size decreases. The term of "size" here represents the general definition of the material size, it includes both the external sample dimension and the internal structure size e.g. the grain size[1]. The research of this thesis can be divided into two sections: (1) A review on both the experimental evidence and the models related to Hall-Petch dependence is investigated; (2) A brilliant micro-foil bending test method based on the load-unload measurement is designed and fabricated.

This thesis is composed of 5 Chapters. Chapter 1 is the comprehensive literature review on both the experiments and the theories related with my research. Chapter 2 is the investigation on the Hall-Petch dependence. Chapter 3 is the literature review particular on the foil bending experiments. Chapter 4 describes design and fabrication of the new micro-foil bending test method based on the load-unload measurement. Chapter 5 is summary.

# 1. Literature review

In this chapter, the size effect in experimental observations are introduced firstly. The external size effect experimental evidences include both inhomogeneous and homogeneous deformations, the internal size effect experiments are mainly focused on the grain size effect, i.e. the Hall-Petch effect. Then the theories on the general size effect and the models related to the Hall-Petch effect are reviewed.

Before the classic experiments review, some key concepts related to material mechanical properties should be reviewed.

## 1.1 Key concepts

### 1.1.1 SSDs and GNDs

It is experimentally found that many two-phase alloys are much stronger than pure single crystals. In 1970, Ashby [2] proposed the GND model to explain it. When a material is deformed, dislocations are generated and moved. Dislocations are trapped and form obstacles to prevent the further motion. This is the reason of hardening. If the mobile dislocations trapped randomly, such trapped dislocations are referred to as statistically stored dislocations (SSDs). The conventional Taylor hardening model [3] is based on the SSDs. However, if the materials deform with inhomogeneous strain i.e. the plastic deformation occurs with plastic strain gradients, the values of the plastic strain varies with position. Hence, dislocation will appear to accommodate this non-uniform deformation. These are the so called geometrically necessary dislocations (GNDs). The plastic strain gradient is achieved by introducing of GNDs into the crystal, the density of GNDs are proportional to the strain gradients.

Take the plastic bending of a single crystal as an example to explain GNDs, as shown in Fig.1.1. We consider a crystal is of length $l$ and thickness $t$ before the deformation (Fig.1.1a). Then the crystal is bent to a radius of $R$, the angle of the arc is $\theta$ (Fig.1.1b). The different sections of the crystal undergo the various strain: the strain of the middle

plane of the bar is zero; the upper part of the crystal is deformed as a tension behaviour, i.e. the length of the upper surface is increased $\delta l$; conversely, the lower part of the crystal is deformed as a compression behaviour, the length change of the lower surface is negative $\delta l$. Hence, the total length difference is $2\delta l = t\theta$, the strain difference between the two surfaces is $2\delta l/l$. The strain gradient is this strain difference divided by the thickness $t$:

$$\text{Strain gradient} = 2\frac{\delta l}{lt} = \frac{t\theta}{lt} = \frac{\theta}{l} \tag{1.1}$$

The number of atomic planes in the crystal is the length divided by the Burgers vector $b$. In plastic strain, the difference in the number of atomic planes between the surfaces is:

$$\Delta n = \frac{2\delta l}{b} \tag{1.2}$$

This difference number is accommodated by introducing the GNDs. The density of the GNDs is then expressed as:

$$\rho_G = \frac{\Delta n}{lt} = \frac{2\delta l}{blt} = 2\frac{\delta l}{lt}\frac{1}{b} = \frac{\text{Strain Gradient}}{b} \tag{1.3}$$

By considering the difference between the orientation of the slip plane and direction of the bending axis, Eq.1.3 will be changed to:

$$\rho_G = \alpha\frac{\text{Strain Gradient}}{b} \tag{1.4}$$

where $\alpha$ is a constant of order unity, $b$ is the Burgers vector.

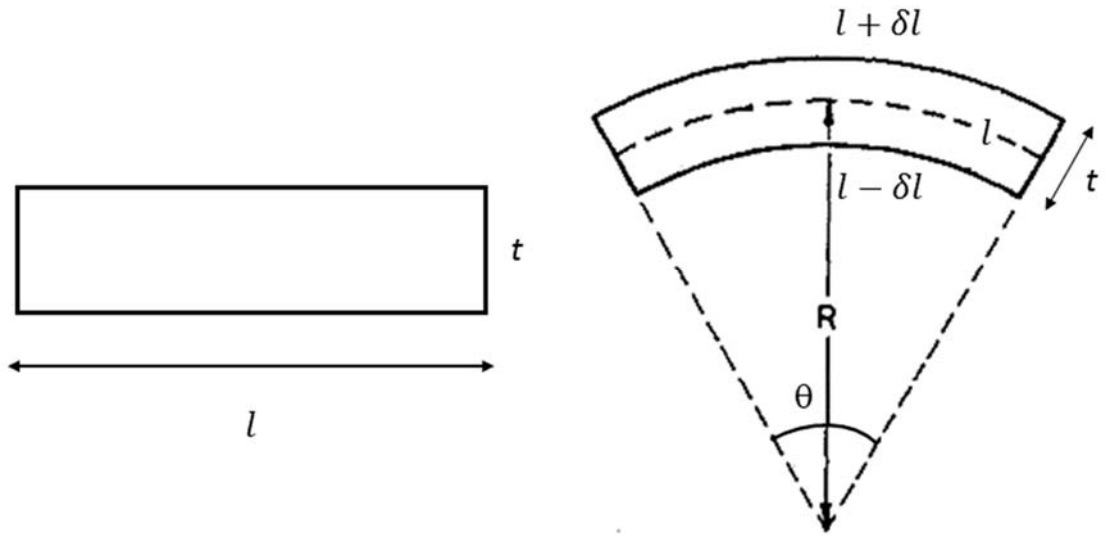


**(a)** **(b)**

**Fig.1.1 Plastic bending of a crystal of length l and thickness t to a radius of R. This bending process will produce a tensile strain on the upper surface and a compressive strain on the lower surface. The strain gradient is accommodated by introducing GNDs into the crystal. (Fig.1.1b is partly reproduced from Fleck, 1994 [4])**

For two-phase alloys, the two phases deform differently. One component deforms more than the other, such alloys are plastically non-homogeneous. In this way, an additional density of GNDs will appear, increasing the total density of the dislocations, therefore making the material much stronger.

Further, poly-crystals of pure metals are also plastically inhomogeneous even under uniform deformation, the mechanism is shown in Fig.1.2. In Fig.1.2 (a), each grain of a poly-crystal has a random orientation, while the tensile strain is uniaxial. Because of the random orientations, each grain will slip in a different direction under the uniaxial strain, then overlap and voids will appear, the grain boundary will correct overlaps or voids, then GNDs are formed.

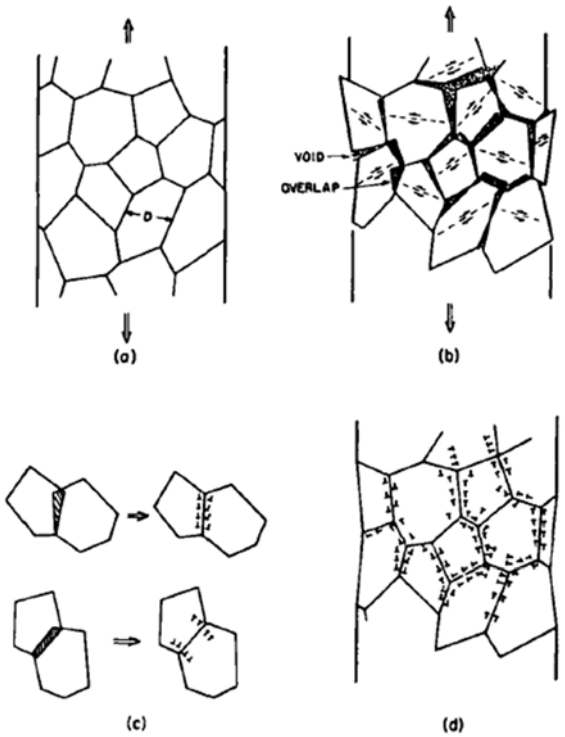


**Fig.1.2 Schematic diagram of GNDs (Reproduced from Ashby, 1970 [2])**

## 1.1.2 Finite size effect on strain hardening

In 1942, ten years before the famous Hall-Petch equation was established, in order to explain the strain hardening, Bragg [5] proposed that the strength is inversely proportional to the grain size. It is generally observed that the effect of plastic deformation by strain hardening is to disintegrate the crystalline grain into much smaller crystal fragments. Hence, during the strain hardening, with the deformation increased, the increase strength of the metal can be attributed to a corresponding decrease of the size of fragments. For simplicity, Bragg supposed a fragment to be a cube of volume $V$ and side $t$, it is also supposed that the general shear strain of the metal is parallel to the glide planes of the fragment. The displacement of the fragment is $x$, as shown in the Fig.1.3.

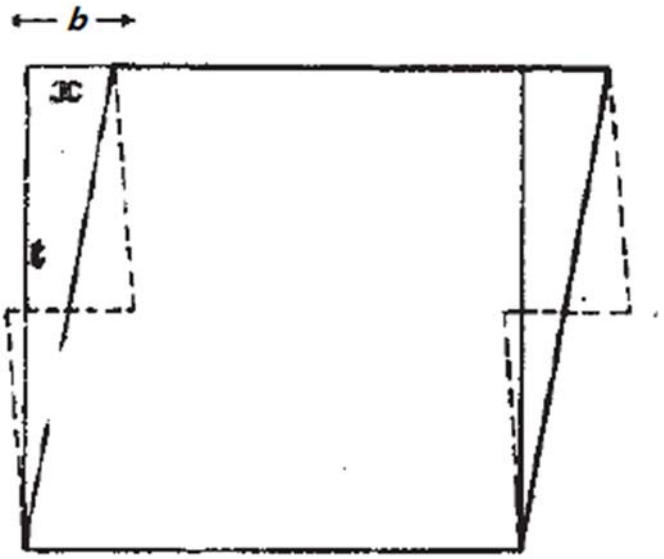


**Fig.1.3 Schematic diagram of deformed small fragment. (Reproduced from Bragg, 1942 [5])**

It may be considered that glide will occur in this fragment when the value of *x* reaches the magnitude of burger's vector *b*. The shear strain is

$$\varepsilon_s = \frac{b}{t} \tag{1.5}$$

where *t* is length of the fragment and therefore the grain size *d.*

All the fragments are subject to this condition. By multiplying the shear modulus G, the whole metal will withstand a shear stress

$$\tau_s = G\frac{b}{d} \tag{1.6}$$

According to Eq.1.6, the smaller grain size *d*, the strength of material will increase.

## 1.2 External size effects

In the past a few decades, the size effects have been observed in various experiments with different external geometric dimension include both inhomogeneous and homogeneous deformation. The experiment only be described here in this section, the theory will be reviewed later.

### 1.2.1 Inhomogeneous deformation experiments

The classic inhomogeneous deformation experiments are the wire diameter in micro-wire torsion [4, 6, 7], the foil thickness in micro-foil bending [8] and the plastic deformation zone in nano-indentation experiments [9-11].

**i Micro-wire torsion**

In order to confirm the SGP theory and observe direct experimental results for strain gradient hardening, in 1994, Fleck *et al.* [4] designed both tension and torsion experiments on thin polycrystalline copper wires. The purpose of these two experiments design is to test the effect of the strain gradients on the strength of the samples. In uniaxial tension experiments, the strain gradients are insignificant; the strength is attribute to the accumulation of statistically stored dislocations (SSDs) only. On the other hand, in wire torsion experiments, since the samples are deformed inhomogeneously, strain gradients are involved, hence, the sample is strengthened by both statistically stored and geometrically necessary dislocations (GNDs). For a given surface shear strain, the smaller diameter wire has the greater strain gradients and associated higher GNDs density. As a result, the thinner wire is expected to be much stronger than the thicker wire in the torsion experiment.

Specimens ranging in diameter from 12 to 170μm were used for both tension and torsion tests. Corresponding to their expectation, they observed very strong size effects in the torsion experiments on thin copper wires, however, there is no obvious influence of wire diameter on the tensile behavior. As shown in Fig.1.4 (a), tension data for diameter in the range 12-30μm almost overlap together. The data of 170μm is about 10% below of other plots, maybe the reason is the grain size was larger than other wires. The torsion data is displayed in figure1 (b), with the increase of the wire diameter, it is quite clear that the strength of the specimens decreased.

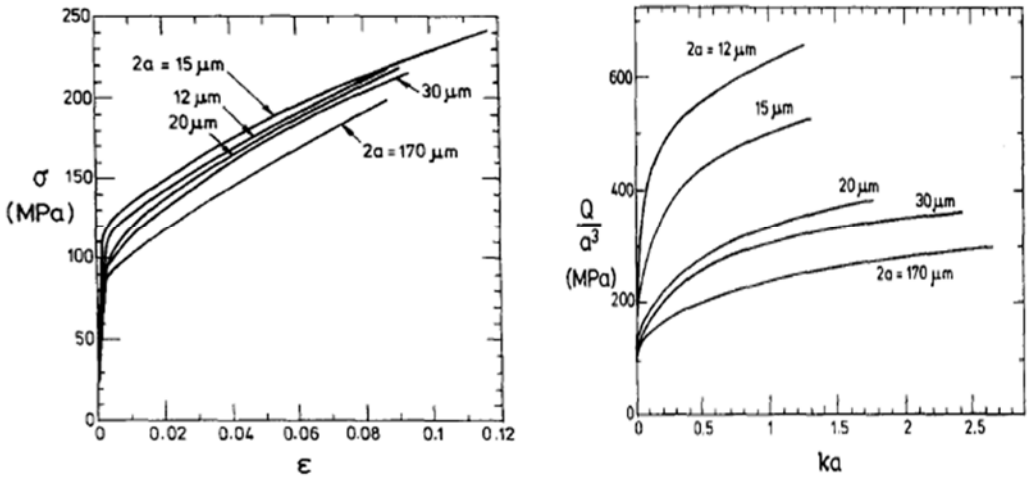


**(a)** **(b)**

**Fig.1.4 (a) Tension data for copper wires of diameter in range 12-170μm. (b) Torsion data for copper wires of diameter in range 12-170μm. (Reproduced from Fleck et al., 1994 [4] )**

### ii Micro-foil bending

Since the micro-foil bending experiment is closely related with my research project, I will give a full literature review in chapter 3. In this section, the classic results of the Stolken and Evans' experiment is described briefly.

In 1998, Stolken and Evans [8] published a micro-foil bending experiment. They were motivated by the significant divergence on the plasticity length scale values obtained by torsion (2.6-5.1μm [4, 12] ) and indentation (~0.5μm [13] ), respectively. Hence, the main purpose of this experimental design is to propose a new brilliant and convenient load-unload method for obtaining the plasticity length scale value. Results for high purity Ni were presented.

The normalized bending moments were plotted against the surface strain in their results, as shown in Fig.1.5. The plot obviously suggested that the strength of the foils increased greatly when the thickness of the foil decrease below 25μm. Their measurements of the plasticity length scale was about 4μm which was quite close to the magnitude obtained for Cu by wire torsion experiments [4].

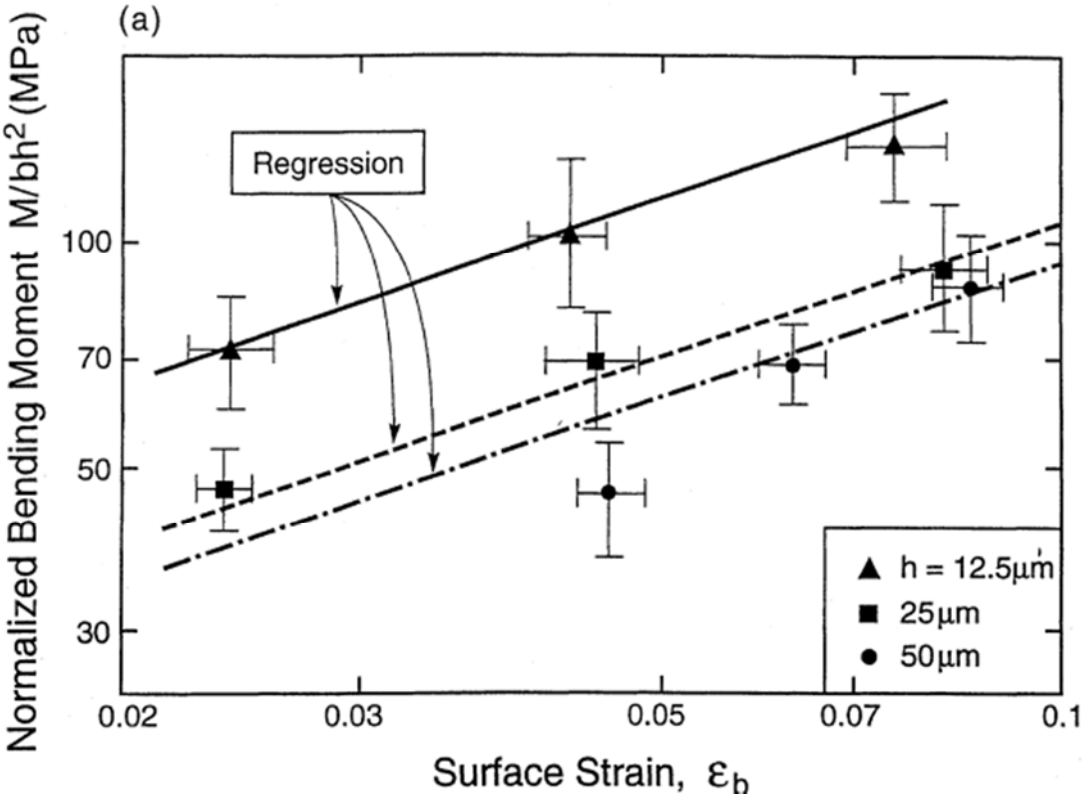


**Fig.1.5 The normalized bending moment were plotted against the surface strain for all three foil thickness ranging from 12.5 to 50μm. (Reproduced from Stolken and Evans, 1998 [8])**

### iii Nano-indentation

The indentation test is a technique to determine the hardness of materials. The indentation size effect (ISE) is one kind of size effect related to the finite volume of material undergoing strain. There are various indenter shape in the different indentation experiments. I will introduce the spherical indentation test, because the spherical indentation tests generate a large contact area but with a small depth. In this case, the small elastic deformation could be fully recovered during the unloading process, hence, the entire stress-strain plot including yield and elastic-plastic transition could be measured. Spary and Bushby [9] published indentation test data on Ni, as shown in Fig.1.6. The stress is expressed by the indentation load divided by contact area, the strain is defined by the ratio of the contact radius ($a$) and the indenter radius ($R$). The four different symbols represented the different radii of the indenter: circle, R=290μm;

triangle, R=20μm; square, R=10μm; diamond, R=5μm. Significantly, with the decrease of the radius of the indenter, the strength increased.

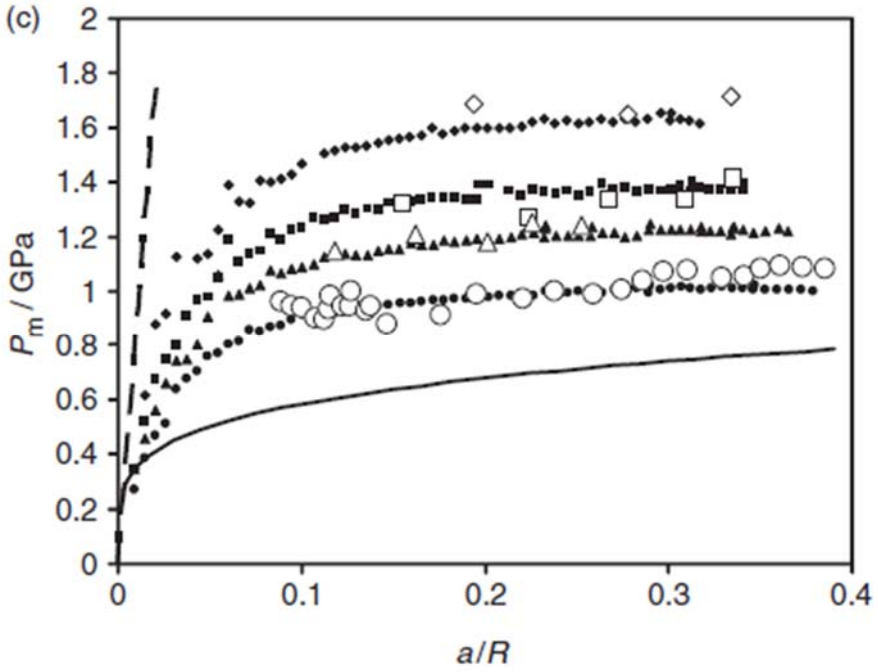


**Fig.1.6 The closed symbols are finite element simulations, the open symbols are experimental indentation data for Nickel: circle, R=290μm; triangle, R=20μm; square, R=10μm; diamond, R=5μm. The strength increased as the radius of indenter decreased. (Reproduced from Spary and Bushby, 2006 [9] )**

## 1.2.2 Homogeneous deformation experiment

The typical homogeneous deformation external size effect experiment is the pillar diameter in uniaxial micro-pillar compressions. Recently, with the application of focused ion beam (FIB) machining technique and high resolution systems for displacement and force measurements, investigations of the uniaxial micro-pillar compressions became popular. There is plenty of literature on micro-pillar compression experiments with various materials (including Ni [14], Cu [15] and Au [16] ). Julia Greer *et al*. [17] published a dataset of gold micro-pillar compressions. They tested the size effect at the micron scale without the obvious strain gradients which were

frequently associated with micron scale deformation.

In order to ensure the experimental results were not related to one particular sample preparation technique, they adopted two different sample fabrication processes (FIB machining & electroplating). In this paragraph, I will introduce their FIB machining process since this method is the most commonly used technique in sample fabrication. Their work is the first to apply the FIB machining technique to gold samples. The (001) oriented single crystal gold disc was used as the raw material of the pillar fabrication. At the beginning, a high current of Ga ions was used to make a cavity with a 4 micron diameter pillar in the center at the surface of the material. This is important to make sure the indenter tip is contact only with the pillar. Secondly, the finer currents and angles were then used to produce the pillar samples with various diameter. Samples of diameter ranging from 0.4 to 7.5 microns were obtained by this method, Fig.1.7 is an example of the FIB image of the samples.

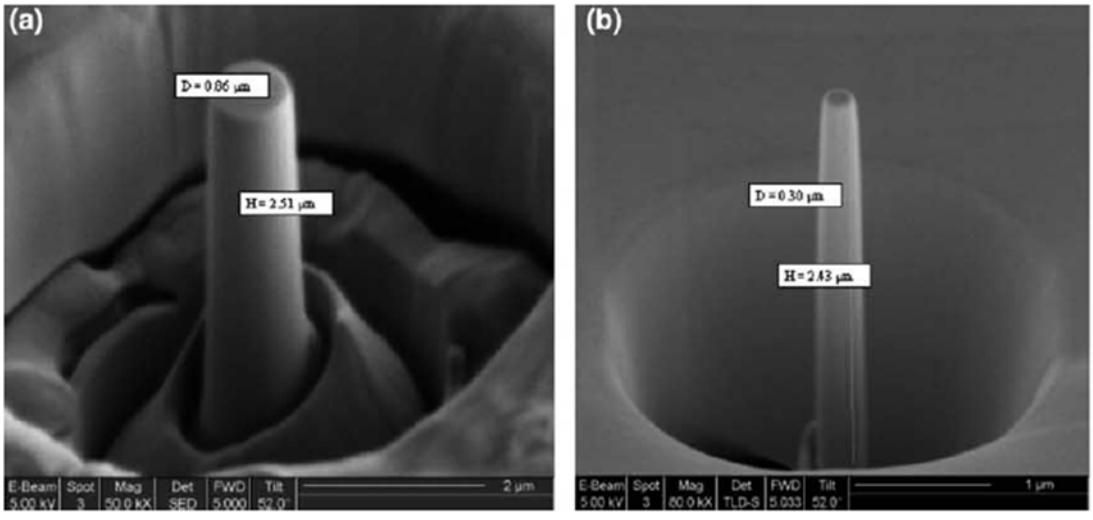


**Fig.1.7 FIB image of the micro pillar samples. (a) 860 nm diameter, 3.2 micron tall; (b) 300 nm diameter, 3.15 micron tall. (Reproduce from Greer et al. 2005 [17])**

Mechanical testing was carried out by using the dynamic contact module of the Nano-indenter XP with a flat indenter tip. To guarantee the unloading data was elastic, the

compressing process used multiple cycles of loading & unloading method before reaching the maximum load.

The results of the uniaxial compression experiments suggested a clear sample size effect. The compressive stress-strain dataset was plotted, as shown in Fig.1.8. Six different samples with diameters ranging from 0.4 to 7.45μm were plotted. When the sample size decrease below 1μm, the yield and flow stress of the samples increase significantly.

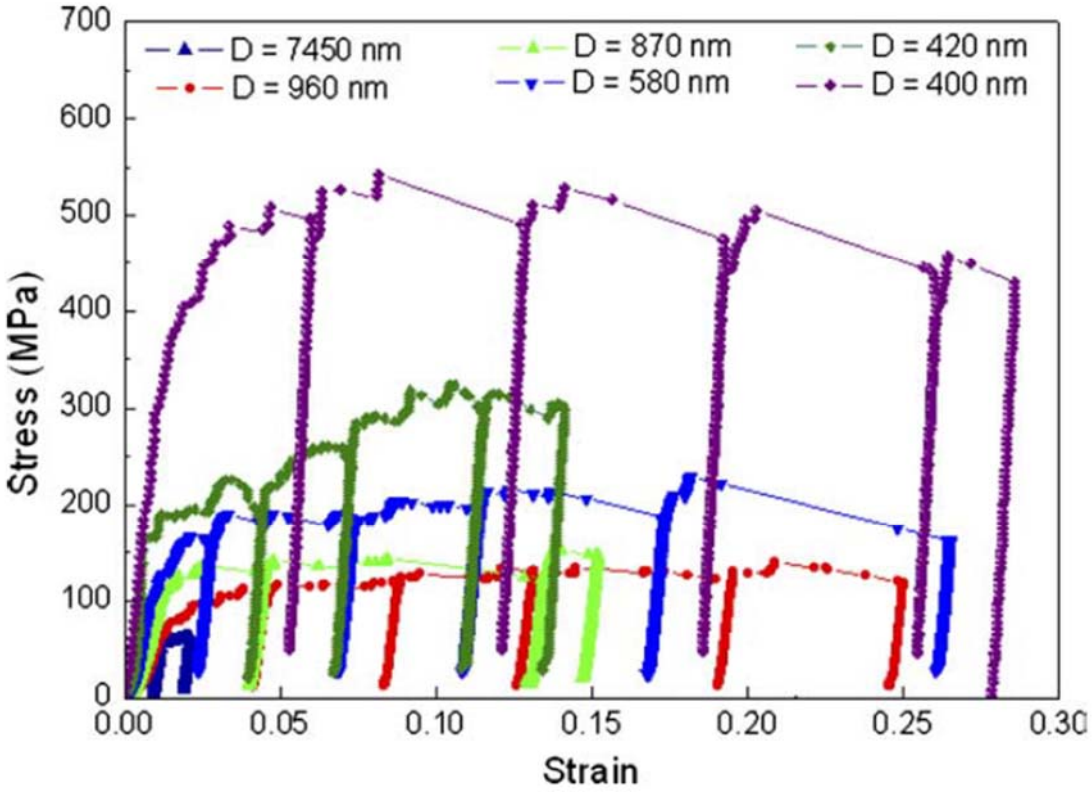


**Fig.1.8 The compressive stress-strain plot of (001) oriented pillars: flow stresses increase radically when pillar diameters decrease below 1μm. (Reproduce from Greer et al. 2005 [17])**

## 1.3 Internal size effect

Internal size effects are due to the size constraints of the microstructure such as impurity particle and grain size. The internal size effects are mainly affected by materials fabrication processes, e.g. metallurgical process of the alloy. The main hardening

mechanisms include precipitation hardening (age hardening) [18, 19], Taylor dislocation hardening (work hardening) [20, 21] and the grain size effect. I will only review the classic references on the grain size effect in this chapter since it is closely related with my research project (investigation on the grain size effect model and theory). The grain size effect is the most common and important subject of investigations on internal size effects.

Grain size has been known to have a significant effect on the mechanical behaviour (yield or flow stress) of the materials [5]. The most famous grain size effect relationship is Hall-Petch effect, which I will described in detail below.

In the 1950s, Hall [22] and Petch [23] presented experimental data showing that the yield stress of iron and steel increases when the grain size is smaller. Based on the dislocation pile-up theory of Eshelby et al. [24], they first established the relationship expressed by the famous Hall-Petch equation:

$$\sigma(d) = \sigma_0 + \frac{k_{HP}}{\sqrt{d}} \tag{1.7}$$

where $\sigma(d)$ is the yield stress or a flow stress at higher plastic strains, $\sigma_0$ is the corresponding bulk yield stress for large single crystals, $k_{HP}$ is considered to be a material constant and $d$ is the grain size. Hall's mild steel wire tension data is shown in Fig.1.9. This data was consisted of three kinds of mild steel, Armco, Siemens-Martin (PXQ quality) and Basic Bessemer (Thomas quality). The samples were annealed in vacuum to obtain the different grain sizes.

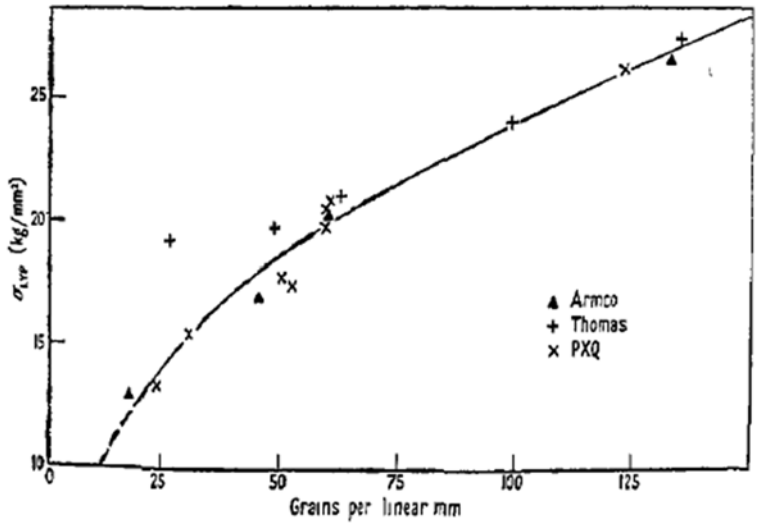


**Fig.1.9 The lower yield point plotted against the inverse grain size. A parabola was plotted by the author indicated an inverse square root relationship. (Reproduced from Hall, 1951 [22])**

A large body of data on other metals was soon reported [25-28] . All of them claimed to fit the inverse square root relationship well. It is worth to present the reference from Aldrich and Armstrong, 1970 [29]. They studied tensile data on silver. The pure silver samples were recrystallized over a wide range of grain size from 1 to 60μm. In their discussions, the yield and tensile fracture stresses were plotted against $d^{-1/2}$, $d^{-1}$ and $d^{-1/3}$, as shown in Fig.1.10. The linear plots were obtained by the least squares fitting method. They concluded that $d^{-1/2}$ relationship fitted best. The $d^{-1}$ fitting were also supported by much of the data but not by all. They ruled out the $d^{-1/3}$ fit because it gives a negative intercept on the y-axis. The negative stress intercept was considered unphysically acceptable.

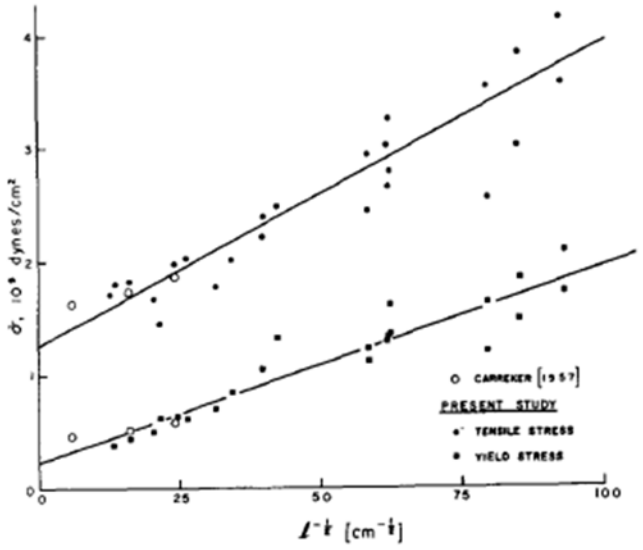


**(a)**

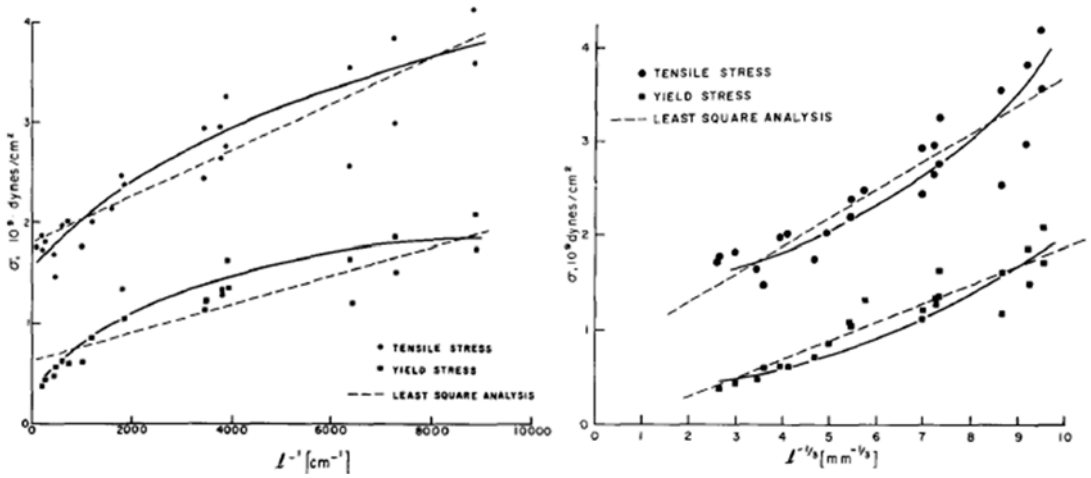


**(b)** **(c)**

**Fig.1.10 The yield and tensile fracture stresses were plotted against with (a) $d^{-1/2}$, (b) $d^{-1}$ and (c) $d^{-1/3}$, respectively. The dashed line in (b) and (c) represented the liner plots by the least square fitting analysis. The $d^{-1/3}$ fit was excluded because of a negative intercept on the y-axis. (Reproduced from Aldrich, 1970 [29] )**

Another interesting Hall-Petch data is from Narutani and Takamura [30]. They reported wire tension data on nickel. They obtained the Hall-Petch plot data from the tensile tests at a strain rate of $3.0\times10^{-4}$ $s^{-1}$ at 77K. They concluded that the data follow the Hall-Petch relationship for small strains (less than 5%). However, for larger strains, the plot clearly deviating from the inverse square root relationship. The data are reproduced in Fig.1.11.

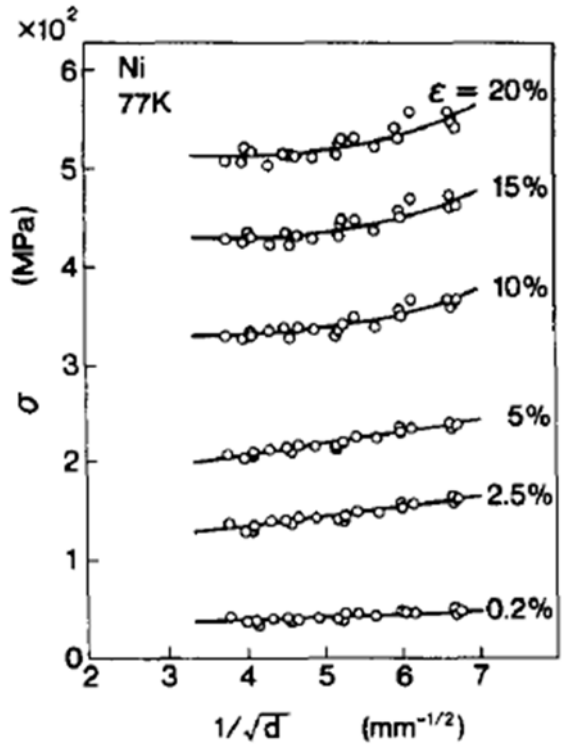


**Fig.1.11 The Hall-Petch plot of wire tension data on nickel. The stress was plotted against inverse square root grain size. For small strains (less than 5%), the linear relationship were plotted, but, for larger strains, the fitting is a curve which clearly deviating from the Hall-Petch equation. (Reproduced from Narutani and Takamura 1991 [30])**

## 1.4 General size effect theories

The most popular theory for the explanation of inhomogeneous deformation size effects is strain gradient plasticity (SGP) theory [4]. When the SGP theory is related to a high density of GNDs at large plastic strain, however, Evans and Hutchinson (2009) [31] indicated that SGP theory can predict a size effect on enhancing yield stress. For a perfect plastic solid, they showed that the Fleck & Hutchinson (FH) model can predict an increase in the yield strength but no size effect in strain hardening, while the Nix & Gao (NG) model predicts an elevation of the strain hardening rate but not the yield strength. Evans and Hutchinson cannot explain this behaviour in physical terms. The FH model considers an increase of the energy required for generating a strain gradient,

by considering no effect of any dislocation density. At the initial yield point, there is no plastic strain, the density of GNDs is zero. Producing a plastic strain gradient requires the creation of GNDs. Actually, this is exactly the same physical mechanism when the critical thickness theory (CTT) [32] explains the initial yield size effects. Hence, in this section, both the SGP and CTT theories are reviewed.

### 1.4.1 Strain gradient plasticity theory

As introduced in the description of GNDs (Section 1.1.1), when the materials deform with inhomogeneous strain, the GNDs will be introduced to accommodate the plastic strain gradient. When the sample size decreases, a larger plastic strain gradients are introduced, then the related higher density of GNDs (Eq.1.4) makes the total density of dislocation $\rho_t$ (assumption of the sum of GNDs and SSDs) greater. Based on Taylor work hardening model, the materials will get stronger. This is the SGP theory [2, 33].
There are various reasons for the production of the plastic strain gradient [4]: (1) the external geometry of samples; (2) some mechanical test methods e.g. nano or micro-indentation; (3) the micro-structure is plastically inhomogeneous e.g. containing non-deforming particles. Schematics are shown in Fig.1.12. In the micro-wire torsion experiment, the strain is zero along the axis of twist but it is greater than zero at the surface. In the micro-foil bending experiment, the plastic strain is zero at neutral plane but it is greater than zero at the both surfaces, as shown in Fig.1.12 (a), (b). In the nano or micro indentation test, the plastic strain under the indenter is greater than zero but it is zero far from plastic zone, as shown in Fig.1.12 (c), (d). In the micro-structure containing non-deforming particles, the strain gradients are produced in the space between the non-deforming particles, but the plastic strain in the non-deforming particle itself is zero; the different slip orientation at the grain boundaries will also produce the plastic strain gradient, as shown in Fig.1.12 (e), (f).

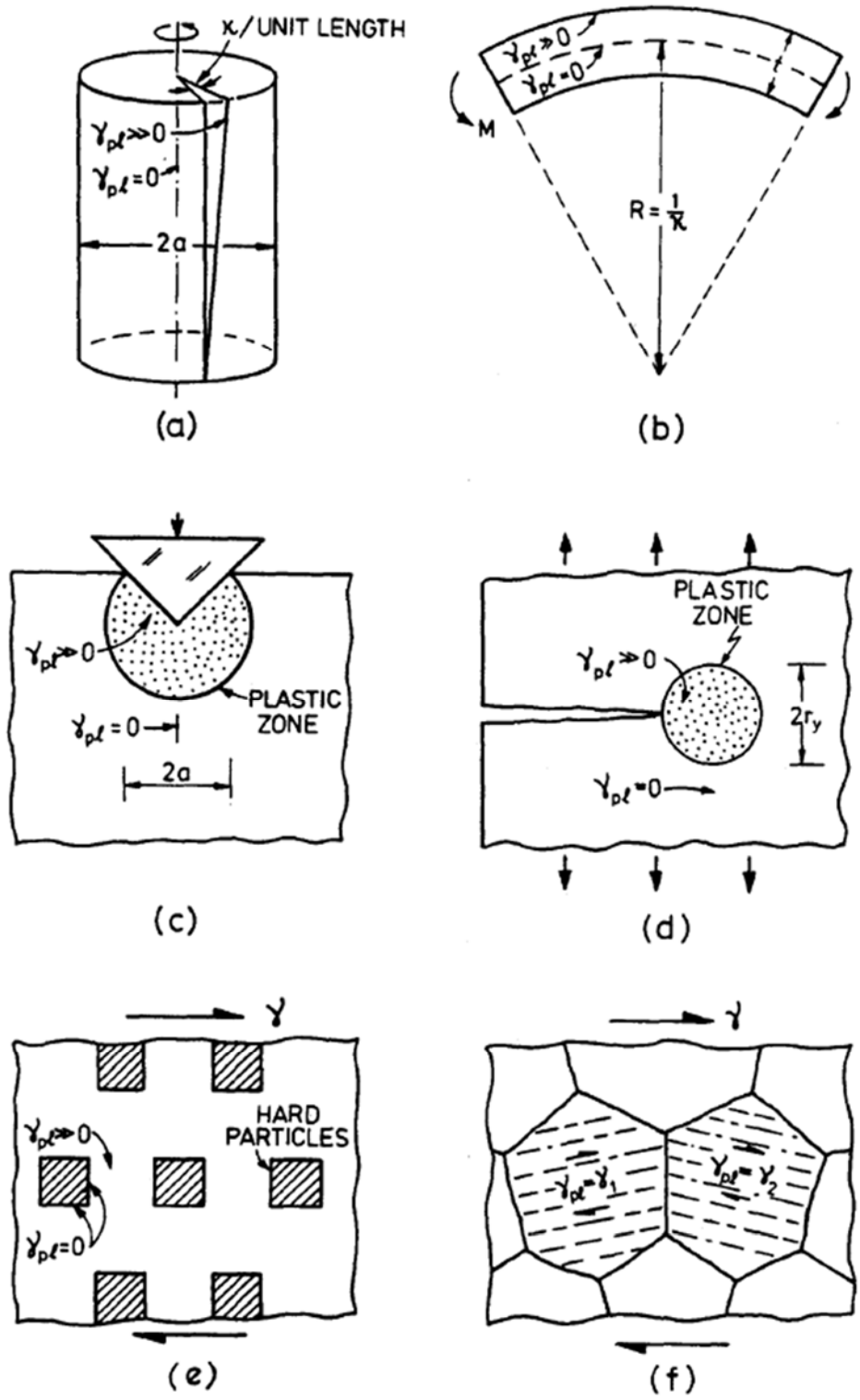


**Fig.1.12 Schematic diagrams of the various ways to produce the plastic strain gradients. (Reproduced from Fleck 1994 [4])**

The Nix-Gao model is a typical model to describe the SGP theory. This model is based on the Taylor hardening relation, in which the flow stress $\sigma_e$ is expressed as

$$\sigma_e = m\alpha Gb\sqrt{\rho_T} \tag{1.8}$$

where $m$ is a Taylor constant acting as an isotropic interpretation of the crystalline anisotropy, and $m=\sqrt{3}$ for an isotropic solid, $m=3.06$ for FCC polycrystalline metals, $\alpha$ is an empirical constant, $G$ is the shear modulus, $b$ is the average magnitude of the Burgers vector for the polycrystalline structure, the magnitude of the $b$ in a single crystal depends on the angle between the crystal orientation and slip plane, and $\rho_T$ is the total dislocation density. According to Ashby's theory [2], the total dislocation density can be assumed as the sum of the density of statistically stored dislocations (SSDs), $\rho_S$ and that of geometrically necessary dislocations (GNDs), $\rho_G$. Then the Eq.1.8 can be written as

$$\sigma_e = m\alpha Gb\sqrt{\rho_S + \rho_G} \tag{1.9}$$

In the absence of strain gradients, i.e. only $\rho_S$ is considered in Eq.1.9

$$\sigma_e = \alpha mGb\sqrt{\rho_S} = \sigma_Y f\left(\varepsilon_{\mathrm{P}}\right) \Rightarrow \rho_S = \left[\frac{\sigma_Y f\left(\varepsilon_{\mathrm{P}}\right)}{\alpha mGb}\right]^2 \tag{1.10}$$

$\sigma_Y f\left(\varepsilon_{\mathrm{P}}\right)$ represents the stress-plastic strain relation in the absence of the gradient effect. And $\sigma_Y$ is the initial yield stress, $f\left(\varepsilon_{\mathrm{P}}\right)$ is a function of plastic strain. The density of GNDs can be calculated as

$$\rho_G = \bar{r}\eta_{\mathrm{P}}/b \tag{1.11}$$

where $\eta_{\mathrm{P}}$ is the effective plastic strain gradient, $\bar{r}$ is the Nye factor reflecting the scalar measure of the density of GNDs due to plastic strain gradients [34]. For FCC polycrystalline metals, Arsenlis and Parks [34] indicated that the Nye factor $\bar{r} \approx 1.85$ in bending and $\bar{r} \approx 1.93$ in torsion.

If $\sigma_e$ is a function of $\varepsilon_P$ and $\eta_{\mathrm{P}}$, then on dimensional consideration, $\eta_{\mathrm{P}}$ must be

multiplied by a length. Substituting Eq.1.10 and Eq.1.11 into Eq.1.9, Nix and Gao [35] obtain a law for strain gradient plasticity

$$\sigma_e = \sigma_Y \sqrt{f^2(\varepsilon_{\mathrm{P}}) + l_{\mathrm{NG}}\eta_{\mathrm{P}}} \tag{1.12}$$

where $\varepsilon_{\mathrm{P}} = \sqrt{\frac{2}{3}\varepsilon_{ij}^{\mathrm{P}}\varepsilon_{ij}^{\mathrm{P}}}$ is the effective plastic strain, and $l_{\mathrm{NG}}$ is the material length scale in the NG theory which is expressed as

$$l_{\mathrm{NG}} = \alpha^2 m^2 \bar{r} \left(\frac{G}{\sigma_Y}\right)^2 b. \tag{1.13}$$

For an isotropy material, the yield stress can be calculated as

$$\sigma_Y = 2G(1+\nu)\varepsilon_Y \tag{1.14}$$

where $\nu$ is the poisson's ratio. Substituting Eq.1.14 into Eq.1.13, we then have

$$l_{\mathrm{NG}} = \frac{\beta b}{\varepsilon_Y^2} \tag{1.15}$$

Here, $\beta = \frac{m^2\bar{r}\alpha^2}{4(1+\nu)^2}$ is on the order of unit. For FCC metals, $m = 3.06$, $\bar{r} \approx 1.85$, $\alpha$=0.4 , $\nu = 0.33$, so we have $\beta \approx 0.22$.

## 1.4.2 Critical thickness theory

The theory of the critical thickness of strained layers was first introduced by Frank and van der Merwe [36] in 1949. They proposed a one-dimensional theory to explain monolayer growth on a crystalline substrate. They found that the critical misfit between the monolayer and substrate is 9%. Up to the critical misfit 9%, the epitaxial layer is deformed to fit the substrate. Above 9% misfit, dislocations formed in the lattice. In the 1970s, Matthews [37, 38] considered the energy thermodynamic stability of film growth. The strain energy is linearly proportional to the film thickness from zero, while the energy of the misfit dislocation which is responsible for relaxation has a weaker (logarithmic) dependence on thickness (shown in Fig.1.13). It is clear that thin films should be thermodynamically stable. Hence, critical thickness is defined as the thickness at which the fully strained layer becomes unstable or metastable. It means

that up to critical thickness, the layer grows with an elastic strain determined by the misfit, above the critical thickness, thermodynamic stability is lost and misfit dislocations are introduced to relax the coherency strain, i.e. once the strain energy is sufficient enough to create a misfit dislocation, thermodynamics permits misfit dislocations to reduce the total energy of the system by the nucleation and propagation.

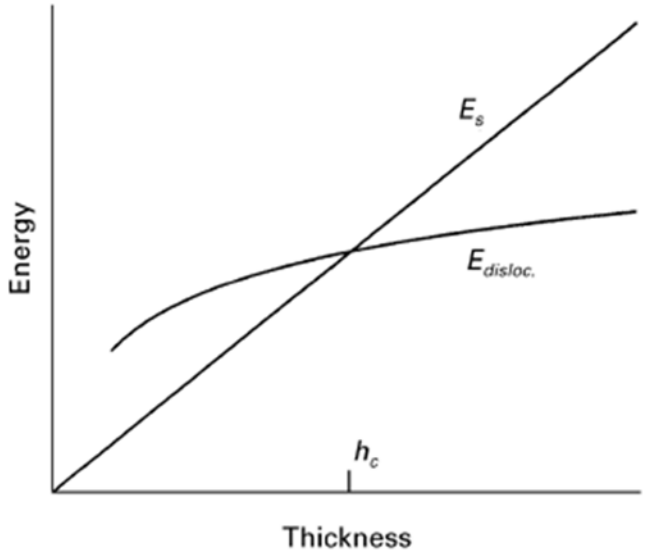


**Fig.1.13 Schematic diagram showing that the elastic strain energy $E_S$ increases in proportion to the strained layer thickness $h$, the energy of the misfit dislocation has a logarithmic dependence on thickness. Critical thickness $h_c$ is the crossing of the two lines (Reproduced from Dunstan, 1997 [39])**

Matthews derived the critical thickness theory by considering the force balance on threading dislocations and the equilibrium of total energy of system which include the energy of an elastically strained overlayer and energy of misfit dislocation per unit area. For a 001-oriented layer, this is given as

$$h_c = \frac{b(1 - \nu \cos^2 \theta)}{8\pi\varepsilon (1 + \nu) \cos \lambda} \ln \frac{h_c}{b} \tag{1.16}$$

Where $b$ is the magnitude of the Burgers vector, $\nu$ is the Poisson ratio, $\lambda$ is the angle between the slip plane direction and a line in the film plane which is perpendicular to

the intersection of the glide plane with the interface, $\theta$ is the angle between the dislocation line and the Burgers vector. $\varepsilon_0$ is a given misfit.

We consider that

$$k = \frac{1 - \nu \cos^2 \theta}{8\pi(1 + \nu) \cos \lambda} \tag{1.17}$$

is a factor of the order of unity determined by crystallographic parameters, the relative orientation of the slip planes, the growth plane and the direction of the Burgers vector. Critical thickness Eq.1.16 is expressed by

$$h_c = \frac{kb}{\varepsilon} \ln \frac{h_c}{b} \tag{1.18}$$

Fitzgerald [40] reviewed carefully the Matthews analysis and gave the correct derivation of Matthews equation to account for the $l^{-1}$ and ln$l$ terms from the mechanical and dislocation energy aspect, respectively. Balancing the total lateral force which acts on the point of intersection between the threading dislocation and the interface plane is the line-tension force of the dislocation section residing in the interface, the displacement of material due to the introduction of a dislocation is the constant $b$. This explains that the stress required scales inversely with the dimension $l$ of the material displaced through $b$. The dislocation energy can be mainly attributed to the elastic energy of the strain field of the dislocation. This elastic energy is determined by the integration of the strain energy $\propto r^{-1}$ from the dislocation. To avoid divergence the integral has to be cut off at an inner core radius $r_0 \sim b$ and an outer radius $R_0$ which is given by a free surface, the outcome of $ln\ (R_0/b)$ is the physical origin of the logarithmic term in Eq.1.18.

Matthew's critical thickness theory has been applied powerfully in the semiconductor [41, 42] and the epitaxial layers of the ductile metals. This robustness led Dunstan and Bushby to propose [32] a general explanation underlying any microscopic mechanism. Based on the critical thickness theory, strain relaxation requires a displacement of materials over a finite distance (the magnitude of the burgers vector). They proposed that the misfit dislocation will formed only if the change of the strain $b/h$ is less than

the order of the strain to be relaxed. They gave the relationship between the critical thickness and critical strain:

$$\varepsilon_c \approx \frac{b}{h_c} \tag{1.19}$$

By considering dislocation multiplication, source operation and significant relaxation happen at five times critical thickness, we can write Eq.1.19 as:

$$\varepsilon_c \approx \frac{5b}{h_c} \tag{1.20}$$

Eq.1.19 (Eq.1.20) is called the geometrical strength or the geometrical contribution to the yield strain. In micro-mechanical tests on metals, the elastic strains are much smaller than that in epitaxial strained layers. Hence, the bulk yield strain also needs to be considered. The Eq.1.19 (Eq.1.20) then could be changed to:

$$\varepsilon_c \approx \frac{b}{h_c} + \varepsilon_Y \tag{1.21}$$

$$\varepsilon_c \approx \frac{5b}{h_c} + \varepsilon_Y \tag{1.22}$$

The Eq.1.21 could be transformed into a general size effect equation which was named as dislocation curvature equation:

$$\varepsilon = \varepsilon_0 + kd^{-1} \tag{1.23}$$

And also the very similar form,

$$\varepsilon = \varepsilon_0 + k\frac{\ln d}{d} \tag{1.24}$$

where $\varepsilon$ is the elastic strain obtained by stress normalized by the relevant elastic modulus, dimensionless constant $k$ is the factor of the order of unity, $\varepsilon_0$ is the strain $\sigma_0/Y$ describing the bulk strength, it may be the strength due to other material processing methods e.g. work-hardening, $d$ is the dimensionless parameter $\frac{h_c}{b}$, e.g. grain size normalized by the magnitude of Burgers' vector. The physical meaning of $d$ is the number of the crystal unit cell. Eq.1.23 (Eq.1.24) is theoretically applicable to any

situation where a dimension constrains the size of the dislocation sources that have to operate if plasticity is to occur, so $d$ may be normalized non-dimension structure size, or some suitable combination of these factors.

## 1.5 The Hall-Petch effect models

The famous Hall-Petch equation has been proposed more than 60 years. However, the real physical mechanism underlying this relationship remains unclear. In the past a few decades, many different models were developed to explain the Hall-Petch equation. Schuh published a review to present the models comprehensively [43]. Generally, there are four distinct models proposed by the classic literature:

(a) Dislocation pile-up model;

(b) Grain boundary source model;

(c) The slip distance model;

(d) The elastic anisotropy model.

Most of these models explain the two parameters of Eq.1.7 ($k_{HP}$ & $\sigma_0$) separately. The $\sigma_0$ is considered to bulk yield stress which unrelated to the grain size, while the $k_{HP}$ is key term to account for the grain size dependent. Different models predict the different values of $k_{HP}$.

### 1.5.1 Dislocation pile-up model

The dislocation pile-up model is the most commonly cited explanation of the Hall-Petch effects. In 1951, Hall [22] published a series of papers to show yield behaviour of mild steels. In the third paper, he used the dislocation pile-up model to explain the inverse square root relationship [44].

In this model, for an applied stress, the dislocation sources become activated. A dislocation source in a grain can produce a number of dislocations. The grain boundaries in poly-crystals are obstacles for the generated dislocations. Hence, the

dislocations plie up against grain boundary. They are distributed in the slip plane non-uniformly as shown in Fig.1.14.

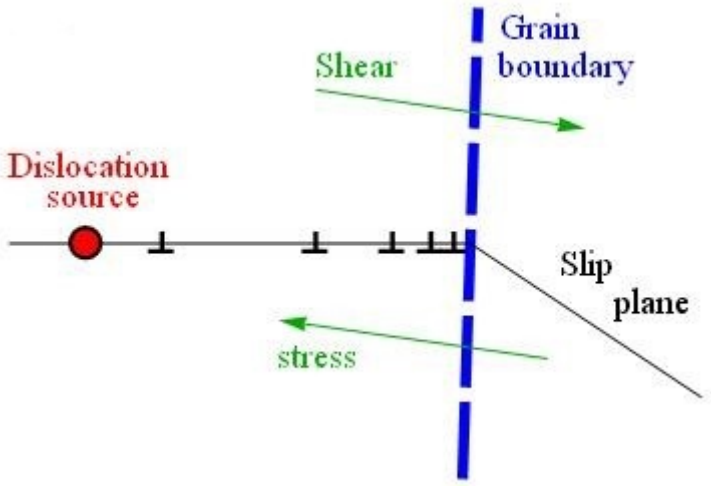


**Fig.1.14 Schematic representation of dislocation pile-up. (Reproduced from Y. Li & Dunstan 2016 [45])**

The first dislocation next to the grain boundary supports the forces from the following dislocations behind it. A cumulative stress is built up at the tip of the pile-up [46, 47]. We assume there are *n* dislocations in this pile-up, the cumulative stress is

$$\tau = n\tau_e \tag{1.25}$$

$\tau_e$ *i*s the effective shear stress.

When the stress concentration at the first dislocation reaches a critical value $\tau_c$, slip will cross the grain boundary. Dislocations will propagate to the next grain. In this situation,

$$\tau_c = n\tau_e \tag{1.26}$$

If the pile-up is of length *L*, Eshelby [24] calculated $\tau_e$ as

$$\tau_e = \frac{Gnb}{\pi L} \tag{1.27}$$

where *G* is shear modulus, *b* is magnitude of the burger's vector and pile-up length *L* here is grain size *d*. Combining the Eq.1.26 and Eq.1.27, the expression of $\tau_e$ can be obtained as

$$\tau_e = \sqrt{\frac{Gb\tau_c}{\pi d}} \tag{1.28}$$

If we considered $\tau_o$ is the corresponding stress for large single crystals material, then Eq.1.28 becomes

$$\tau = \tau_0 + \sqrt{\frac{Gb\tau_c}{\pi d}} \tag{1.29}$$

## 1.5.2 Grain boundary source model

The dislocation pile-up model explains well for a number of steel data. However, direct experimental observations (i.e. SEM images of dislocation pile-up at boundaries) are not always found [48]. As a result of this weakness, other explanations for grain size strengthening were proposed by researchers.

Li [49] first proposed that grain boundaries are sources of dislocation. In this model, dislocation pile-up is unnecessary. The example of grain boundary ledge generated dislocation is shown in Fig.1.15. The grain boundary ledge just donates a single dislocation. At the beginning of the yield, the initial dislocation density is provided by the grain boundary ledges. The forest formed by all the dislocations produced by the grain boundary ledge. If the ledge density in the grain boundary is $m$ (number per unit length), the dislocation density in the forest is about $8m/\pi l$. Hence, according to Taylor's law for forest dislocation hardening, the flow stress is:

$$\tau = \tau_0 + \alpha Gb\sqrt{\frac{8m}{\pi d}} \tag{1.30}$$

where $\alpha$ is a constant depends on dislocation arrangement, generally, the value of $\alpha$ is 0.4. $G$ is shear modulus.

+

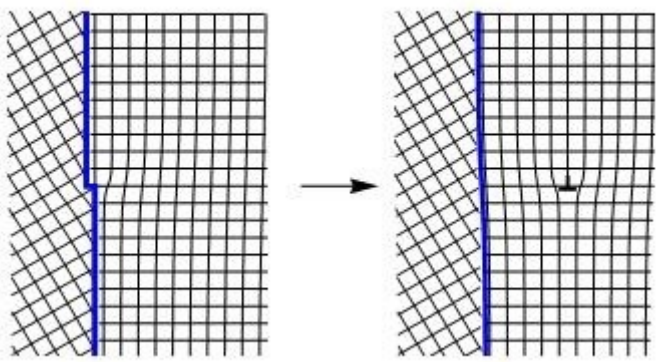

**Fig.1.15 The example of grain boundary ledge acting as donor of dislocations. (Reproduced from Y. Li & Dunstan [45] )**

In 1975, Murr [50] reported the direct experimental observation of the grain boundary ledge model. A transmission electron microscope (TEM) was used to study the grain boundary structure of annealed Ni, Al, Cu, stainless steel and other metals. The results shown the occurrence of grain boundary ledges in many of the metals and alloys. Grain boundary ledges have been observed to be sources of dislocations during plastic deformation.

## 1.5.3 The slip distance model

In 1953, Cottrell [51] reported that the dislocation density is related to the tensile strain. It is expressed by:

$$\varepsilon = \alpha_1 \rho b s \tag{1.31}$$

where $\alpha_1$ is a constant of the value of 1.4, $b$ is the burgers' vector and $s$ is the average distance each dislocation has moved. Based on Taylor's law, the slope of Hall-Petch equation depends on the plastic strain.

In 1967, Conrad and co-workers [52-54] developed the slip distance model based on

Eq.7. In this model, they proposed that, for a given strain, the higher dislocation density in small grain sample is attribute to the smaller slip distance, as shown in Fig.1.16.

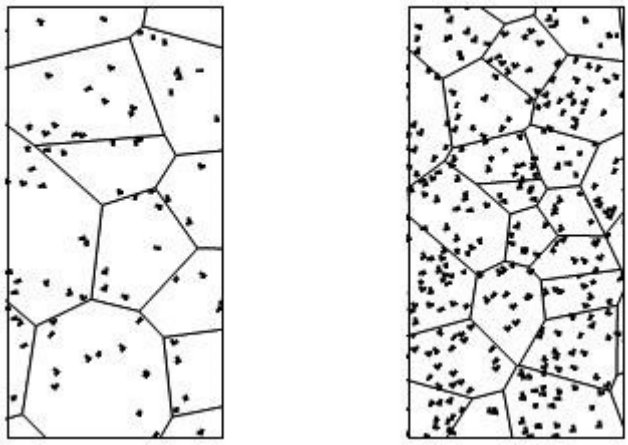

**Fig.1.16 Schematic illustration of slip distance model: dislocation slip length is less in a smaller grain, the dislocation density is higher. (Reproduced from Y. Li & Dunstan [45] )**

To obtain a $d^{-1/2}$ relationship, they proposed the dislocation density $\rho$ varies as $d^{-1}$. They indicated that for a constant strain, the dislocation density is proportional to $d^{-1}$. In Eq.1.31, they assumed that the average free path $s$ is proportional to the grain size $d$, i.e. $s=\lambda d$. Then Eq.1.31 can be rearranged to

$$\rho = \frac{\varepsilon_{pl}}{\alpha_1 b \lambda d} \tag{1.32}$$

using the work hardening equation, substituting Eq.1.32 and rearranging, we can get

$$\tau = \tau_0 + \alpha G b\sqrt{\rho} = \tau_0 + \alpha G\sqrt{\frac{b\varepsilon_{pl}}{\alpha_1 \lambda d}} \tag{1.33}$$

where $\alpha$ is a Taylor constant depends on dislocation arrangement, $G$ is the shear modulus. $\alpha_1$ and $\lambda$ are both constant but less the order of unity.

## 1.5.4 The elastic anisotropy model

Hirth [55] and Meyers [56] proposed the elastic anisotropy model. In this model, anisotropic grains are distributed in a homogenous stress field, the same GNDs mechanism is used, as shown in the Fig.1.17.

Fig.1.14 present a two-dimensional cubic material with anisotropy factor $C = |c_{11} - c_{12} - 2c_{44}|$ elastically deformed under a uniform shear stress field. In this model, as introduced in Section 1.4.1, when the grain sizes decrease, the strain gradients and the density of GNDs will be proportionately larger. Hence, if the total density of dislocation $\rho$ is the simply sum of SSDs and GNDs, $\rho$ will increase accordingly. This model predicts that after suitable normalization, $k_{HP}$ will be proportional to the elastic anisotropy. The factor of proportionality is not explained by the model. The only experimental evidence of this factor is that it depends on the characteristic length in the strain-gradient theory.

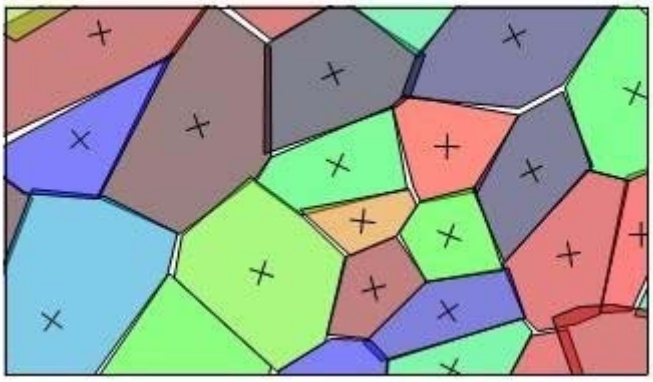

**Fig.1.17 The effects of crystalline elastic or plastic anisotropy in forcing stress and strain gradients, in which anisotropic grains are subject to a homogenous stress field. (Reproduced from Y. Li & Dunstan [45] )**

## 1.6 Summary

Research on the size effect is essential in materials science. In this chapter, both the experimental observations in different geometries and various theories related to experimental results are reviewed.

Grain size effect is one of the most important issue of size effect. In the six decades since Hall-Petch equation was proposed in 1953, a large body of researches on this empirical equation have been published. However, there are various models. On the

other hand, based on the critical thickness theory, Dunstan and Bushby proposed the curvature dislocation equation theoretically applicable to any situation, i.e. it is a general size effect theory. Thus, one aim of my thesis is to review plenty of classic Hall-Petch data and theories and to discuss the physical mechanism underlying the Hall-Petch relationship.

Investigations on SGP theory were very popular since Fleck *et al.* published wire torsion and tension results in 1994. The micro-foil bending test is a good candidate for the testing of SGP theory. The traditional experimental design had weaknesses for obtaining high quality data. Hence, another aim of my thesis is to design of a new equipment to overcome the difficulties. Then high quality data could be used to test the relative theories.

# 2. The Hall-Petch effect as a manifestation of the general size effect

## 2.1 Introduction

Grain size has been known to have a significant effect on the mechanical behaviour (yield or flow stress) of the materials [5]. As described in the literature review, the most famous equation to explain the grain size effect is Hall-Petch equation:

$$\sigma(d) = \sigma_0 + \frac{k_{HP}}{\sqrt{d}} \tag{2.1}$$

where $\sigma(d)$ is the yield or a tensile flow stress at higher plastic strains, $\sigma_0$ is the corresponding bulk yield stress or large single crystals, $k_{HP}$ is a constant that considered to be a material constant and $d$ is the grain diameter.

As described in Section 1.4.2, based on the critical thickness theory, Dunstan and Bushby presented a general size effect expression underlying any microscopic mechanism:

$$\varepsilon_{e1}(d) = \varepsilon_0 + k\frac{\ln d}{d} \tag{2.2}$$

where the fixed constant $k$ is expected to be the order of unity, $\varepsilon_0$ is the strain $\sigma_0/Y$ describe the bulk strength or it may be the strength due to other material processing methods, e.g. the work-hardening, the dimensionless parameter $d$ is theoretically applicable to any situation where a dimension constrains the size of the dislocation sources. In this chapter, $d$ will be the grain size which normalized by lattice constant $a_0$. It is found that the complete lack of any data falling under the line of Eq.2.2 with $k$~1 and $\varepsilon_0$=0, implying that Eq.2.2 describes the minimum strength, due to the size effect [57]. Then a collection of 17 datasets from the classic literature of the Hall-Petch effect are also above this line [58]. They recognized that this can be taken as experimental support for the applicability of Eq.2.2 to the Hall-Petch effect.

Returning to the Hall-Petch effect, as described in the literature review, many authors have considered the exponent of inverse square root is not suitable for their datasets. Hence, different exponent values like *2/3* [59], *1/3* and *1* [29] were also proposed. In order to test the power law relationship and confirm the value of the exponent *x*, the free exponent of Hall-Petch equation is used to the fitting as well, expressed as

$$\sigma(\mathrm{a}) = \sigma_0 + ka^{-x} \tag{2.3}$$

where *a* is some suitable characteristic dimension such as micro-pillar diameter or indentation contact radius. Much effort has been invested in finding appropriate values of the scaling exponent *x* for particular materials, or for particular types of materials such as FCC or BCC metals.

In Section 2.2 in total 61 the classic Hall-Petch datasets which include quite general metals e.g. Fe, Brass, Cu, W, Cr, Ti, Ag, Au, Ni and Al were reviewed. All of the dataset resources came from citations, references and search engines. From the early data which contribute to the establishment of Hall-Petch equation to the recent data, I collected all the data I searched with no selection. The analyses shown that the there is no evidence that the data support for Eq.2.1, meanwhile, when we fitted the datasets with Eq.2.3 and the value of scaling exponent *x* is scatted from 0 to 1. In Section 2.3 we use a Bayesian theorem to compare Eq.2.2 and modified Ashby theory. In Section 2.4 we compare the predictions of the different models of the Hall-Petch effect with the data fitting. In Section 2.5, we propose a method to test the Eq.2.2, from the view of the data point distribution in one dataset. Finally, we conclude that Eq.2.2 fits the data as well as with Eq.2.1, but compared with two free fitting parameters in Eq.2.1, one fixed parameter fitting (the factor of the order of unity $k \sim 1$) of Eq.2.2 and modified Ashby equation applied more reasonable, the small grain size data are more close to Eq.2.2.

## 2.2 Review and analysis of the data

We collected 61 datasets in total from the classic references which were claimed strongly corresponding well with Hall-Petch relationship in the past a few decades. All of the general metal datasets like Fe, Brass, Cu, W, Cr, Ti, Ag, Au, Ni and Al were digitized and fitted by using the *Mathematica*© software.

### 2.2.1 Data presentation & Metallurgy review

For each metal, in Fig. (a), we present the datasets as the reported original reference (i.e. Yield or flow stress plots against the inverse square root of grain size with a straight-line). We only change the authors' original units to SI units (MPa), this is convenient to show the different datasets in the same framework. For each dataset, the best fit to the Eq.2.1 is shown, calculated using the Mathematica© function *NonlinearModelFit* with both $\sigma_0$ and $k_{HP}$ treated as free fitting parameters. Then in Fig. (b), we show the data plotted simply against the inverse of grain size. Finally in Fig. (c), the stress and grain size are normalized by the relevant material Young's modulus $Y$ and lattice constant $a_0$, respectively. The purpose of the normalized process here is to eliminate the known differences between the different kinds of metals, i.e. the pure comparisons of constrain size on the different metals. we show the normalized data on log-log plots because of the very wide range of data, on which we show the plot of Eq.2.2 with a fixed appropriate parameter value of $k = 0.72$ and $\varepsilon_0$ treated as free fitting parameter which interpreted the expected minimum strength.

For each dataset, we give what relevant information is available in the original papers about the metallurgical processing, especially grain-size modification and determination, and the yield or flow stress determination, or we mention the absence of this information. It should be noted that Rhines [60] listed about ten ways of determining the grain size. For grains that are not equi-axed or which have a distribution of sizes, these methods can give diverse values for the average grain diameter. Since few authors give their method of grain size determination, much of the variation in

fitted values of $\varepsilon_0$ in Eq.2.2 or $k_{HP}$ in Eq.2.1 may arise from this.

**i Iron and steel**

We should begin with Hall (1951) and Petch (1953) data in which the famous Hall-Petch equation was firstly proposed. For iron and steel, the normalization constants are $Y$=211GPa, $a_0$=0.287nm. Hall [22] measured wires tension data, made from three kinds of mild steel, Armco, Siemens-Martin (PXQ quality) and Basic Bessemer (Thomas quality). The samples were annealed in vacuum to obtain the different grain sizes. The method of measuring the grain sizes is not given. The lower yield points, measured at a strain rate of $10^{-4}$ $min^{-1}$, were plotted by Hall and fitted by an inverse square-root dependence on grain size. We do not distinguish between the three kinds of mild steel in copying this data to Fig.2.1 (Fe (7) black crosses).

Petch [23] reported tensile experiment data on mild steel, ingot iron and spectrographic iron, indicated by Fe (1) black filled circles in Fig.2.1. The specimens ranged from single crystals to 8000 grains/sq.mm. They were prepared by annealing in vacuo at temperatures up to 1050ºC for times up to 24h, followed by cooling at various rates. The single crystals and a few coarse-grained specimens were obtained by straining and annealing the decarburized mild steel. The method of measuring the grain sizes is described as "6–12 counts" on the surface, and to give not the true diameter but to be proportional to the true diameter. Petch was primarily concerned with the cleavage strength, which he showed obeyed Eq.2.1 and explained by identifying glide planes on which the dislocation motion is blocked by grain boundaries with Griffith cracks [61] (1920) and again invoking the theory of Eshelby [24] et al. (1951). However, he also plotted the lower yield point against $d^{-1/2}$ and fitted a single straight line to the data for all three metals, which we do not distinguish in Fig.2.1.

Armstrong et al. [62] (1962) give data for the yield and flow stress of a 0.1%C semi-killed mild steel. The mild steel elemental composition is given. Grain sizes were obtained by 900–1200ºC anneals, followed by machining and polishing and then a final anneal at 650ºC. For the largest grains, annealing at 1200ºC was followed by 8% strain

and a long 650ºC anneal. The method of measuring the grain sizes is not given. They find excellent agreement with linear dependences on $d^{-1/2}$, explained by invoking the Eshelby et al. [24] theory, within the context of the Taylor [63] theory of polycrystalline aggregates. In Fig.2.1 we reproduce their data (Fe (6) brown crosses) for the lower yield point, for 2.5% strain and 20% strain (intermediate strain values of 5%, 7.5%, 10% and 15% gave data evenly spaced between and parallel to the 2.5% and 20% data).

Douthwaite [64] was interested in the relationship between hardness and flow stress, with the flow stress varied by different grain sizes and by strain-hardening. He studied EN2 steel (elemental compositions are given). Different grain sizes were obtained by annealing specimens in the range of 950ºC-1250ºC, followed by cooling at various rates through the critical range and a final anneal for 20h at 650ºC. The largest grain size was obtained by strain annealing. The method of measuring the grain sizes is not given. All his data was plotted against $d^{-1/2}$ and given linear fits. In Fig.2.1 we plot his data for the flow stress of strained at 2.5%, 10% and 18.25% (Fe (5) green open triangles).

Douthwaite and Evans [65] (1973) studied 2.9% Si-steel with grain sizes varied by vacuum annealing between 650ºC and 1150ºC. Micro-strain was obtained by tensile loading to below the yield point. Slip lines and grain boundaries were observed by optical microscopy after etching. The yield point was measured at 77K and 298K and they plotted their data with linear fits to $d^{-1/2}$ They followed Kelly (1966) in considering that elastic anisotropy can give rise to the $d^{-1/2}$ dependence. We plot their data in Fig.2.1 as Fe (2) red filled triangles.

More recently, Kashyap and Tangri [66] (1997) report tensile experiments at room temperature on 416L stainless steel. The specimens were vacuum annealed at temperatures from 900ºC to 1300ºC to obtain grain sizes from 3.1 to 104μm. Both optical and transmission electron microscopy were used to measure the grain size. Tensile testing was carried out with a strain rate of $1\times10^{-4}s^{-1}$ at room temperature and at 400ºC and 700ºC. We plot their room temperature flow stress data at the yield point and 2%, 5%, 10%, 20% and 30% strain (Fe (4) purple open circles) in Fig.2.1. Kashyap and Tangri were interested in the variation of the Hall-Petch parameters $\sigma_0$ and $k_{HP}$ of

Eq.2.1 with strain. They considered the slip-distance model of Conrad [52] and the anisotropy model of Ashby [2], both of which predict $k_{HP} \propto \varepsilon^{1/2}$, but their data showed a much smaller strain sensitivity.

Agraie-Khafri *et al*. [59] (2012) also studied stainless, hot rolled AISI 301 sheet. After annealing for an hour at various temperatures 800–1200ºC and forced-air-cooling, they measured grain sizes by both ultrasonic attenuation and by polishing and etching, and reported grain size distributions. Uniaxial tensile test data at the yield point were plotted and fitted with $x = 0.66$. Their data is plotted in Fig.2.1 (Fe (3) red solid squares).

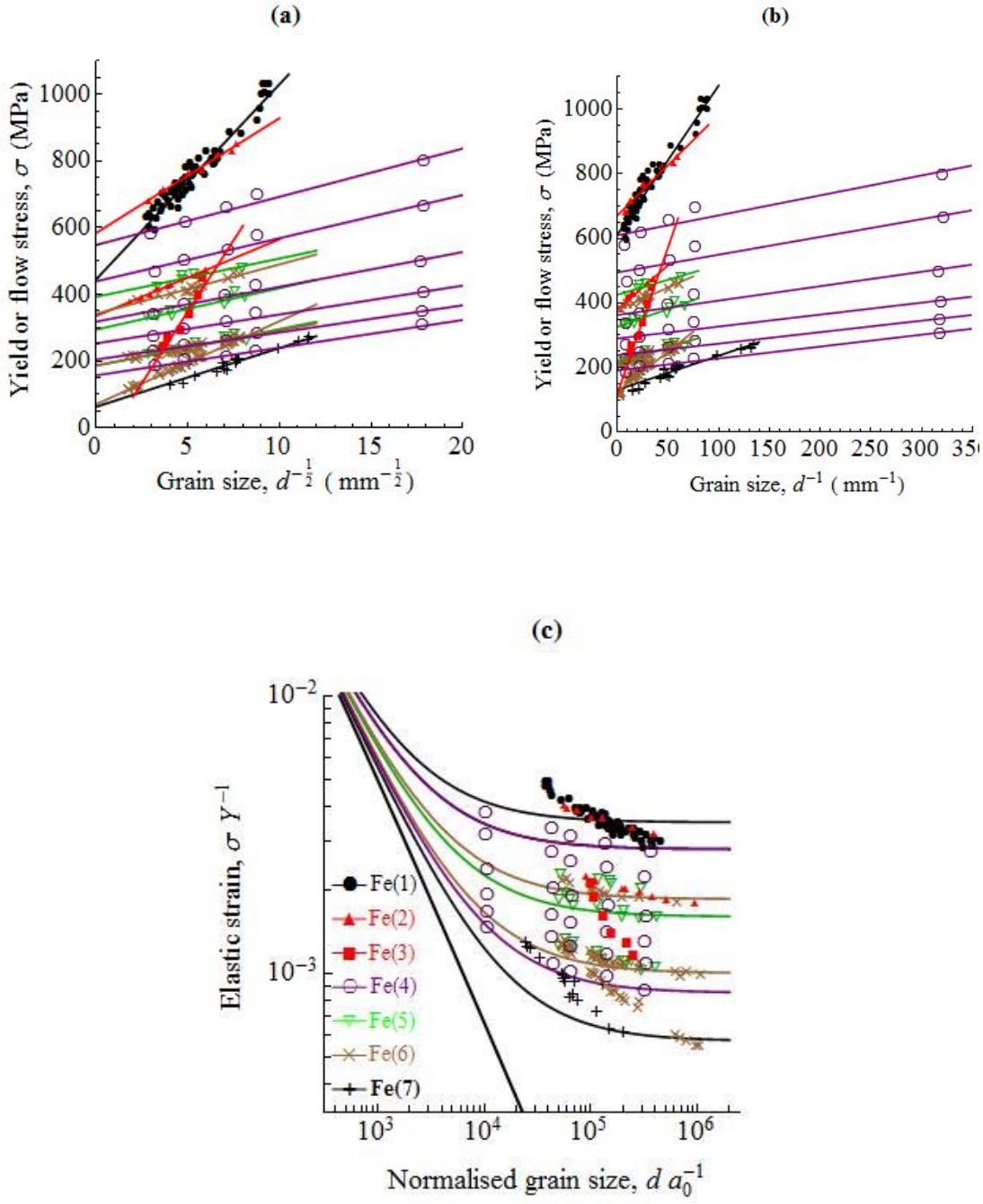


**Fig.2.1 Datasets for iron, steel and silicon steel are plotted against (a) the inverse square-root of grain size, (b) the simple inverse of grain size, and (c) in normalised form on a double logarithmic plot. The normalization constants: $Y$=211GPa, $a_0$=0.287nm. In (a), the solid lines are fits to Eq.2.1; in (b) the solid lines are fits to Eq.2.3 with the exponent $x$= -1; in (c) the solid lines are plots of Eq.2.2 with k = 0.72 and $\sigma_0$ chosen so the lines for each dataset are below most of the data. The heavy black line is for Eq.3.2 with $\sigma_0$ = 0. Fe(1) is the classic dataset of**

**Petch (1953); Fe(2) represent the silicon steel datasets from Douthwaite and Evans (1973); Fe(3) is data from Agraie-Khafri et al. (2012); Fe(4) are data sets for 316L stainless steel from Kashyap and Tangri (1997); Fe(5) come from the EN2 steel datasets in Douthwaite (1970); Fe(6) represent data sets from Armstrong (1962); Fe (7) is the classic dataset of Hall (1951).**

**Table 2.1 The knowledge of Fe data from the original references. (N.G. is Not Given)**

<table>
<tr><th rowspan="2">Data</th><th rowspan="2">Strain</th><th rowspan="2">Texture</th><th rowspan="2">Twinning</th><th colspan="2">Crystallography of slip</th><th rowspan="2">Work hardening</th></tr>
<tr><th>Slip plane</th><th>Slip direction</th></tr>
<tr><td>Fe(1)</td><td>Yield</td><td>N.G.</td><td>N.G.</td><td rowspan="15">{110}<br>{211}<br>{321}</td><td rowspan="15">< $\bar{1}$11 ></td><td>Not reported</td></tr>
<tr><td>Fe(2)</td><td>Yield</td><td>N.G.</td><td>N.G.</td><td>Not reported</td></tr>
<tr><td>Fe(3)</td><td>Yield</td><td>N.G.</td><td>N.G.</td><td>Not reported</td></tr>
<tr><td rowspan="5">Fe(4)</td><td>Yield</td><td rowspan="5">N.G.</td><td rowspan="5">N.G.</td><td rowspan="5">See Fig.2.1 Fe(4)</td></tr>
<tr><td>2%</td></tr>
<tr><td>5%</td></tr>
<tr><td>10%</td></tr>
<tr><td>20%</td></tr>
<tr><td rowspan="3">Fe(5)</td><td>30%</td><td rowspan="3">N.G.</td><td rowspan="3">N.G.</td><td rowspan="3">See Fig.2.1 Fe(5)</td></tr>
<tr><td>2.5%</td></tr>
<tr><td>10%</td></tr>
<tr><td rowspan="3">Fe(6)</td><td>18.25%</td><td rowspan="3">N.G.</td><td rowspan="3">N.G.</td><td rowspan="3">See Fig.2.1 Fe(6)</td></tr>
<tr><td>Yield</td></tr>
<tr><td>2.5%</td></tr>
<tr><td>Fe(7)</td><td>20%</td><td>N.G.</td><td>N.G.</td><td>Not reported</td></tr>
</table>

**ii Brass**

For brass and copper, $Y$=115GPa, $a_0$=0.361nm are used as normalization constants. The oldest datasets come from Bassett and Davis [67] (1919) and Babyak and Rhines [68] (1960); neither of these papers presented plots of data against $d^{-1/2}$. Jindal and Armstrong [69] (1967) replotted these datasets. Armstrong and Elban [70] (2012) also reported that Mathewson [71](1919) fitted an inverse fourth-root to the data of Bassett and Davis. In Fig.2.2 we plot the Bassett and Davis data for 68-32 (B (1) red circles) and 69-31 (B (2) red crosses) brass and the Babyak and Rhines data for 70-30 brass (B (3) green filled triangles), taken from Jindal and Armstrong [69].

Armstrong et al. [62] (1962) also presented data for the flow stress of 70-30 brass at the yield point and at 2%, 5%, 10% and 20% strain. The grain size was varied by vacuum annealing at temperatures from 400ºC to 800ºC; how the grain size was measured was not stated. In Fig.2.2 we plot their data for the flow stress of 70-30 brass at yield stress and at 20% strain (B (4) blue crosses); the data at intermediate strains follows parallel regularly spaced lines.

Douthwaite [64] (1970) also reports data for 70-30 brass. The grain size range was obtained by annealing for different times in the range 450-950ºC. However, the method of measuring the grain sizes is not given. Tensile tests were carried out at a strain rate of $2\times10^{-4}$ $s^{-1}$. Data for the yield stress and the flow stress at 5% and 7.5% strain are given, and are plotted in Fig.2.2 (B (5) black open squares).

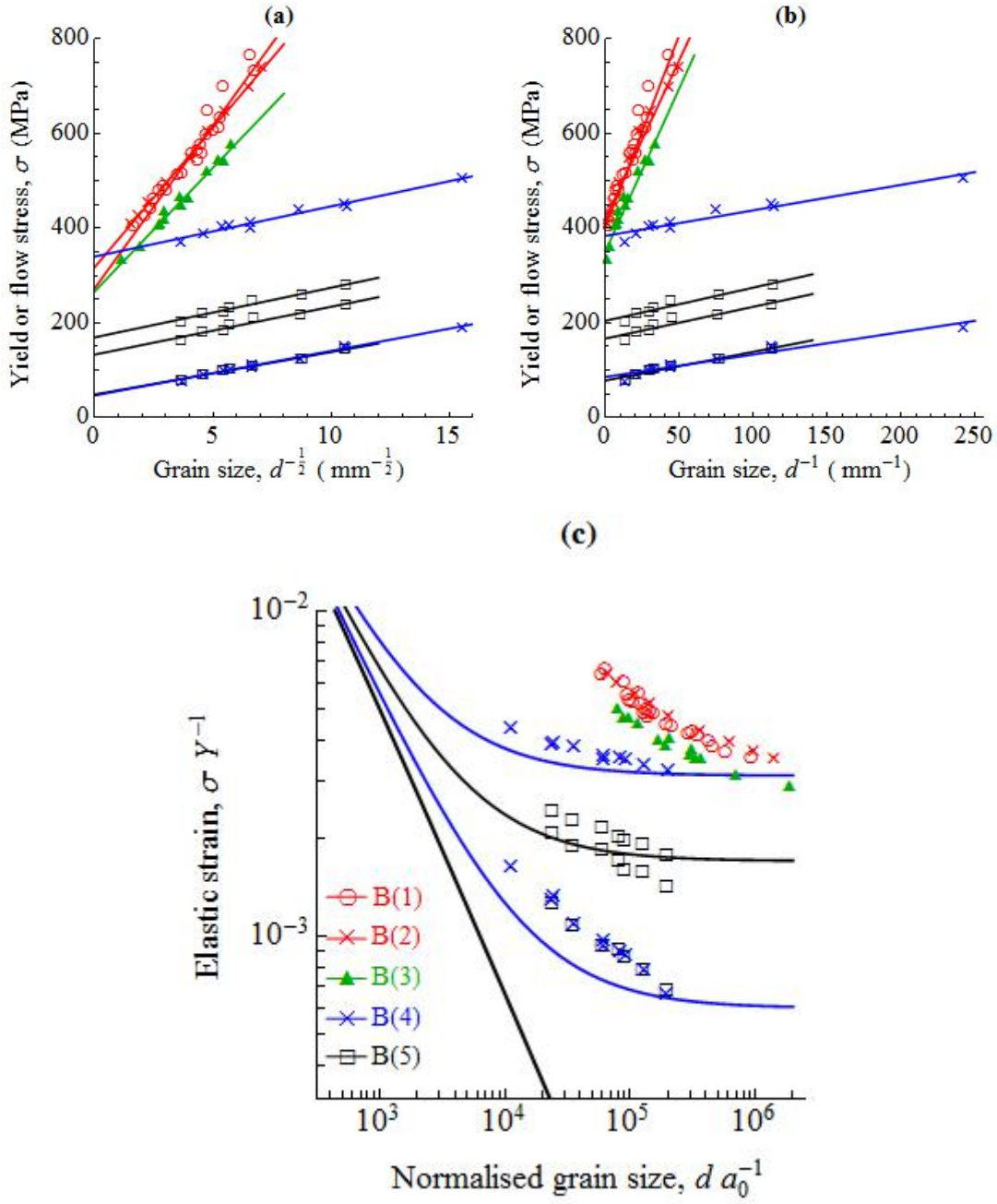


**Fig.2.2 Datasets for brass are plotted against (a) the inverse square-root of grain size, (b) the simple inverse of grain size, and (c) in normalised form on a double logarithmic plot. The normalization constants: $Y$=115GPa, $a_0$=0.361nm. B(1) and B (2) are Bassett and Davis (1919) data for 68-32 and 69-31 brass; B (3) is Babyak (1960) data for 70-30 brass; B(4) are the Armstrong (1962) 70-30 brass data at yield stress and at 20% strain; B(5) are the data sets from Douthwaite (1970) for the yield stress and the flow stress at 5% and 7.5% strain. The solid curves are as in Fig.2.1.**

**Table 2.2 The knowledge of Brass data from the original references. (N.G. is Not Given)**

| Data | Strain | Texture | Twinning | Crystallography of slip | | Work hardening |
|---|---|---|---|---|---|---|
| | | | | Slip plane | Slip direction | |
| Brass(1) | Yield | N.G. | N.G. | {111} | $< 1\bar{1}0 >$ | Not reported |
| Brass(2) | Yield | N.G. | N.G. | | | Not reported |
| Brass(3) | Yield | N.G. | N.G. | | | Not reported |
| Brass(4) | Yield | N.G. | N.G. | | | See Fig.2.2 B(4) |
| | 20% | | | | | |
| Brass(5) | Yield | N.G. | N.G. | | | See Fig.2.2 B(5) |
| | 5% | | | | | |
| | 7.5% | | | | | |

### iii Copper

Feltham and Meakin [72] (1957) reported data for copper at 0.5% strain. Tensile specimens of oxygen-free copper (99.9911%) were annealed for various periods in vacuum, in the range 500–700°C. Grain size measurements are not described. Armstrong et al. (1962) plotted this data with a linear fit to $d^{-1/2}$, and we have replotted this data from Armstrong et al. in Fig.2.3 (Cu (3) green filled circles).

Hansen [73] (1982) reported tensile test data for 99.999% copper. The copper was reduced by cold drawing and recrystallized at temperatures from 300-400ºC for 1h. The recrystallized grain size was further increased by annealing at temperatures from 500-600ºC. The grain size was determined by optical microscopy and specimens having grain sizes of 8.5, 25 and 60μm were examined. Tensile testing was carried out with a strain rate of $7\times10^{-4}s^{-1}$, and after straining, detailed electron microscopy was carried out to elucidate the mechanisms of grain boundary hardening. We plot their data in Fig.2.3 for measurements at liquid nitrogen temperature and room temperature at 5%, 10% and 20% strain, indicated by Cu (1) red and Cu (2) black filled circles respectively.

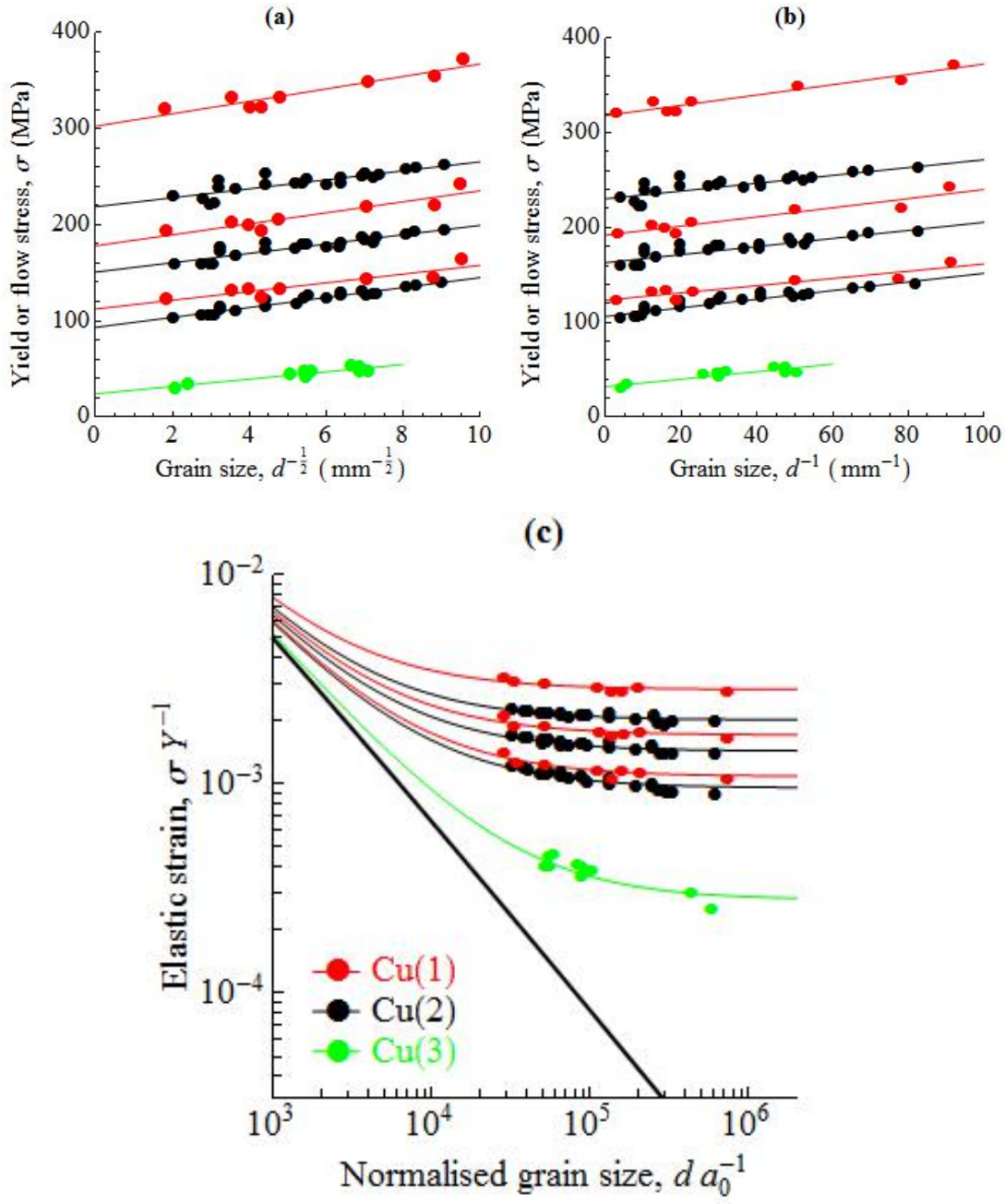


**Fig2.3 Data sets for copper are plotted against (a) the inverse square-root of grain size, (b) the simple inverse of grain size, and (c) in normalised form on a double logarithmic plot. The normalization constants: $Y$=115GPa, $a_0$=0.361nm. Cu(1) and Cu(2) are data sets from Hansen and Ralph (1982) liquid nitrogen temperature and room temperature at 5%, 10% and 20% strain, respectively; Cu(3) indicate the data for copper at 0.5% strain from Armstrong et al. (1962). The solid curves are as in Fig.2.1.**

**Table 2.3 The knowledge of Cu data from the original references. (N.G. is Not Given)**

| Data | Strain | Texture | Twinning | Crystallography of slip | | Work hardening |
|---|---|---|---|---|---|---|
| | | | | Slip plane | Slip direction | |
| Cu(1) | 5% | Reported | N.G. | {111} | $<1\bar{1}0>$ | See Fig.2.3 Cu(1) |
| | 10% | | | | | |
| | 20% | | | | | |
| Cu(2) | 5% | Reported | N.G. | | | See Fig.2.3 Cu(2) |
| | 10% | | | | | |
| | 20% | | | | | |
| Cu(3) | Yield | N.G. | N.G. | | | Not reported |

### iv Tungsten, Titanium, Chromium

With only one or two datasets per metal, we consider W, Ti and Cr together. Three hardness test datasets were transfer to yield or flow stress by dividing the coefficient 2.8. The normalization constants: for tungsten, $Y$=411GPa, $a_0$=0.316nm; for chromium, $Y$=279GPa, $a_0$=0.228nm; for titanium, $Y$=116GPa, $a_0$=0.295nm.

Vashi *et al.* [74] (1970) consolidated 0.05μm tungsten powder material at a pressure of 1GPa for 10min at temperatures of 820ºC, 870ºC and 920ºC. The grain sizes ranged from 0.15μm to 10μm, measured by both optical metallography and electron microscopy. Hardness testing was performed with indentation sizes always large compared with the grain sizes. Their data is plotted in Fig.2.4 (W black circles).

Chromium hardness data is given by Brittain *et al.* [75] (1985). Specimens of different grain size were prepared by electrodeposition. The method of measuring the grain sizes is not given. The diamond pyramid hardness values they report are plotted in Fig.2.4 (Cr blue crosses).

Hu and Cline [76] (1968) reported micro-hardness tests on titanium. The raw material was repeatedly cold-rolled and recrystallized by vacuum annealing. After the specimen

preparation, the various grain sizes were obtained by a final anneal at various temperatures, and measured by both optical and transmission-electron microscopy. Their data is plotted in Fig.2.4 (Ti (1) red crosses).

Jones and Conrad [77] (1969) studied tensile test data for alpha-Titanium at room temperature. Commercial purity (A-70) titanium was supplied as 1/4 inch in diam centerless-ground rod. The raw rods were cold-swaged to 0.078 inch in diam wires and 2 inch lengths were recrystallized in a vacuum of -$5\times10^{-5}$ torr, giving grain sizes in the range 0.8 to 30μm. The grain size values are obtained from mean linear intercept method and measurements were made using conventional optical techniques. Data for the 4% strain flow stress are plotted in Fig.2.4 (Ti (2) red filled circles).

It is interesting to note that in Fig.4a and Fig.4b titanium appears to have a much weaker Hall-Petch effect than tungsten or chromium. However, this is just an effect of its much lower Young's modulus, for in the normalised plot of Fig.4c, it is not far away from tungsten or chromium.

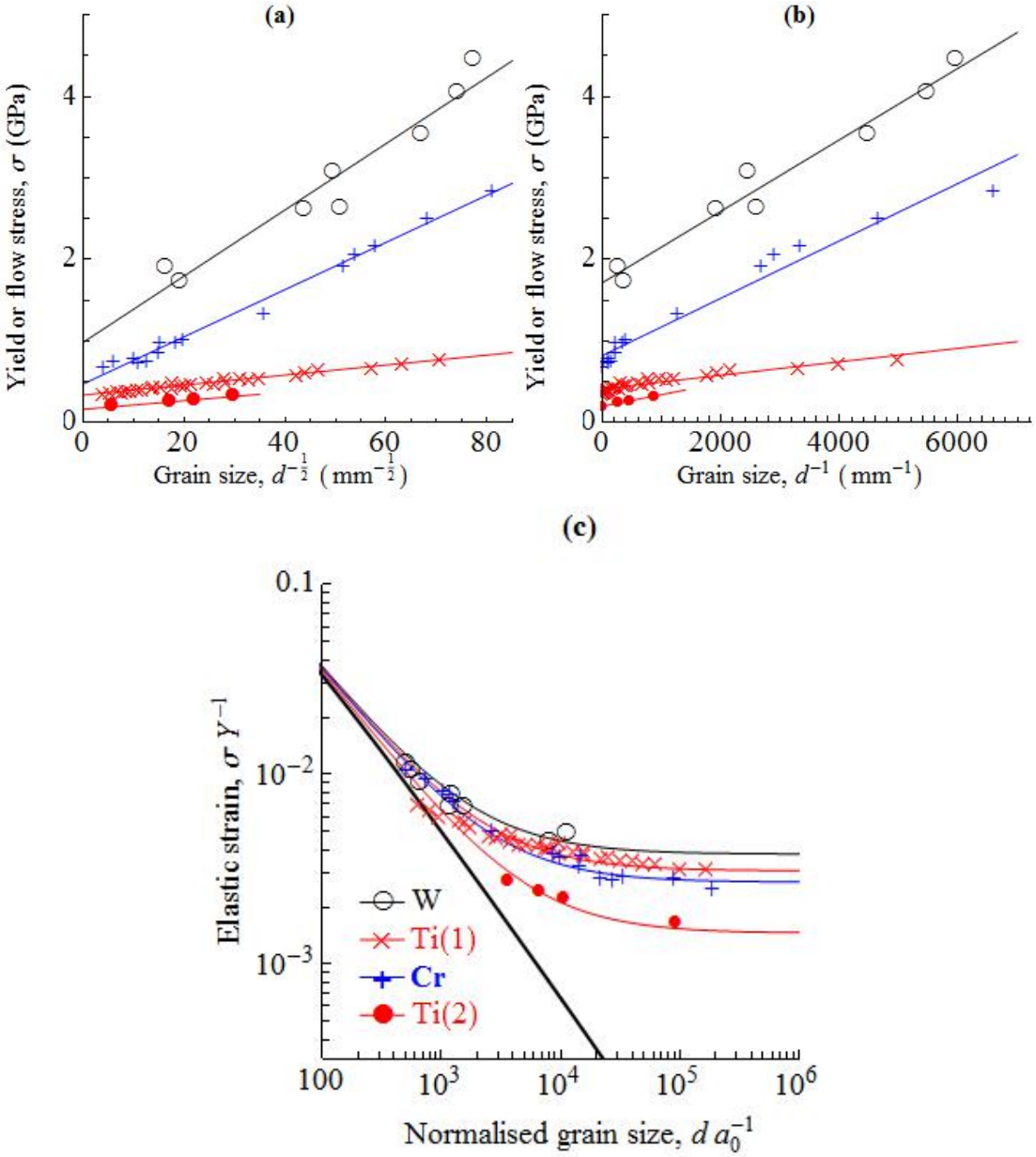


**Fig.2.4 W Data for tungsten Vashi et al. (1970); Ti(1) Data from titanium Hu and Cline (1968); Cr Data is chromium Brittain et al (1985); Ti(2) Data reproduced from titanium Jones and Conrad (1969) are plotted against (a) the inverse square-root of grain size, (b) the simple inverse of grain size, and (c) in normalised form on a double logarithmmic plot. The normalization constants: for tungsten, $Y$=411GPa, $a_0$=0.316nm; for chromium, $Y$=279GPa, $a_0$=0.228nm; for titanium, $Y$=116GPa, $a_0$=0.295nm. The solid curves are as in Fig.2.1.**

**Table 2.4 The knowledge of W, Cr and Ti data from the original references. (N.G. is Not Given)**

| Data | Strain | Texture | Twinning | Crystallography of slip | | Work hardening |
|---|---|---|---|---|---|---|
| | | | | Slip plane | Slip direction | |
| W | N.G. | N.G. | N.G. | {110}&{211} | $< \bar{1}11 >$ | Not reported |
| Cr | N.G. | N.G. | N.G. | {110}&{211} | $< \bar{1}11 >$ | Not reported |
| Ti(1) | N.G. | N.G. | N.G. | {0001} $\{10\bar{1}1\}$ | $< 11\bar{2}0 >$ | Not reported |
| Ti(2) | 4% | N.G. | N.G. | $\{10\bar{1}0\}$ | | Not reported |

**v Silver, Gold, Nickel**

For silver, $Y$=83GPa, $a_0$=0.409nm are used. Aldrich and Armstrong [29](1970) reported a silver data over a wide range of grain size between 1 and 60μm. Specimens of cold-rolled sheet material of purity 99.9% were annealed in air at temperatures from 100ºC to 900ºC for 0.5 hr. The grain size measurement include both optical and electron microscope. The grain size was calculated by three-halves the mean linear intercept. Tensile testing rate was 0.0667 $min^{-1}$. Their datasets included the yield stress, the flow stress at 0.2%, 5% and 20% strain and the fracture stress. The yield stress ( Ag(2) green circles) and flow stress at 20% strain ( Ag(1) green crosses) is shown in Fig.2.7. In the original paper, the author compared linear fits to $d^{-1}$, $d^{-1/2}$ and $d^{-1/3}$,The final conclusion is $d^{-1/2}$ fitted best, they excluded the $d^{-1/3}$ fit because it gives a negative intercept on the y-axis. The negative stress intercept was considered unphysical. However, we found that the datasets Fe(3), Au, Al(4) and Al(5) also have the negative y-axis intercept in the $d^{-1/2}$ fits.

For gold data, we use $Y$=79GPa, $a_0$=0.408nm. Emery [78] (2003) reported a tensile testing data of gold thin films. The films specimens were made by electron beam or thermal evaporation, the thickness ranging from 0.2-2.1μm. The samples were annealed for 10, 30 and 60 second at 800ºC. The film microstructure and morphology were measured by scanning ion microscopy. The grain size were calculated by eye in SIM

images. The testing strain rate was $6\times10^{-5}s^{-1}$. They concluded flow strength was generally consistent with the Hall-Petch relationship. However, we can see the parabola-shape of the fitting with eye observation. We reproduced this data in the Fig.2.7 with red triangle.

For nickel data, $Y$=200GPa, $a_0$=0.352nm are used. Thompson [79] (1977) reported a nickel data. This data is a study of work-hardening. The small grain size specimens were obtained by electroplating from a high-purity bath and then annealing at various temperatures. Grain sizes of 80μm and larger came from swaged and annealed material. Grain size measurements are not described. Tensile tests were conducted at the strain rate of $8.3\times10^{-4}$ $s^{-1}$. They only gave a log-log plot showed a slope of 0.367 for grain sizes above 1 μm. We plot Thompson's data for yield stress in Fig.2.7 ( Ni(1) blue filled squares).

Keller and Hug [80] (2008) reported tensile tests on nickel specimens with a thickness to grain size ratio $t/d$ between 1.3 and 15. Specimens of 99.98% wt.% purity were annealed in vacuum for 220 min at temperatures between 600ºC and 1050ºC and then air cooled. The grain size and weak texture were revealed by electron back-scattered diffraction (EBSD). Uniaxial tensile tests were conducted at a strain rate of $2.4\times10^{-4}$ $s^{-1}$. At yield stress, they observed a normal Hall-Petch behaviour for all $t/d$ values and this data is reproduced in Fig.2.7 (Ni (2) blue crosses).

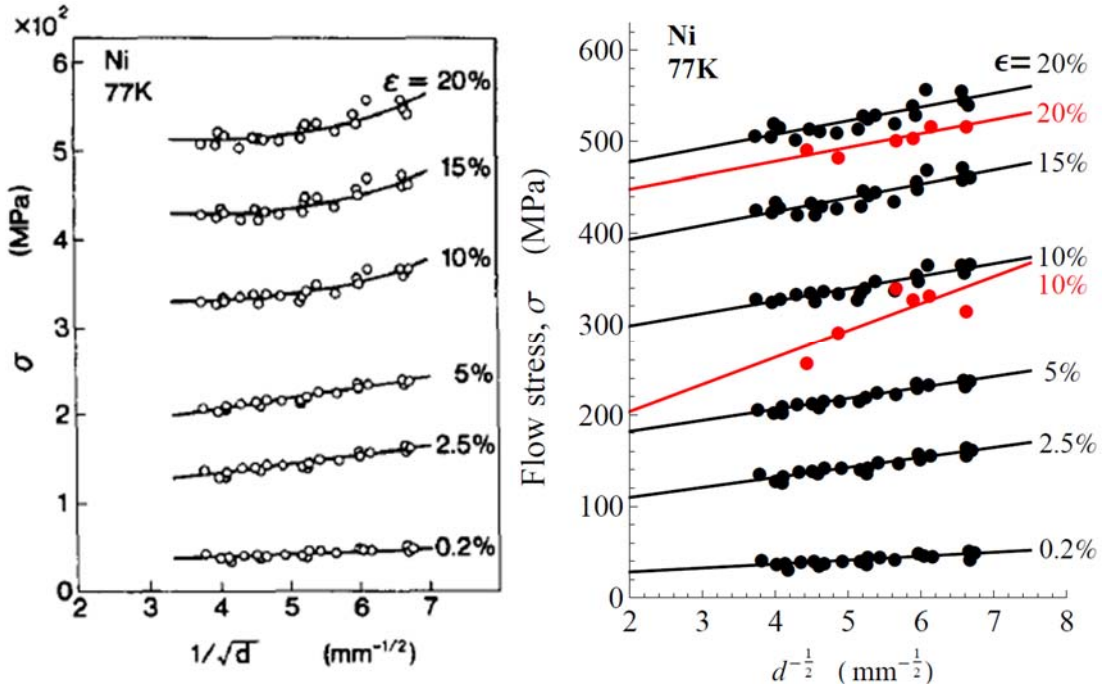


**(a)** **(b)**

**Fig.2.5 (a) The reproduced original Hall-Petch type plot of flow stress for Ni data. (b) The linear fitting of both the mechanical flow stress data and electrical resistivity method data. The black filled circles indicated the flow stress data points of (a), the red filled circles represented the electrical resistivity measurements data which reproduced from the Fig.5 and Fig.8 of the original reference [30], 10% and 20% strain at 77K data were reproduced.**

Narutani and Takamura [30] (1991) reported wire tension data on nickel. This is a very interesting paper, which has been cited as supporting the Ashby equation (Brown, Argon). The detail of modified Ashby equation will be discussed in section 2.2.2. The 99.99% purity Ni samples were re-crystallized at temperatures between 475ºC and 1000ºC. The grain sizes ranging from 20 to 90μm. The tensile tests were carried out at a strain rate of $3.0\times10^{-4}\ s^{-1}$ at 77 and 295K. The Hall-Petch plot data were obtained from the deformation at 77K. The author concluded that for small strains (below 5%), the plot follow a linear relation between the flow stress and the inverse square root of grain size. However, for larger strains, the fitting were clearly deviating from the Hall-Petch equation, as shown in Fig.2.5 (a). The effect of dislocation density on flow stress were also investigated, irrespective of grain size.

The dislocation density were obtained by the measurement of electrical resistivity. It was found that the flow stress is proportional to the square root of dislocation density. The linear relationship was also obtained between dislocation density and the reciprocal of grain size [30]. We reproduced both the mechanical testing data and electrical resistivity data. The datasets are fitted with linear equation, which are shown in Fig.2.5 (b). The black filled circle are the Hall-Petch data produced by mechanical testing method (Fig.2.5 (a)). The red filled circle represent the data obtained by means of electrical resistivity which reproduced from the Fig.5 and Fig.8 of the original reference [30]. Only 77K datasets were reproduced for the comparison of the mechanical testing results. The red data corresponding well with the black data, which indicate the measurement of electrical resistivity is a very good method to obtain the Hall-Petch type data. From the Fig.2.5 (b), it is found that the linear fittings for the high strain data (10%, 15% and 20%) are equally good as the lower strain fitting. All of the data are also fitted with simply inverse grain size function and free exponent function. The fitting parameters are given in table 2.5.

**Table 2.5. The fitting parameters of Hall-Petch equation, reciprocal grain size equation and free exponent fitting equation to Narutani's Ni data.**

| | $\sigma = \sigma_0 + \frac{k_{HP}}{d^{1/2}}$ | | $\sigma = \sigma_0 + \frac{k_{HP}}{d}$ | | $\sigma = \sigma_0 + \frac{k_{HP}}{d^n}$ | | |
|---|---|---|---|---|---|---|---|
| Data $\varepsilon$ | $\sigma_0$ | $k_{HP}$ | $\sigma_0$ | $k_{HP}$ | $\sigma_0$ | $k_{HP}$ | $n$ |
| 0.2% | 19.812 | 4.298 | 30.843 | 0.406 | 19.659 | 4.236 | 1.2±2.6 |
| 2.5% | 87.944 | 10.929 | 115.883 | 1.037 | 87.469 | 10.836 | 1.0±1.3 |
| 5% | 158.000 | 12.016 | 188.781 | 1.136 | 158.051 | 12.016 | 0.5±1.0 |
| 10% | 270.664 | 13.696 | 305.174 | 1.318 | 272.795 | 12.746 | 1.9±1.7 |
| 15% | 363.043 | 15.114 | 400.896 | 1.461 | 364.721 | 14.257 | 1.6±1.7 |
| 20% | 447.470 | 15.026 | 484.934 | 1.458 | 447.165 | 14.565 | 1.6±1.9 |

According to Eq.13 of Narutani's paper [30], the $k_{HP}$ values should proportional with the square root strain at the low strain (0.2%, 2.5% and 5%). Hence, the $k_{HP}$ values were plotted against square root strain from the data of Table 2.5, as shown in Fig.2.6. The red filled circles are low strain data, the red crosses are high strain data, and the black line is linear relationship indicated by Eq.13 of Narutani's paper. It is found that with increased of the square root strain values, the $k_{HP}$ values increased but not followed the linear relationship. At the high strain region (10%, 15% and 20%), there is nearly no effect of strain on $k_{HP}$ values. The free exponent fitting results show that the most of the exponents are greater than 1 but with the very big error.

From the fitting results, it can be concluded that the electrical resistivity measurement provide a very good method to investigate the effect of dislocation density and grain size on flow stress. However, the datasets cannot confirm the theory cited by the author.

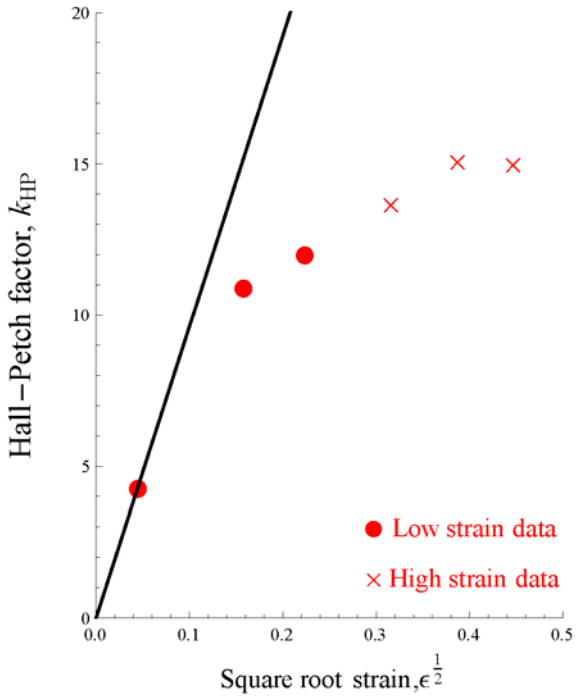


**Fig.2.6 The $k_{HP}$ values were plotted against square root strain from the data of Table 2.5. The red filled circles are low strain data, the red crosses are high strain data, and the black line is linear relationship indicated by Eq.13 of Narutani's paper [30].**

In the Fig.2.7, Narutani's data is shown as the brown triangle.

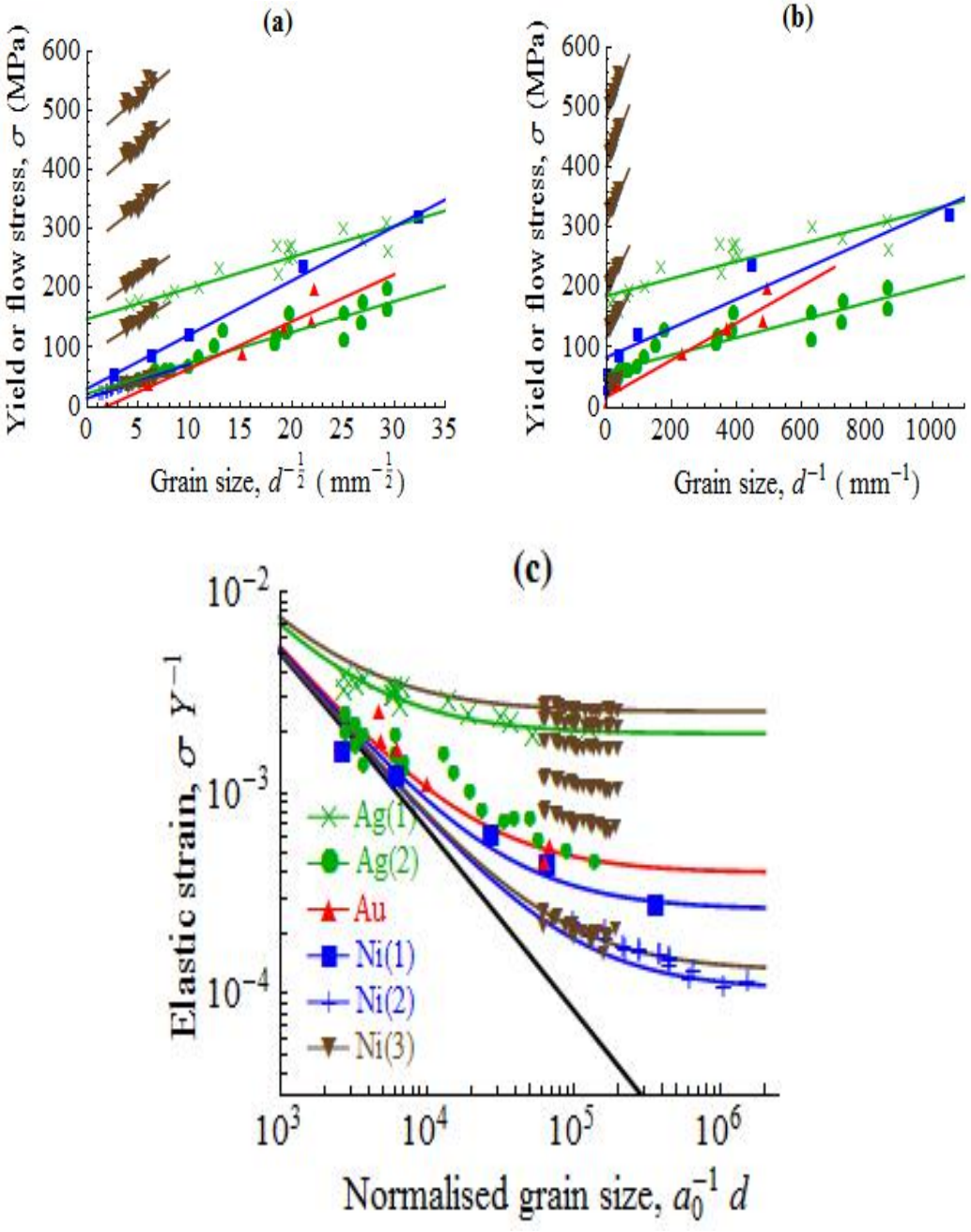


**Fig.2.7 Data for silver, gold and nickel are plotted against (a) the inverse square-root of grain size, (b) the simple inverse of grain size, and (c) in normalised form on a double logarithmic plot. The normalization constants: for silver, *Y*=83GPa, $a_0$=0.409nm; for gold, *Y*=79GPa, $a_0$=0.408nm; for nickel, *Y*=200GPa, $a_0$=0.352nm. Ag(1) and Ag(2) indicated the silver data of Aldrich and Armstrong (1970) at 20% strain and yield stress; Ni(1) is the data set of Thompson (1977); Ni(2) from Keller and Hug (2008); Ni(3) from Narutani & Takamura (1991). The solid curves are as in Fig.2.1.**

**Table 2.6 The knowledge of Ag, Au and Ni data from the original references.(N.G. is Not Given)**

| Data | Strain | Texture | Twinning | Crystallography of slip | | Work hardening |
|---|---|---|---|---|---|---|
| | | | | Slip plane | Slip direction | |
| Ag(1) | 20% | N.G. | N.G. | {111} | $<1\bar{1}0>$ | See Fig.2.6 Ag(1) & Ag(2) |
| Ag(2) | Yield | N.G. | N.G. | | | |
| Au | Yield | Reported | N.G. | | | Not reported |
| Ni(1) | Yield | N.G. | N.G | | | Reported |
| Ni(2) | Yield | N.G. | N.G. | | | Reported |
| Ni(3) | Yield | N.G. | N.G. | | | See Fig.2.5 & Fig.2.6 Ni(3) |
| | 2.5% | | | | | |
| | 5% | | | | | |
| | 10% | | | | | |
| | 15% | | | | | |
| | 20% | | | | | |

**vi Aluminium**

The normalization constants used for aluminium data are $Y$=70GPa, $a_0$=0.316nm. Carreker and Hibbard [81] (1955) reported tensile tests on wires made from two batches of aluminium both of 99.987% purity (elemental compositions given). Samples were annealed in air for 1h at temperatures from 300ºC to 500ºC. Grain sizes were measured by optical microscopy. Tensile tests were carried out at a strain rate of $0.66\times10^{-4}$ $s^{-1}$ at various temperatures down to 20K. They presented log-log plots; at 300K, 5% strain the flow stress scarcely depends on grain size while at 1% strain the slope is close to *-1/2*. We reproduce their data for 300K at 1% strain in Fig.2.8 (Al (3) red crosses); their data for yield is very similar.

Hansen [27] (1977) reported tensile test data for two grades of aluminium, purities

99.999% and 99.5%. The material was reduced by cold rolling or drawing and annealed at temperatures from 300ºC to 625ºC. The recrystallized grain sizes were determined by optical microscopy in polarized light. Tensile tests were carried out at a strain rate of $0.66\times10^{-4}$ $s^{-1}$. After the tests, the grain sizes of the specimens at 0.5%, 5% and 10% strain were measured by electron microscopy. The data for five strains from 0.2% to 20% are reproduced in Fig.2.8 (Al (1) blue open circles & Al (2) green open squares for the low-purity and high-purity materials respectively).

Tsuji et al. [82] (2002) prepared ultrafine-grained (UFG) aluminium by accumulative roll-bonding (ARB) process. Commercial purity aluminium (JIS-1100) was used for the ARB process. The material was annealed for 600 s or 1800 s at temperatures from 373 K to 673 K. The resulting grain sizes were measured by TEM, using the mean interception method. Tensile tests were carried out at a strain rate of $8.3\times10^{-4}$ $s^{-1}$, and a linear fit to $d^{-1/2}$for the yield point. It is found that work-hardening is not enhanced but rather suppressed by ultra-grain refinement. This data is reproduced in Fig.2.8c (Al (4) green triangles).

Yu et al. [83] (2005) prepared ultrafine grained aluminium by equal channel angular extrusion of commercial purity aluminium, followed by annealing. For materials of larger grain sizes, the grain sizes were measured by EBSD. For materials of fine grain size, the grains were determined from TEM measurements. Tensile tests were conducted at a strain rate of $7.1\times10^{-4}$ $s^{-1}$, at room temperature and 77K. They reported a good fit to the inverse-square root dependence (Eq.1). These data are reproduced in Fig.2.8c (room temperature, Al (6) purple squares; 77K, Al (5) circles).

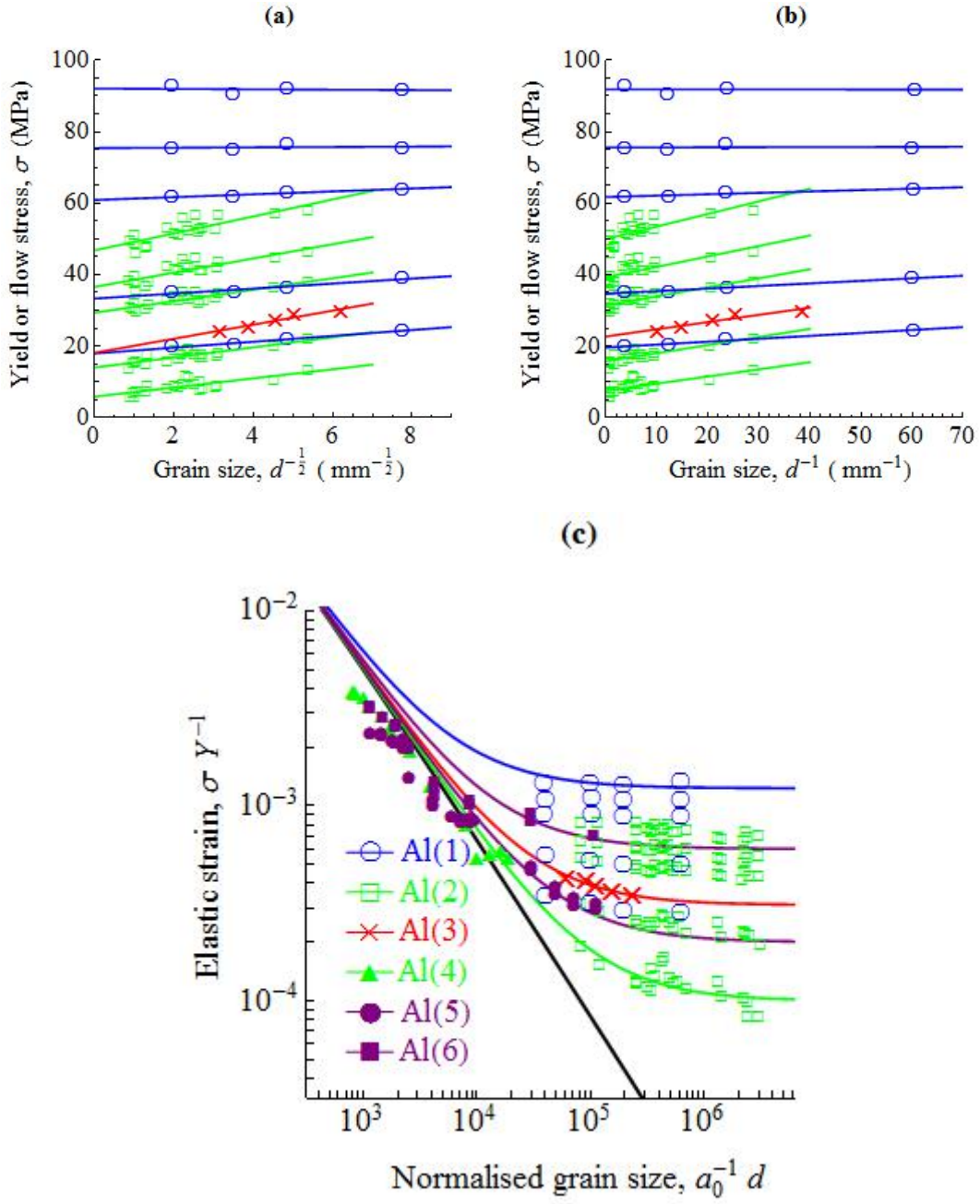


**Fig.2.8 Data for aluminium are plotted against (a) the inverse square-root of grain size, (b) the simple inverse of grain size, and (c) in normalised form on a double logarithmic plot. The normalization constants: $Y$=70GPa, $a_0$=0.316nm. Al(1) and Al(2) are from Hansen (1977) for 99.5% and 99.999% aluminium at 0.2, 1, 5, 10, 20% strain at room temperature; Al(3) show the Carreker and Hibbard (1957) aluminium data; Al(4) are the data of Tsuji et al. (2002); Al(5) and Al(6) come from Yu et al. (2005) at 77K and at room temperature, respectively. The solid curves are as in Fig.2.1.**

**Table 2.7 The knowledge of Al data from the original references. (N.G. is Not Given)**

| Data | Strain | Texture | Twinning | Crystallography of slip | | Work hardening |
|---|---|---|---|---|---|---|
| | | | | Slip plane | Slip direction | |
| Al(1) | Yield | N.G. | N.G. | {111} | $<1\bar{1}0>$ | See Fig.2.7 Al(1) |
| | 1% | | | | | |
| | 5% | | | | | |
| | 10% | | | | | |
| | 20% | | | | | |
| Al(2) | Yield | N.G. | N.G. | | | See Fig.2.7 Al(2) |
| | 1% | | | | | |
| | 5% | | | | | |
| | 10% | | | | | |
| | 20% | | | | | |
| Al(3) | 1% | N.G. | N.G. | | | Reported |
| Al(4) | Yield | Reported | N.G. | | | Reported |
| Al(5) | Yield | N.G. | N.G. | | | Reported |
| Al(6) | Yield | N.G. | N.G. | | | Reported |

## 2.2.2 Comprehensive comparison

Brown recommended the modified Ashby equation [84], which is expressed as

$$\sigma = \sigma_0 + M\alpha\mu b\sqrt{\rho(\varepsilon) + \frac{A\varepsilon}{L}} \tag{2.4}$$

where $\sigma_0$ is the corresponding bulk yield stress or large single crystals, $M$ is the Taylor factor, which can convert the shear stress to the tensile flow stress. The Taylor factor acts as an isotropic interpretation of the crystalline anisotropy at the continuum level, and $M=\sqrt{3}$ for an isotropic solid, $M=3.06$ for FCC polycrystalline metals [85], $M_{ave}\approx 3$ for BCC polycrystalline metals [86], $\alpha$ is the forest hardening constant related

to the crystal and grain structure and generally ranging from 0.1 to 0.5, a value of 1/3 was suggested by Brown [84], $\mu$ is the elastic shear modulus, $b$ is the magnitude of the Burgers vector. The constant $A$ results from averaging the Schmidt factors $S$ of the polycrystalline array and for planar glide in f.c.c. and b.c.c. ductile crystal structures, the calculation of constant $A$ is given by $A = \frac{\pi}{b}\sqrt{\frac{< S^4 > - < S^2 >^2}{< S^2 >^2}}$, Brown [84] (his Eq.6) gave the value is about equal to $\frac{0.53}{b}$.

By considering $\mu = \frac{E}{2(1+\nu)} = \frac{E}{2.6}$, the Eq.2.4 is also normalized by Young's modulus, then

$$\varepsilon_{el} = \varepsilon_0 + \frac{1}{2.6} M\alpha b\sqrt{\rho(\varepsilon) + \frac{A\varepsilon}{L}} \tag{2.5}$$

By considering 3-D density, $\frac{A\varepsilon}{L} \to \frac{3A\varepsilon}{L}$, if $\rho(\varepsilon) \ll \frac{3A\varepsilon}{L}$ ( yield or small strain), irrespective of the elastic strain $\varepsilon_0$ described bulk strength, the modified Ashby theory may also predict a minimum strength (depending on plastic strain and grain size), which is expressed as

$$\varepsilon_{el} = \frac{1}{2.6} M\alpha b\sqrt{\frac{3A\varepsilon}{L}} \tag{2.6}$$

The plastic strain $\varepsilon$ can be taken as 0.002 at yield. Substituting the values of parameters, then the Eq.2.6 is expressed as

$$\varepsilon_{el} = 4.85\times10^{-1}\sqrt{\varepsilon\frac{b}{L}} \quad \& \quad \varepsilon_Y = 2.16\times10^{-2}\sqrt{\frac{b}{L}} \tag{2.7}$$

For FCC or BCC materials, $b = \frac{\sqrt{2}}{2}a_0$ or $b = \frac{\sqrt{3}}{2}a_0$, Eq.2.7 can be written as

$$\varepsilon_{el} = 4.2\times10^{-1}\sqrt{\varepsilon\frac{a_0}{L}} \quad \& \quad \varepsilon_Y = 1.88\times10^{-2}\sqrt{\frac{a_0}{L}} \tag{2.8}$$

To compare the fitting to the normalized data by Eq.2.1, Eq.2.2, Eq.2.3 and Eq.2.8 in the same framework, the comprehensive figure of all 61 datasets is shown in Fig.2.9.

The black heavy lines are Eq.2.2 with the parameter $k = 0.72$ and $\varepsilon_0 = 0$. While the thin solid lines are Eq.2.2 with $k = 0.72$ and $\varepsilon_0$ as the single fitting parameter. The black chain-dotted lines are the Hall-Petch equation with $k_{HP}$ and $\varepsilon_0$ as free fitting parameters. The black dashed lines are the fits of Eq.2.3 with $x$=1, $k$ and $\varepsilon_0$ as free fitting parameters. The purple solid lines are the minimum strength predicted by the Eq.2.8 at yield strain $\varepsilon$ equal to 0.002. The purple chain-dotted lines are Eq.2.8 plus the elastic strain $\varepsilon_0$ which describe the bulk strength. The red heavy line and chain-dotted line in Fig.2.9 (iv) come from Eq.2.8 with $\varepsilon$ equal to 0.04, since the dataset (red circle) is 4% strain flow stress of titanium. At high strain the value of $\rho(\varepsilon)$ is important. However, only one of datasets reports the measurements of $\rho(\varepsilon)$. A value of $\rho(\varepsilon)$ is reported from resistivity measurement method for the 20% strain in Narutani's Ni data [30], a minimum strength for 20% strain using Eq.2.4 is plotted, as shown in the dark yellow line in Fig.2.9 (v). The dark yellow line is too low to predict the 20% strain Ni data very well. There are four features of Fig.2.9: (1) only quite few experimental data points locate below the black heavy line but quite near it; (2) experimental data points don't follow the Eq.2.8 prediction at small grain size, the strength of experimental data increase sharply at small grain size, however, Eq.2.8 increases gently (purple chain-dotted line); (3) the fitting of the inverse square root (black chain-dotted line) and simply inverse relationship (black dashed line) diverge significantly only outside the range of each dataset; (4) very consistently, there is a significant gap above the purple line. If the data obeyed Eq.2.4, there should be data locate in this area. If this area is about 0.3 of the total area (see Section 2.3), the probability of it being empty in all 30 yield data is $(0.7)^{30} \sim 2\times10^{-5}$.

By considering the compatibility of modified Ashby equation (Eq.2.8), the gradient value of Eq.2.8 is adjusted to make it as likely as Eq.2.2. It is found that at least a value of $3.76\times10^{-2}$ (double the original value) of gradient plus the bulk strength parameter are adopted to make the Eq.2.8 fit the yield data equally well as Eq.2.2. Except plastic strain

$\varepsilon$ , the values of Taylor factor $M$ and forest hardening constant $\alpha$ can also affected the gradient value. The Taylor factor is a fixed value for a particular type of metal, e.g. $M \approx 3$ for both FCC and BCC polycrystalline metals. Hence, the only possible changed parameter is the forest hardening constant which related to the crystal and grain structure. To describe the double gradient value of Eq.2.8, the double forest hardening constant is the most physical reasonable adjustment. In this case, a value of 0.66 of $\alpha$ is obtained. The different classic papers suggested various values of $\alpha$ ranging from 0.1 to 0.5, Taylor gave a value of $\pi^{-1} = 0.32$ [3], Ashby suggested a value of 0.3 [2], a value of 0.33 was given by Brown [84]. Comparing with the maximum value of 0.5, 0.66 is not out of range too much.

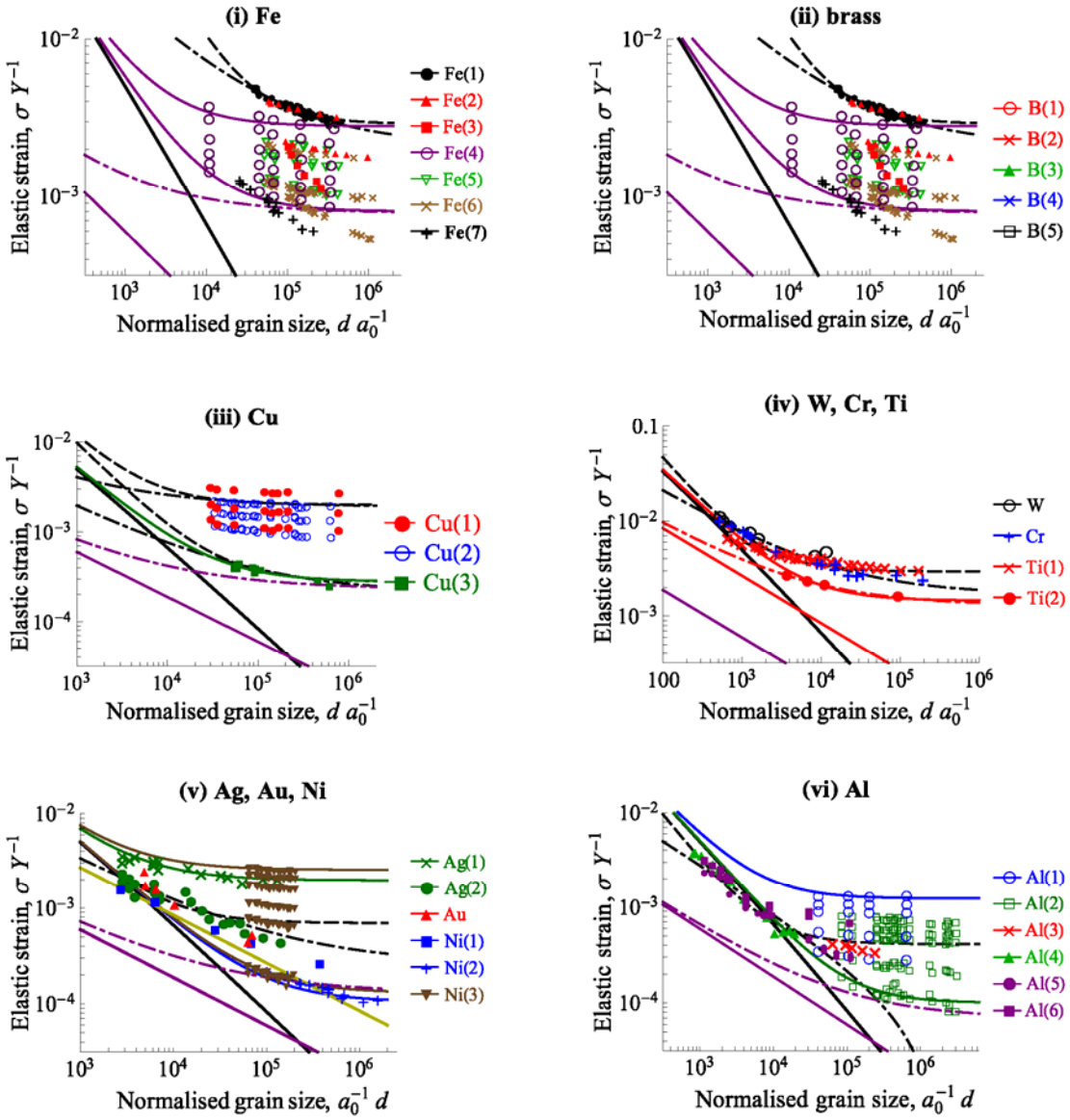


**Fig.2.9 Normalised datasets from the literature for flow or yield stress against grain size. The heavy line in all panels is for Eq.2.2 with $k$ = 0.72 and $\varepsilon_0$ = 0. The thin solid lines are for Eq.2.2 with $k$ = 0.72 and $\varepsilon_0$ as the only fitting parameter. The black dashed lines are fits using Eq.2.3 with $x$ = 1, $k$ and $\varepsilon_0$ as fitting parameters. The black chain-dotted lines are fits using Eq.2.1, normalised, so that $k_{HP}$ and $\varepsilon_0$ are the fitting parameters. The purple solid lines are the minimum strength predicted by the Eq.2.8 with the yield strain equal to 0.002. The purple chain-dotted lines are Eq.2.8 at yield strain plus the elastic strain which describe**

**the bulk strength. The red heavy line and chain-dotted line in Fig. iv come from Eq.2.8 with the plastic strain equal to 0.04. The dark yellow line in Fig. v is the plot of Eq.2.4 at 20% strain.**

## 2.2.3 Fits to the data

All of the datasets are fitted with Eq.2.1 (HP fitting), Eq.2.2 (EDC fitting) and Eq.2.3 ($x$=1 (SI fitting) and as a free-fitting parameter (EQ3 fitting)) by using the *Mathematica© NonlinearModelFit*. The $R^2$ values generally over 0.999 which means all of the fittings are quite good. It is found that the exponents of the Eq.2.3 are scatted largely. Then we choose some representative data for the detailed analysis: (1) The copper datasets because the quality of these 3 datasets are quite good, (2) Ag (1) because it was fitted by Aldrich and Armstrong [29] with the exponents of $x$=1/3, $x$=1/2 and $x$=1, (3) B (1) because many brass and steel datasets have very high values of $k_{HP}$. In the detailed analysis, the 4 additional equations are used to the fitting. They are (1) Linear equation (LIN fit), (2) Aldrich & Armstrong 1/3 exponent equation (A3 fit), (3) the power law fit (EXP fit), (4) log fit (LOG fit), respectively.

$$\begin{aligned} &\text{LIN}: \quad \sigma = \sigma_0 - cd && \text{A3}: \quad \sigma = \sigma_0 + \frac{k_{HP}}{d^{1/3}} \\ &\text{EXP}: \quad \sigma = \sigma_0 + ce^{-\alpha d} && \text{LOG}: \quad \sigma = \sigma_0 - c\ln d \end{aligned} \tag{2.9}$$

The Linear equation is clearly wrong for the explanation of the HP data, hence, the fittings are expected to provide statistical benchmarks of wrong equations fittings. A3 fitting comes from Aldrich and Armstrong. The EXP and LOG fits are used to compare the power law fits with non-power law fits. The 1-$R^2$ values of the fittings are shown in Table 2.8. The LIN fit has the expected highest values. However, for other seven model fits, all of the 1-$R^2$ values quite small and little scatted. The fitting result just confirm the Fig.2.9 conclusion: we can't distinguish which model is better. No evidence support the Hall-Petch relationship is true. The values of the exponent $x$ may prefer the Hall-Petch equation, but with quite large uncertainties.

**Table 2.8. The 1-$R^2$ values of the fittings to the eight models. All 1-$R^2$ values are in ‰. The final column is the values of the exponent by Eq.2.3.**

| Data | LIN | SI | HP | A3 | EDC | EXP | LOG | EQ3 | *x* |
|---|---|---|---|---|---|---|---|---|---|
| Cu(1) 5% | 2.1 | 0.9 | 0.5 | 0.5 | 0.8 | 0.6 | 0.6 | 0.5 | 0.3±0.16 |
| Cu(1) 10% | 1.1 | 0.7 | 0.6 | 0.6 | 0.7 | 0.6 | 0.6 | 0.6 | 0.22±0.27 |
| Cu(1) 20% | 0.9 | 0.6 | 0.5 | 0.5 | 0.6 | 0.6 | 0.6 | 0.5 | 0.35±0.39 |
| Ag(1) | 68 | 30 | 21 | 20 | 27 | 22 | 22 | 20 | 0.28±0.19 |
| B(1) | 11 | 1.4 | 1.4 | 1.8 | 1.3 | 1.5 | 3.2 | 1.1 | 0.74±0.13 |

## 2.2.4 Discussion

The comprehensive comparison Fig.2.9 suggests that fits of the 61 data to Eq.2.1 and Eq.2.2 (with or without the ln*d* term) are equally good. The fitting of the HP equation and SI equation diverge significantly only out the range of each dataset. There is no statistical result show Eq.2.1 is correct. The large scatted and variable exponent *x* in Eq.2.3 explains that there is no experimental evidence support for a power law. Eq.2.8 also suggested a minimum strength depending on the strain which corresponding well with large grain size data, however, the small grain size data are more close to the Eq.2.2 theory. We can only get one conclusion from the fitting results is that the strength decreases monotonically with the increase of the grain size.

Almost all of the Hall-Petch data points as well as micromechanical testing data on micro pillars are found above the line of Eq.2.2 with $k$~1 and $\varepsilon_0$=0. This line indicates a minimum strength with the general sample size. This is consistent with the theory of dislocation source operation. The datasets above this line can be explained by other strengthening mechanisms such as work hardening. Only few data falls below this line, we suggest the reason is the error in the grain size determination. Rhines [60] demonstrated about 10 methods to determine the grain size and most authors did not introduce their methods for the grain size determination. Hence, the random error of the grain size values can come from authors' subjective choices. We proposed that the

low values of the exponent obtained from fitting to the Eq.2.3, are also attribute to the error in the grain size determination. According to the classic Ag and Cu data, Dunstan designed the new dummy data with the errors in grain size measurement [45]. The errors are expected to be proportional to grain size (lognormal distribution). The reason for using lognormal distribution is because large and small grain size are usually measured from micrographs showing a similar number of grains. The values of grain size and error can be obtained before the scale bar is read. Then the Eq.2.3 were used to the fitting to the new dummy datasets, the exponents obtained are dramatically smaller than the values got from the fitting to the relevant original datasets. The dummy data fitting results are corresponding well with some simulation works [87-89]. In modelling works, there is no error bar on the grain size, their conclusions suggest that the exponents are greater than 0.5.

It is true that all the datasets agree well with Hall-Petch equation, but there is an important feature of the HP equation, that both $\sigma_0$ and $k_{HP}$ were treated as free fitting parameters. This is reasonable for $\sigma_0$, for the bulk strengths of metals can generally be varied widely by metallurgical processing. It is less reasonable for $k_{HP}$, this factor might have been given a fixed value which was explained by theory. However, the factor $k_{HP}$ varies largely even for a particular metal data. The modified Ashby theory also predict a minimum strength but depending on strain. Our other statistical results (submitted to Acta Mat.) shown that the factor of $k_{HP}$ is independent on strain, which outside the scope of this thesis. In contrast, many of the datasets agree very well with Eq.2.2 for the fixed value of $k = 0.72$, e.g. Fig. 2.3-2.7.

## 2.3 Bayesian analysis of support for hypotheses

Since the comparison of the fitting of the Eq.2.2 and Eq.2.8 by eye are not rigorous, an analysis of the statistical method should be introduced to explain eventually which equation is better. Hence, a fully Bayesian analysis is given in this section. Bayes' theorem can be expressed that the posterior probability for the observed data is the result based on the prior probability and likelihood function [90], the formula is:

$$P\left(H\left|N\ \ E\right.\right)=\frac{P\left(N\ \ E\left|H\right.\right)\times P\left(H\right)}{P\left(N\ \ E\right)} \tag{2.10}$$

where $H$ stands for any hypothesis whose probability may be affected by the data, $N\,E$ stand for the new evidence, $P\,(H|N\,E)$ means the probability of a hypothesis given the new observed evidence, i.e. the new probability after new data is tested, and $P\,(H)$ corresponds to prior probability, is the prior probability of $H$ before the new data is observed. $P\,(N\,E|H)$ is the likelihood which indicates that the probability of observing the new data given $H$.

We use the $\overline{H}$ represent the hypothesis is false. From the Eq.2.10, it is not difficult to derive the equation below:

$$\frac{P\left(H\left|N\ \ E\right.\right)}{P\left(\overline{H}\left|N\ \ E\right.\right)}=\frac{P\left(H\right)}{P\left(\overline{H}\right)}\times\frac{P\left(N\ \ E\left|H\right.\right)}{P\left(N\ \ E\left|\overline{H}\right.\right)} \tag{2.11}$$

The new probability of the hypothesis under the new data being true equal the prior probability of the previous data, multiply by the ratio of the probability of the new data under the hypothesis $H$ and its probability if $H$ is false ($\overline{H}$).

In our analysis, we take $H$ to be the hypothesis that Eq.2.2 is correct, then $\overline{H}$ to be the hypothesis that Eq.2.8 (modified Ashby theory) is correct. Both the theory of Eq.2.2 and Eq.2.8 proposed a minimum strength due to the size effect, i.e. the line of Eq.2.2 with $k$~1 and $\varepsilon_0$=0 and Eq.2.8 at yield strain. We consider the grain size at sub-millimeter region, the minimum strength of Eq.2.2 divides the $log\sigma_0$–$logd$ space into two equal parts. The theory determined all of datasets should be concentrated into the half of the space above the line, the probability of the dataset falls far below the line is zero. Hence, in our hypothesis of Eq.2.2 is correct, we have a probability density of 1 for datasets above the $d^{-1}$ line and 0 for data dramatically below the $d^{-1}$ line. On the other hand, modified Ashby theory also predict a minimum strength, the plot of yield minimum strength is lower than Eq.2.2. This leaves an empty gap with no data in it, as shown in Fig.2.10. The area of the two triangles A and B can be estimated to be about 4.5 and 11.5. Then the probabilities of dataset falling in these areas are about 0.3

and 0.7, respectively. If the hypothesis of Eq.2.8 is valid, the relative probability density above the $d^{-1}$ line is about equal to 0.7.

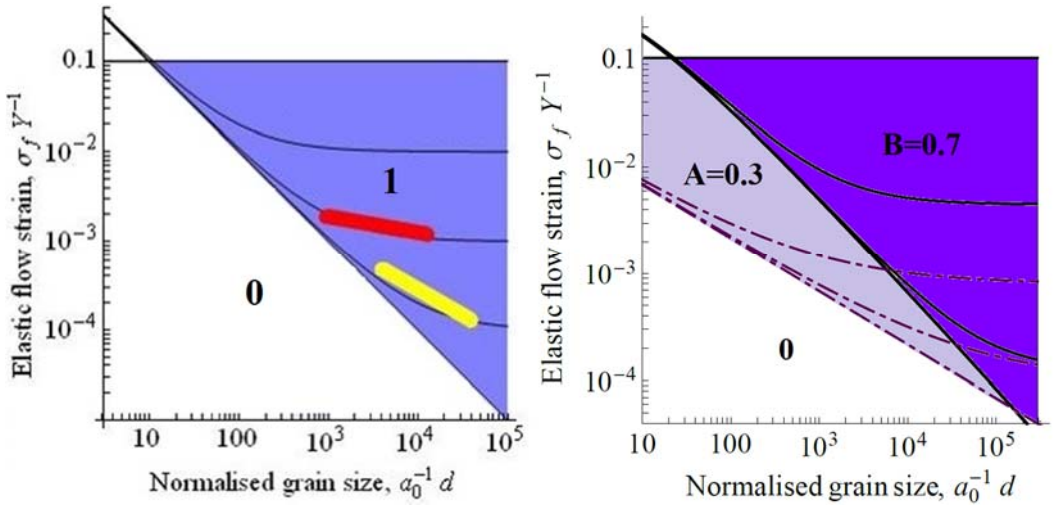


**(a)** **(b)**

**Fig.2.10 The probability distribution of Eq.2.2 and Eq.2.8 in the log$\sigma_0$–log$d$ space. In (a), the Eq.2.2 have a probability density of 1 for datasets above the $d^{-1}$ line (black heavy line) and 0 for data dramatically below the $d^{-1}$ line. In (b), for the Eq.2.8, the relative probability density above the $d^{-1}$ line is 0.7 due to 0.3 of the gap between modified Ashby theory (purple chain-dotted line) and CTT theory (black heavy line).**

More formally, using Bates Theorem, the Eq.2.11 is applied repetitively to get the probability of our hypothesis. We consider the second term on the RHS, the ratio of the probability of the new data under the hypothesis $H$ and its probability if $H$ is false. It means that for every single dataset falls above the $d^{-1}$ line, the ratio gives a value 1.43 to the second term on the RHS. If each dataset $i$ falls above the $d^{-1}$ line, we can get the new probability of $P_i$=1.43$P_{i-1}$, and for $n$ datasets, $P_n$=1.43$^n P_o$. As observed in Fig2.8, there are in total 30 yield strain datasets from the classic literature, all of 30 datasets are fall above the $d^{-1}$ line with only a few data points not significantly fall below the $d^{-1}$ line. Hence, for the hypothesis of Eq.2.2 is valid, these 30 datasets giving the probability of $1.43^{30}P_0$ ($4.6\times10^4$) to one. We can conclude that for any

reasonable value of prior probability $P_o$, the final probability $P_{30}$ is a tremendous value to accept the Eq2.2 as preferable to modified Ashby theory.

It is hard to say there is no data point fall below the $d^{-1}$ line. For example, one data point of Ni (1), some data points of the ultra-fine grain size samples Al (4), Al (5) and Al (6), are fall below the line. But they are very close to the line. Compare to the large amount of the datasets, these data points are quite little. There are several reasons can explain these data points. In fact, the grain size determination methods, the grain size distribution and the experimental equipment error can all contribute to these data points fall below the line. For the ultra-fine grain size samples, may be accounted by grain boundary sliding, migration and diffusion which have been considered in the inverse Hall-Petch effect [91-93].

## 2.4 One-parameter Hall-Petch theories

As described in the literature review (Section 1.5), in the past a few decades, generally, four typical models were proposed to explain the Hall-Petch relationship. The schematic of the four classic models are shown together in Fig.2.11. It is clear that there are two constraining parameters $\sigma_0$ and $k_{HP}$ in the Hall-Petch relationship, the value of parameter $\sigma_0$ are various, the reason is that the bulk strengths of metals can generally be varied widely by metallurgical processing. For the predictions for the values of parameter $k_{HP}$, each model implied a different value. The $\sigma_0$ is unrelated to the grain size, while the $k_{HP}$ is account for the grain size dependent. Hence, it is necessary to compare their predictions of $k_{HP}$ with the real experimental datasets, to test whether they are in fact supported by the experimental data. The details of the formula derivation of the four models have been described in the Section 1.5. In this section, the normalized form of the equations corresponding to the normalized data are illustrated below.

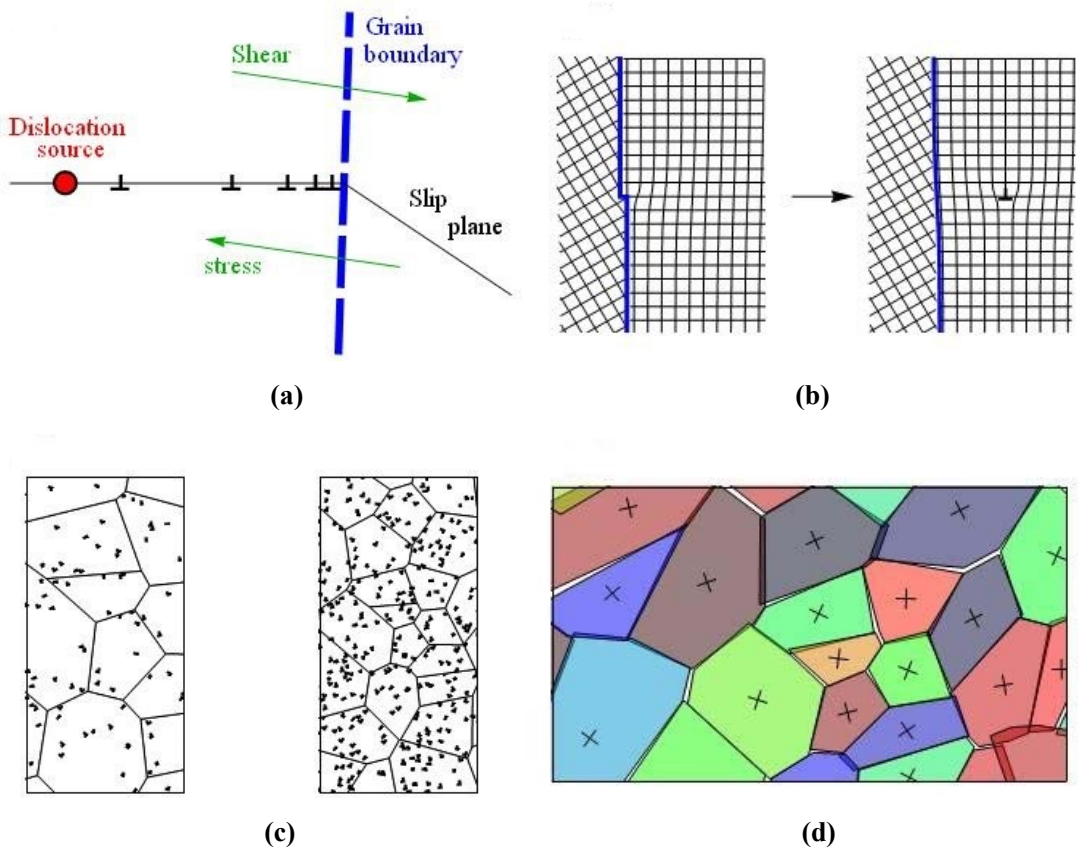


**Fig.2.11. The schematic of the four classic models: (a) Dislocation pile-up model, (b) Grain boundary source model, (c) The slip distance model, (d) The GNDs and elastic anisotropy model.**

## 2.4.1 Dislocation pile-up model

The most frequently cited explanation of the Hall-Petch effects is the dislocation pile-up model. This model gives the equation:

$$\tau = \tau_0 + \sqrt{\frac{Gb\tau_c}{\pi d}} \tag{2.12}$$

where $G$ is shear modulus, $b$ is the burger's vector, $\tau_c$ is the critical shear stress at the grain boundary, when the stress over this value, slip will cross the grain boundary. Dislocations will propagate to the next grain. The maximum reasonable value of $\tau_c$ is less than $G/10$. In the data normalization, the grain size and stress are normalized by the relevant material lattice constant $a_0$ and Young's modulus $Y$, respectively. Combine

the relationship of $Y = 2G(1+\nu) \approx 2G$, we consider the approximation $\tau/G \sim 2\sigma/Y$, $b \sim a_0$. Then the Eq.2.7 becomes

$$\varepsilon - \varepsilon_0 = \frac{1}{2}\sqrt{\frac{\tau_c}{\pi G}}\frac{1}{\sqrt{a_0^{-1}d}} \leq \frac{\sim 0.09}{\sqrt{a_0^{-1}d}} \tag{2.13}$$

where $\varepsilon$ is the elastic flow strain.

## 2.4.2 Grain boundary source model

Since the directly experimental observations on dislocation pile-up model are not always found. Li [49] first proposed that sources of dislocation is grain boundary. According to Taylor's law for forest dislocation hardening, the grain boundary source model:

$$\tau = \tau_0 + \alpha Gb\sqrt{\frac{8m}{\pi d}} \tag{2.14}$$

where $\alpha$ is a constant depends on dislocation arrangement, the value of $\alpha$ is 0.4. $G$ is shear modulus, $b$ is the burger's vector, $m$ is a constant represents the ledge density, typically, $mb$ will be in the range 0.02~0.2 [94, 95]. With the same approximation $\tau/G \sim 2\sigma/Y$, $b \sim a_0$, the Eq.2.9 becomes

$$\varepsilon - \varepsilon_0 = \frac{\alpha}{2}\sqrt{\frac{8mb}{\pi}}\frac{1}{\sqrt{a_0^{-1}d}} \approx \frac{0.05 \sim 0.15}{\sqrt{a_0^{-1}d}} \tag{2.15}$$

## 2.4.3 The slip distance model

In 1967, Conrad and co-workers developed the slip distance model. They suggested that the value of $k_{HP}$ depends on the plastic strain (with no Hall-Petch effect at the yield point), for a given strain, the dislocation density was higher in small grain samples than in the larger grain specimens. Combining with the work hardening equation, they give the slip distance model by:

$$\tau = \tau_0 + \alpha G b\sqrt{\rho} = \tau_0 + \alpha G\sqrt{\frac{b\varepsilon_{pl}}{\alpha_1 \lambda d}} \tag{2.16}$$

where $\alpha$ is a Taylor constant depends on dislocation arrangement, the value of $\alpha$ is 0.4. $G$ is shear modulus, $b$ is the burger's vector. $\alpha_1\lambda$ are both constant but less the order of unity. The equation is converted by our approximation $\tau/G \sim 2\sigma/Y$, $b \sim a_0$, we can get

$$\varepsilon - \varepsilon_0 = \frac{\alpha}{2}\sqrt{\frac{\varepsilon_{pl}}{\lambda\alpha_1}}\frac{1}{\sqrt{a_0^{-1}d}} \tag{2.17}$$

In Eq.2.12, the factor of $\alpha/2\sqrt{\lambda\alpha_1}$ is a constant depends on the order of unity. For the high plastic strains about 0.2, that the value of $k_{HP}$ may be around 0.5, while for the low plastic strains near the yield point e.g. $\varepsilon_{pl}$ is near 0.002, the value of the slope will be below 0.05.

### 2.4.4 The GNDs and elastic anisotropy model

The GNDs was introduced by Ashby [2] to explain the extra strength of the materials. Similarly, Kelly [96], Hirth [55] and Meyers [56] proposed the elastic anisotropy model. They suggested that the anisotropic grains are distributed in a homogenous stress field. With the grain sizes decrease, the strain gradients and the densities of GNDs will be proportionately larger. This model predicts that after suitable normalization, $k_{HP}$ will be proportional to the elastic anisotropy. The factor of proportionality is not clear under the model. In the cubic material, a formula to calculate the anisotropy factor is $C = |c_{11} - c_{12} - 2c_{44}|$.

### 2.4.5 Results and discussion

The first three models (Section 2.4.1-2.4.3) make the clear predictions of the value of $k_{HP}$, respectively. Thus, it is convenient to compare these three models together with the normalized datasets. As shown in the Fig.2.12 (*a*). According to these models, the depth of shading indicates the probability of data will fall in the various regions, white

corresponds to a probability close to zero.

The heavy black line indicates the predictions of the pile-up model (Eq.2.8), the triangle below the solid black line is the expected region of the pile-up model. It is found that many of the datasets falls above the heavy black line where the maximum $k_{HP}$ value from the pile-up model. Obviously, the pile-up model cannot explain a great part of the experimental datasets. Some datasets have a much greater slope means that the predictions of the pile-up are too weak to explain the effect of the grain size on the dislocation mechanism. This conclusion is confirmed by discrete dislocation dynamics simulations of wires in torsion.

The predictions of the grain boundary source model (Eq.2.10) are illustrated by the region between the two blue dashed lines. It is also found that many datasets located outside of the region. This model is again inconsistent with much of the data. The narrow region cannot explain the wide scattered datasets.

The red chain-dotted lines stand for the predictions of the slip distance model (Eq.2.12). Evidently, this theory is failed to explain the Hall-Petch effect near the yield point. For the high plastic strains datasets, this model is good enough as an explanation. It is worth noting that we consider several high quality datasets with various strains from yield region to the high plastic strains, e.g. Cu(1), Cu(2), Al(1) and Al(2), there is a very weak evidence that the value of $k_{HP}$ depends on the plastic strain.

For the GNDs and elastic anisotropy model (Section 2.4.4), the values of $k_{HP}$ for the cubic metals were plotted against the related normalized anisotropy $C/Y$, as shown in Fig2.12. (b). Large data points indicate that only one data is available for a metal. Small data points represent the different values of datasets for the same metal. The red filled circles indicate the yield data sets. For one particular metal, there is a significant scatter of the value of $k_{HP}$. The solid black line is a least-squares fitting of $y=ax+b$ to the averaged data, the slope of the fitting is nearly horizontal suggests that there is no evidence support the parameter $k_{HP}$ is proportional to the elastic anisotropy.

From the results of this section, we can conclude that none of these classic models could explain the experimental data well. All of them are failed to predict the values of the

parameter $k_{HP}$. From the view of the Bayesian analysis, the datasets distribution show that the probability of these models being true is close to zero. In contrast, almost all of datasets support the Eq.2.2.

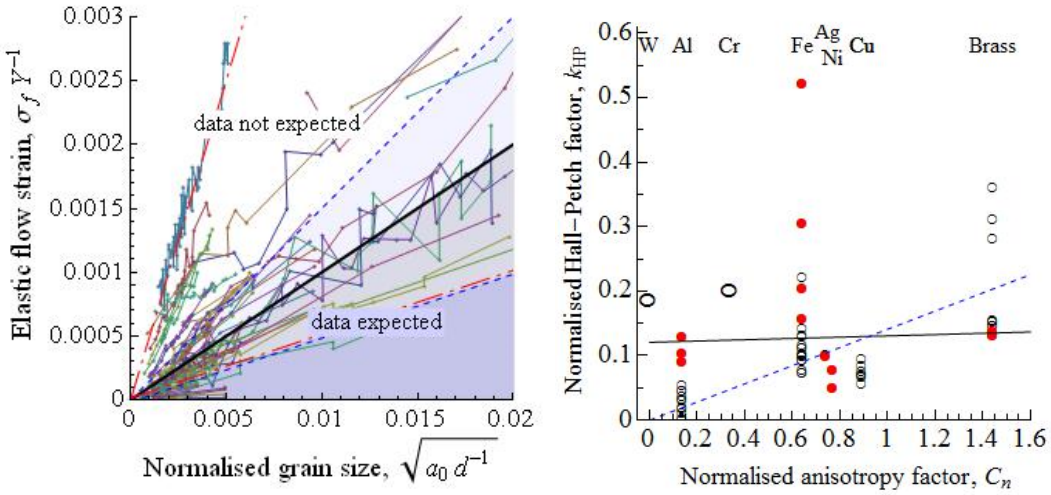


**(a)** **(b)**

**Fig.2.12. (a) The predictions of the pile-up model (Eq.2.8) (heavy black line), the grain-boundary ledge model (Eq.2.10) (dashed blue lines indicating the range of the upper limit of the predictions) and the slip-distance model, Eq.2.12 (chain-dotted red lines) are compared with the data. The depth of shading indicates schematically the probability according to these models that data will fall in the various regions; white corresponds to a probability close to zero. In (b), the Hall-Petch slopes are plotted against the normalised anisotropy factor. The large data points indicate that only one data set is available for a metal; the small data points represent many results for the same metal. The red filled circles indicate the yield datasets. The solid black line is a least-squares fit of $y = ax + b$ to the averaged data and the dashed blue line a fit of $y = ax$ as described in Section 2.4.4.**

## 2.5 Hypothesis on Eq.2.2 is correct

In section 2.3, the Bayesian analysis on the data distribution conclude the Eq.2.2 is correct. Then in section 2.4, it is concluded that none of the classic models on Hall-Petch relationship could explain the experimental data well. Thus, in this section, it is

quite meaningful to propose a method to test the Eq.2.2, from the view of one dataset. If we consider the Eq.2.2 is correct, i.e. for each dataset, the data points are actually consistent with the Eq.2.2, then in the $d^{-1/2}$ plot (the traditional Hall-Petch plot), they will follow a parabola instead of the straight line. In other words, if we plot the Eq.2.2 against the inverse square root abscissa, it will be a parabola. The schematic is shown in Fig 2.13 (a). The black heavy parabola represents the Eq.2.2. When the data point distribution obey this parabola, we can divide the whole data points into three regions: large (L), mid-point (M) and small (S) grains region, which are represented by blue, green and red, respectively. It is clear that for these three regions, the slopes of the fitting with straight lines are different, as shown in the figure, the slope of the mid-point region fitting (green line) should be the value of the parameter $k_{HP}$, the gradient of the large grains fitting is lower (blue line), the higher value can be obtained for small grains fitting (red line). Fig 2.13 (b) is an example from the data of Emery's gold films tension experiment. The blue dashed line is the best fit parabola of Eq2.2. The black solid straight line is the Hall-Petch fitting of Eq.2.1. The red solid line is the fitting to the large grain size and small grain size datasets, separately, according to the equation below:

$$\begin{aligned} y &= y_0 + k_{HP}^{low}(x-\bar{x}) \quad x < \bar{x} \\ y &= y_0 + k_{HP}^{high}(x-\bar{x}) \quad x > \bar{x} \end{aligned} \tag{2.18}$$

where the $\bar{x}$ is the mild-point of the whole dataset.

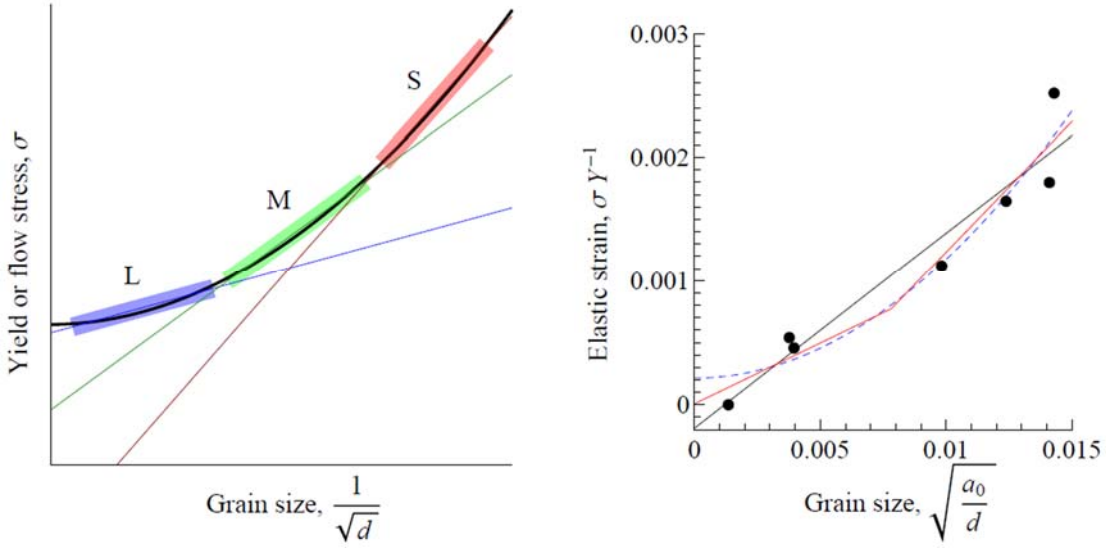


**(a)** **(b)**

**Fig.2.13. (a) The schematic of Eq.2.2 plots against the inverse square root abscissa. The black heavy parabola represents the Eq.2.2. The three regions datasets in different ranges of grain size are shown by different colours: large (L), mid-point (M) and small (S) grains region, which are represented by blue, green and red, respectively. Fitting to the large-grain-size dataset (L, blue) will give the blue straight line with a small slope $k_{HP}$, while fitting to the green (M) and red (S) datasets with medium and small grain sizes will give the green and red straight lines with larger slopes (larger values of $k_{HP}$). (b) This is an example from the data of Emery's gold films tension experiment. The blue dashed line is the best fit parabola of Eq.2.2. The black solid straight line is the Hall-Petch fitting of Eq.2.1. The red solid line is fitting with the upper and lower halves of the dataset.**

Based on the schematic of Fig.2.13 (a), we can conclude that the experimental values of $k_{HP}$ shows a dependence on grain size $d$ when the data points distribution actually consistent with Eq.2.2. Thus, the Hall-Petch gradient $k_{HP}$ of the 61 datasets are plotted against the normalized average grain size, as shown in Fig.2.14. For the grain size normalization, the mid-points of each dataset on the classic Hall-Petch plots were taken, i.e. $d_{ISR}^{mean} = ½(d_{ISR}^{\max} + d_{ISR}^{\min})$. The reason for choosing the mid-points of each dataset is because the slope of a straight line fitted to data that follow the parabola would be

approximately the gradient of the parabola at the mid-point of the data range.

Indeed, the data points are scattered largely. However, the fit of the data are shown a trend that the smaller grain size are related to a higher value of the $k_{HP}$. For a few large grain sizes data, the value of the gradient are quite low.

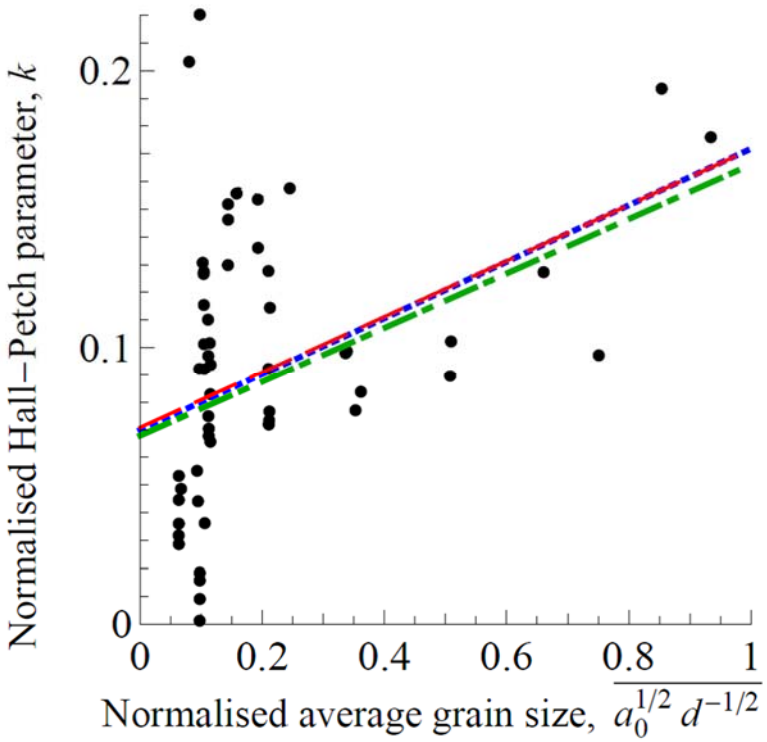


**Fig.2.14. The normalised HP factors are plotted against the normalised average grain size.**

We verify the unreasonable scattered high values of the $k_{HP}$ of the large grain size data. It is found that most of them are from the alloy like steel and brass. The high values could be accounted by complicated microstructure and impurity. Thus, if we consider only pure metals, we will get a less scattered plot, as shown in Fig.2.15. The values from 27 pure metals datasets are plotted against inverse square root of the normalized average grain size. The dashed line represented that the values of the $k_{HP}$ have no dependence with the grain size. The heavy black line indicates a trend that the smaller grain size datasets have a higher value of the $k_{HP}$.

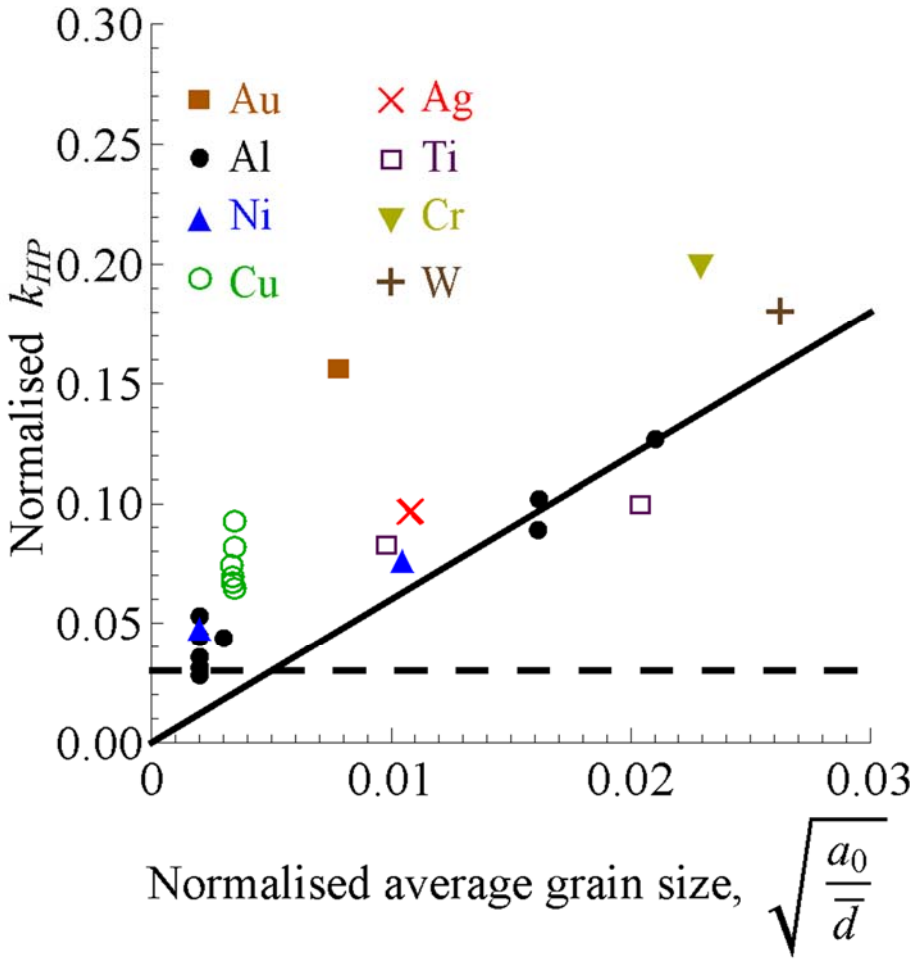


**Fig.2.15. Normalised values of $k_{HP}$ for the data from the pure metal datasets are plotted against the normalised inverse square root of grain size. The heavy black line indicates that the smaller grain size datasets have a higher value of the $k_{HP}$.**

## 2.6 Conclusions

It is clear that the experimental evidence can support the 60-year-old Hall-Petch equation (Eq.2.1), the dislocation curvature equation (Eq.2.2) and modified Ashby equation (Eq.2.4). However, the fully Bayesian analysis result, giving the probability for the hypothesis of the Eq.2.2 is preferable compared with the two parameters Eq.2.1. From the fitting to the datasets with Eq.2.1, we get a wide range values for the Hall-Petch constant $k_{HP}$. For even one material, the large scattered $k_{HP}$ cannot explain anything valuable character of the relative material. Additionally, the four classic

models described in Section 2.4 are all failed to predict the values of $k_{HP}$. On the other hand, both Eq.2.2 with the fixed parameter $k$ = 0.72 and $\varepsilon_0$ = 0 and Eq.2.4 at the yield strain with $\varepsilon_0$ = 0 (Eq.2.8) can predict the minimum strength expected for a given grain size, i.e. the $k_{HP}$ is a fixed constant. The large grain size data could corresponding well with both Eq.2.2 and Eq.2.4 (Eq.2.8), the small grain size data are more prefer to Eq.2.2. However, when the maximum physical reasonable values of Taylor factor and forest hardening constant are adopted, Eq.2.4 (Eq.2.8) can also compatible with the small grain size data.

It has been claimed that the Hall-Petch relationship is a valid empirical relation and it is useful for the prediction in the material community. It does not matter whether it is theoretically correct. Actually, for one material, the experimental observations obtain a large scattered parameter $k_{HP}$. Thus, the Hall-Petch equation is failed to predict the parameter for one kind of metal material. It is hard to say that Hall-Petch equation is qualified as an empirical formula. We consider the precise description of Hall-Petch relation is that the strength decreases monotonically with the increase of the grain size. We can obtain a disputable conclusion from this chapter: The Hall-Petch effect is a manifestation of the general size effect, instead of a particular experimental behavior with its own unique inverse square root exponent and individual value of $k_{HP}$. Accordingly, there is no necessary to find its own explanation and theoretical model of the $k_{HP}$. We propose that a fundamental size dependence in all experimental observation is dislocation curvature equation based on the critical thickness theory: the size is inversely proportional to dislocation curvature and therefore to stress. In the case of grain size effect has the same mechanism as other general size effects, it will be considered that combined these effects together. For example, Dunstan & Ehrler proposed an effective length which coupling of grain size and structural size [97].

# 3. Size effects in the bending of micro-foils

Because there is a strain gradient from zero strain on the neutral plane to a maximum strain at the foil surface, the micro-foil bending experiment is one of the best method for testing SGP theory.

In micro-foil bending tests, measurements of bending moments are difficult because the values are small. It is also difficult to control the strain level precisely. To overcome both of these difficulties, in 1998, Stolken and Evans [8] designed a brilliant micro-foil bending experiment method. In this section, their experimental design is reviewed in detail.

## 3.1 Stolken and Evans' experiment

The most convenient design feature of their method is that the data are obtained only from measurement of curvature, using a non-contact optical microscope.

### 3.1.1 Experimental design

The schematic of their micro-bending method is reproduced in Fig.3.1. Firstly, the foil sample is clamped between two cylindrical mandrels. The lower mandrel is used for supporting the foil loading i.e. during the loading process, the foil will be bent on the cylindrical surface of it. The upper mandrel is necessary for clamping the foil, it can secure the foil to make sure the symmetric loading, as well as preventing the distortion upon the unloading process. On each side of the sample, there is an aluminium die for loading the sample (Fig.3.1 a). Secondly, the profiled dies move downward, and load the foil on the lower cylinder (Fig.3.1 b). Finally, unload process, the foil is elastically recovered (Fig.3.1 c). During the unload process, to minimize the friction with the foil, it is necessary to have highly polished contact surfaces. Otherwise, the friction will cause the distortion when the die is removed.

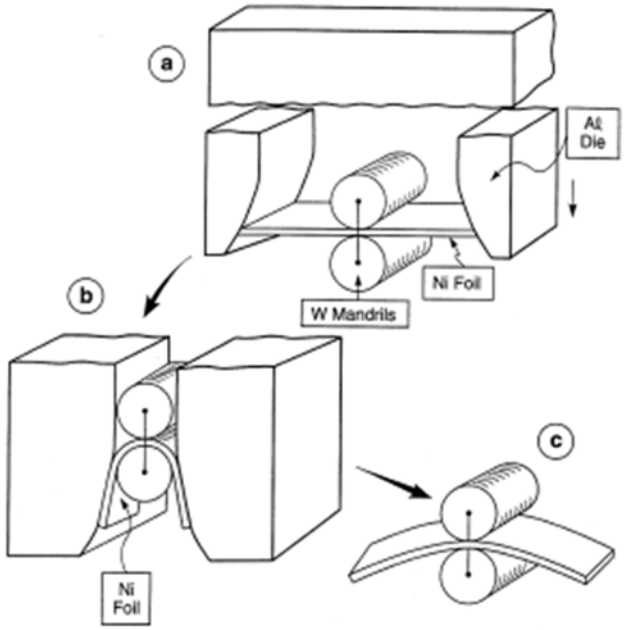


**Fig.3.1. Schematic of the Stolken and Evans' micro-foil bending equipment. (a) mounted the foil, (b) load process, (c) unload (elastic recovery). (Reproduced from Stolken and Evans [8])**

The schematic of the calculation of stress-strain behaviour from measured bend radii is shown in Fig.3.2. During the load process, the flat foil sample is bent plastically around the cylinder below, as shown in Fig.3.2 (b). The radius of the cylinder is $R_0$. Then the load is removed, the foil is unload elastically. The sample recovers elastically to a large radius of curvature $R_f$, as shown in Fig.3.2 (c). Because the foil is fully contacted with the cylinder, the surface strain of the foil in the loaded state is simply related to the radius of cylinder, giving the surface strain by

$$\varepsilon_b = \frac{h}{2R_0} \tag{3.1}$$

where $h$ is the thickness of the foil and $R_0$ is the radius of the cylinder. The moment of the foil is related to two radii of curvature. When the foil is in the loaded state, the total strain contains both elastic and plastic component; when it is unloaded, for the reason of elastically recovery, the strain only contains plastic component. Hence, the increase in the radius of curvature gives a determination of the bending moment at the load radius $R_0$. The bending moment normalized by $bh^2$ is

$$M_n = \frac{M}{bh^2} = \frac{Eh}{12}\left(\frac{1}{R_0} - \frac{1}{R_f}\right) \tag{3.2}$$

where $M_n$ is the normalized bending moment, $b$ is the width of the foil, $h$ is the thickness of the foil, $E$ is the Young's modulus of the material and $R_f$ is the radius of curvature for the unloaded foil. By selecting cylinders with a suitable range of radii, a range of surface strains and related moments will be obtained. Then the stress-strain figure can be plotted.

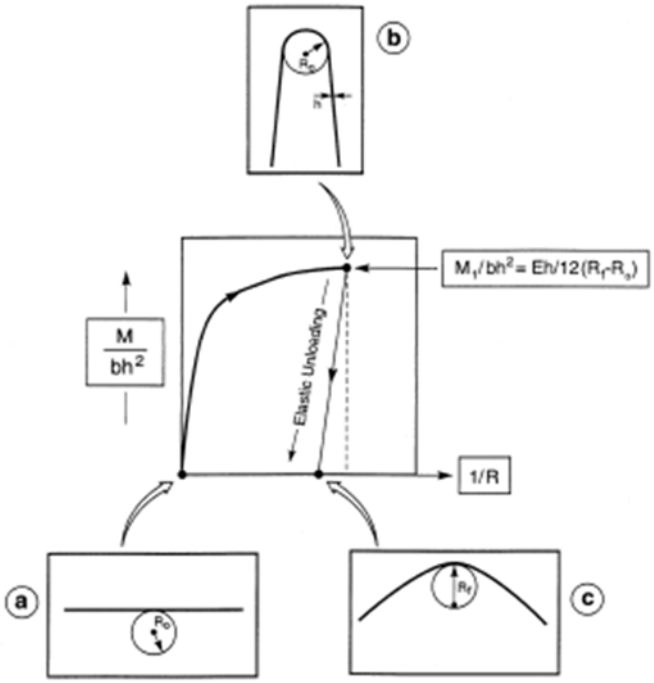


**Fig.3.2. Schematic of the calculation of stress-strain behaviour from measured bend radii. (Reproduced from Stolken and Evans [8])**

## 3.1.2 Results and Weakness

Stolken and Evans observed a strong size effect in the foil bending tests. As shown in Fig.3.3, the normalized bending moment were plotted against the surface strain. The strength of the foils increased greatly when the thickness of the foil decreased below 25μm. Their experiment is a very good design but has its own weakness: firstly, the grain size effect is not studied in their results; secondly, they can only obtain data at high plastic strain; thirdly, the plots have large error bars. Hence, more work is needed

to be done to improve the data, specifically, the obtaining of more precise data over a wider range of strain.

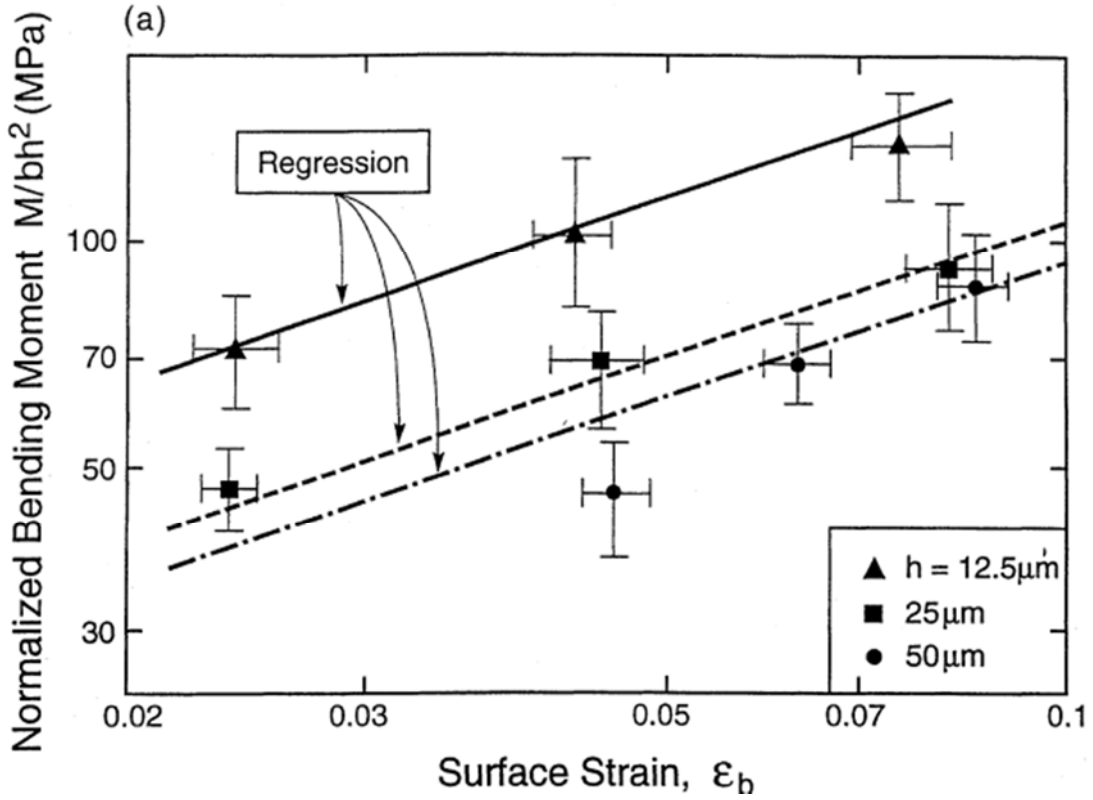


**Fig.3.3 The normalized bending moment were plotted against the surface strain for all three foil thickness ranging from 12.5 to 50μm . (Reproduced from Stolken and Evans [8])**

## 3.2 M.Y. P'ng Four-Point Bending Test

Previously, in our group, M.Y.P'ng and David Dunstan [98] (2005) reported one yield strength data set of nickel foils. They adopted the classic measurement of curvature of the foils test method. As described in the upper paragraph, in this method, the most important issue is the quality of the data. The metals such as Cu and Ni are so soft. Hence, the stress-strain data can be obtained only when large plastic deformation. Obtaining data around the yield point is not easy. That is why Stolken and Evans' data was focus on the high plastic strain area. To obtain the data around yield point which requires the measurement of large radii of curvature, the modification to the bend test

have to be made. Hence, they designed a 4-Point bending test and constructed the new apparatus.

### 3.2.1 Rig and method introduction

Schematic of the micro-foil 4-Point bending apparatus is shown in Fig.3.4. 4-Point bending means there are four roller: two Middle rollers and two Outer rollers. These four rollers are distributed symmetric in the rig. A shim made by spring steel is mounted between the Middle rollers and Outer rollers. The screw on the left side is used to drive the wedge move towards the right direction or return back. The two Middle rollers will be raised up when the wedge moves to the right side. Initially, the shim is flat (radius is infinity). The radius of the shim is reduced by raising the two middle rollers. The red line in the Fig.3.4 is thin metal foil. The foil is restricted on the shim by two weighted bars on both sides of the foil. Hence, the foil is bent into the curvature of the shim. The top of the foil is exposed in the rig. Hence, they can use a non-contact optical profilometer to measure the load and unload radius (curvature).

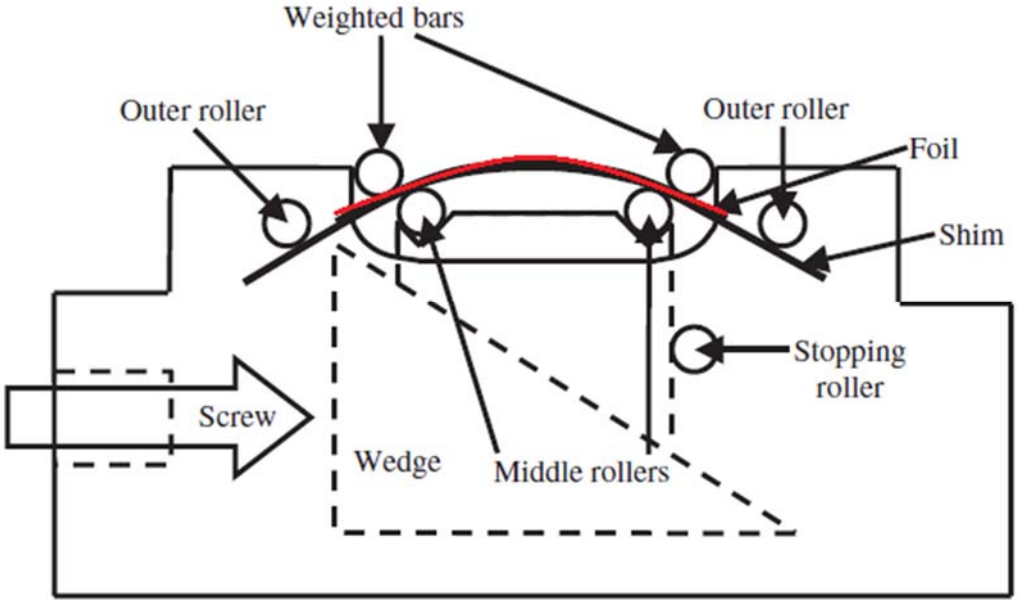


**Fig.3.4 Schematic of the 4-Point micro-foil bend rig reproduced from P.Moreau, M.Y.P'ng [98]. The red line is thin metal foil, which is restricted on the shim by two weighted bars on both side.**

### 3.2.2 Weakness

This rig can obtain the data around yield point of the soft metal by introducing the spring steel shim, because the spring steel shim makes it possible to control the small strain level (measure the large radius of the curvature) precisely. However, the introduced spring steel shim also constrains the flexure (deformation) upper limit, because it is too hard to deform easily. The minimum radius of the shim in this rig can be obtained is 30mm. It means that the data points obtained by this rig can only cover the elastic and yield point area.

These data sets are good enough to study mechanical properties around the yield point of the foil. However, if we would like to get accurate discrete data from the elastic region through the yield point and to high plastic strain area, we have to use two different apparatus work on one particular thin metal foil sample, i.e. the 4-Point bending rig is used to produce the elastic region and yield point data, then the load-unload method on a range of mandrels of smaller radii to obtain the high plastic strain data. Since it is quite difficult to mount the thin soft metal foil into the rig, particularly, it is very complex to mount the already bent foil with the different mandrels, the accuracy of the whole data sets are hard to guarantee.

## 3.3 Summary

Stolken and Evans proposed a brilliant testing method that the data are obtained only from measurement of curvature, using a non-contact optical microscope. However, the most important weakness is the big error bar in the results. This uncertainty is from the experimental operation since the soft thin metal foils are so fragile that repeated handling deform the foil itself. Hence, the great challenge of the experimental design is obtaining the precise data with minimum error bars. If we would like to get the excellent data sets for the whole range, we should avoid to mount the thin foil many times. The best method is to design a new device in which the thin foil is mounted only once then

the whole range of different radii of load formers could be substituted. We call it load-unload formers bending test.

# 4. New testing method for micro-foil bending test

## 4.1 Introduction

I will introduce the new load-unload formers bending test experimental design in this chapter. At the beginning, I will introduce the idea of the rig design and fabrication of the formers in section 4.2. Secondly, the experimental design of this new methods include the sample preparation method and data plot will be illustrated in section 4.3. Finally, the experimental procedure and initial test results will be shown in section 4.4 and 4.5.

## 4.2 Mechanical testing equipment

### 4.2.1 The rig

A schematic of the load-unload former bending rig is shown in Fig.4.1. The different components of the rig are shown in Fig.4.1 (a). The thin metal foil is fixed by the cover plate on the top of the rig. There are two screws that can fix the cover plate and foil. The middle part of the cover plate is removed, so the thin foil sample can be exposed. Then we can load the foil and measure the surface profile conveniently. The top-view of the cover plate is shown in Fig.4.2 (a).The wedge has an angle of 12º, a trench with the same angle 12º is designed in the rig (the purple dash line). Hence, the wedge can be moved in the rig freely. Each former has a certain radius. The former is put on the wedge, and moves forward with the wedge, as shown in Fig.4.1 (b). When the former reach to the stopping plate, with the push forward of the wedge, the former will move upward. Finally, the wedge will be stopped by the second plate, as shown in Fig.4.1 (c). The distance between the two stopping plate is calculated precisely to make sure the former and thin foil contact compactly. When the experiment is in progress, to put the former and thin foil in full contact, a rubber is used to load the foil, then unload. The

shape of the rubber is shown in Fig.4.2 (b).

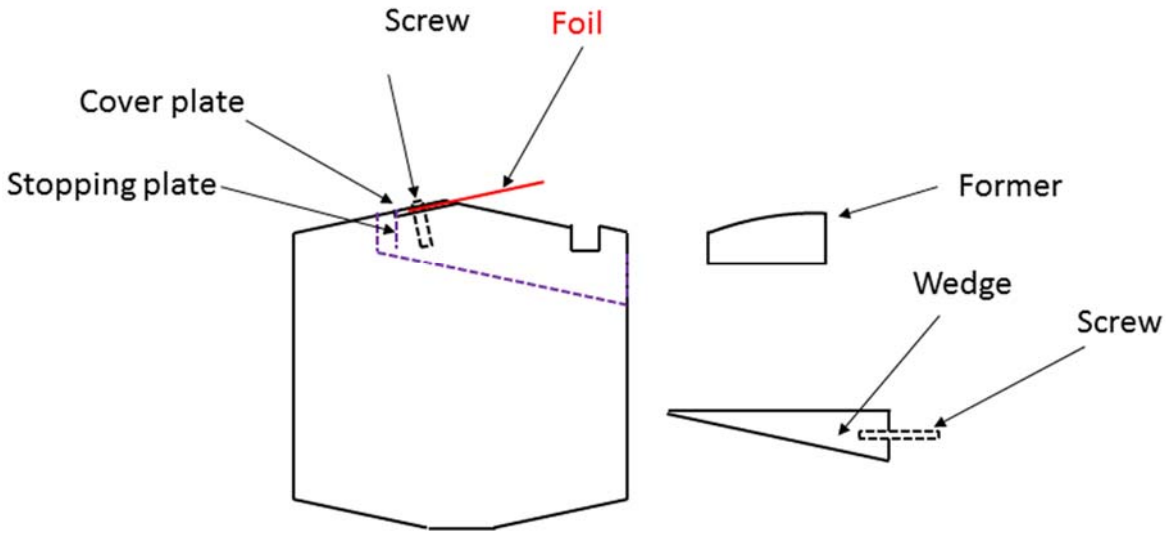


**(a)**

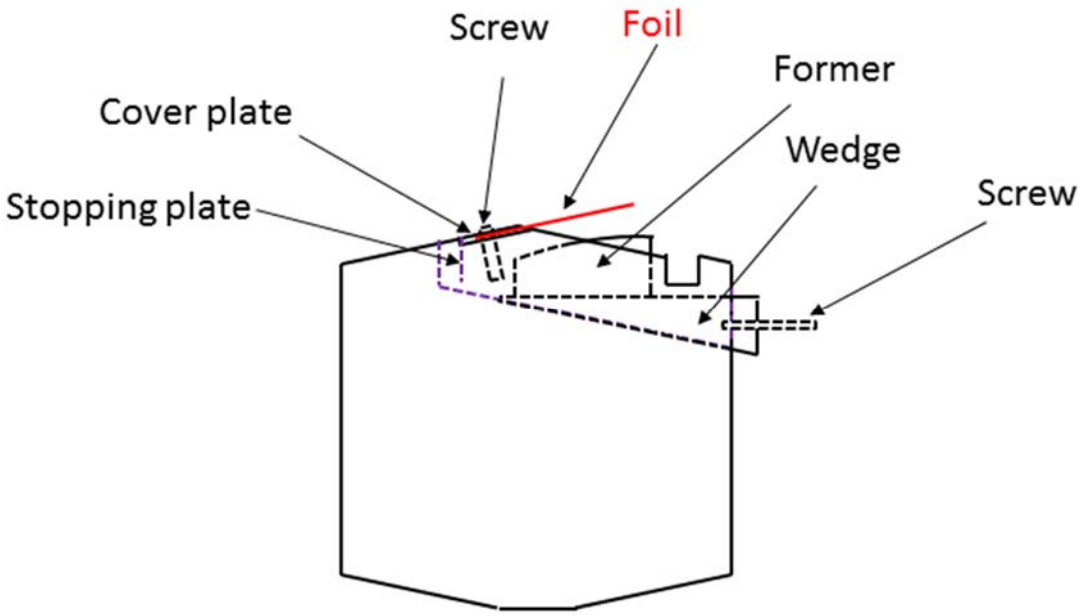


**(b)**

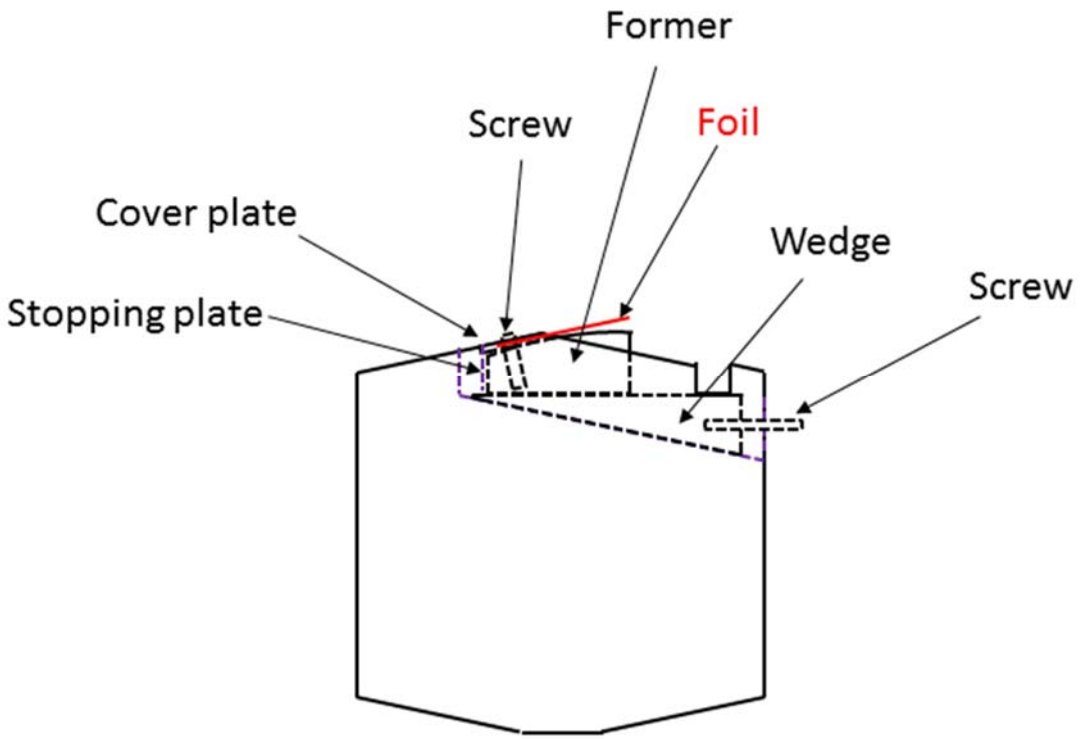


**(c)**

**Fig.4.1 Schematic of the load-unload formers bend rig. (a) Introduction of the different components of the rig. (b) (c) show the details of how to control the wedge and former.**

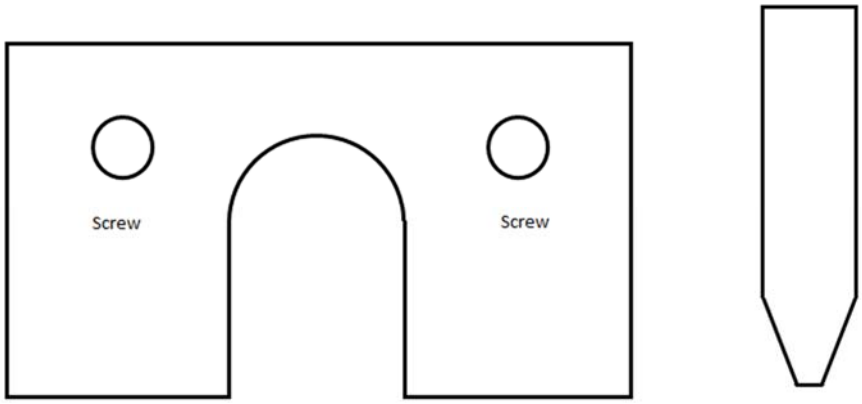


**(a)** **(b)**

**Fig.4.2 (a) The top-view of the cover plate is shown. The middle part is removed to expose the foil. (b) The shape of the load rubber.**

The bottom of the rig has two kind of faces (face1 and face 2), the angle of intersection

between these two faces is also 12°. The surface profile of foil can be only measured in the X-Y plane and has a height limitation in Z-axis, because the non-contact profilometer can only measure small vertical displacement over long distance. Hence, this two-face design can make sure the measurement of the surface profile is possible. As shown in Fig.4.3 (a), when the face 1 is horizontal, the flat thin foil is horizontal as well. Then the surface profile could be measured. With the foil deformed gradually, the curvature of the foil increases largely, we can't obtain the whole profile with this horizontal mode, since measurement on the end part of the foil exceed the height limitation in Z-axis, as shown in Fig.4.3 (b). In this case, we can set the face 2 horizontally, i.e. rotate the whole rig by 12°, as shown in Fig.4.3 (c). The peak of the foil curvature changes into the middle part, i.e. both ends of the foil are lower than the middle but within the Z-axis limitation, then the whole surface profile information could be detected.

The rig and formers were manufactured by Geoff Gannaway and Geoff Simpson in the Workshops, School of Physics, Queen Mary University of London.

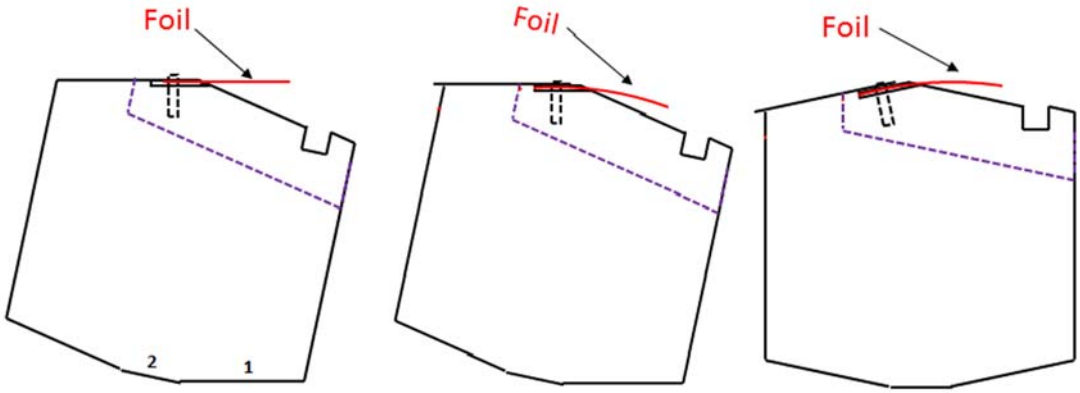


(a) (b) (c)

**Fig4.3 Schematic of the two face mode of the rig. In (a), the flat foil is measured horizontally. In (b), the whole profile couldn't be obtained since the measurement on the end of the foil exceed the height limitation. In (c), with the rotation of the rig, the full information could be obtained.**

### 4.2.2 Non-contact optical profilometer

The surface profiles of the designed experiments are measured by using a non-contact optical profilometer (OTM3 profilometer from Wolf & Beck Sensorik, Germany), shown in Fig.4.4 (a). The rig in 4.2.1 is designed to be mounted under this profilometer. Hence, the curvature of the foil could be measured without physical contact and without dismounting the foil from the rig. A schematic of the optical profilometer is shown in Fig.4.4 (b). When the light beam goes through the objective lens, the focal plane is formed. The position of the sample to be measured should be located in the focal plane. Hence, there is a measuring range of the sensor. The 3D coordinate is formed by the position on the X-Y plane and height distance. The surface morphology is recorded by the digital image sensor.

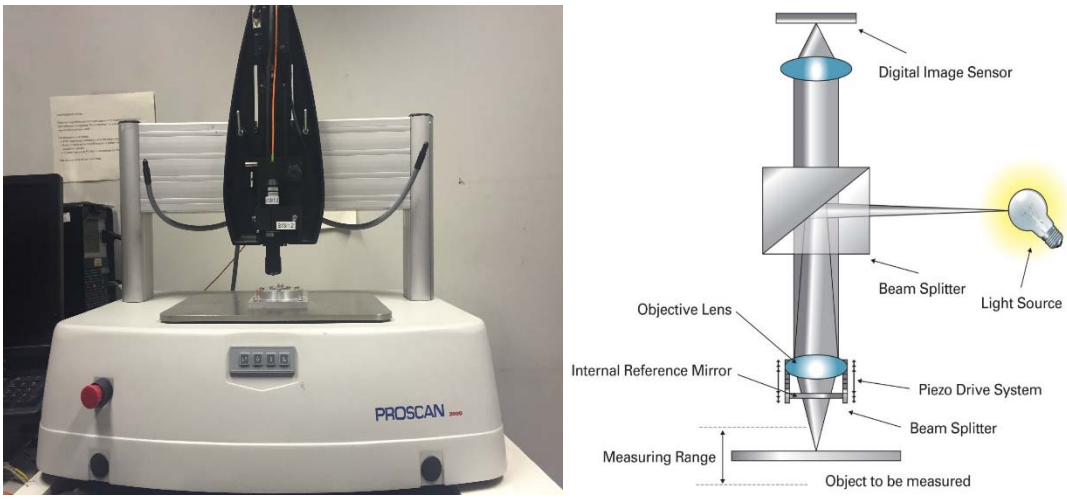


**(a)** **(b)**

**Fig.4.4 (a) The profilometer used in the surface profile measurement. (b) Schematic of the optical profilometer. There is a measuring range of profilometer. [99]**

### 4.2.3 Formers

In order to get complete data sets for the whole range (elastic section, the yield point and high plastic st rain section), a discrete and large range of radii of formers were designed, fabricated and measured, as shown in Table 4.1.

**Table 4.1. The nominal and measured radius of the former**

| No. | Nominal (mm) | Measured (mm) | Tolerance (mm) |
|---|---|---|---|
| 1 | 312.500 | 332.14 | ±0.208 |
| 2 | 250.000 | 261.236 | ±0.166 |
| 3 | 208.333 | 225.785 | ±0.182 |
| 4 | 156.250 | 159.113 | ±0.116 |
| 5 | 125.000 | 132.656 | ±0.187 |
| 6 | 104.167 | 105.115 | ±0.133 |
| 7 | 70.000 | 70.456 | ±0.088 |
| 8 | 50.000 | 50.126 | ±0.055 |
| 9 | 30.000 | 30.152 | ±0.034 |
| 10 | 20.000 | 20.398 | ±0.033 |
| 11 | 15.000 | 15.100 | ±0.800 |
| 12 | 10.000 | 10.100 | ±0.033 |
| 13 | 7.000 | 7.120 | ±0.033 |
| 14 | 4.167 | 4.214 | ±0.114 |
| 15 | 2.500 | 2.602 | ±0.033 |
| 16 | 2.083 | 2.131 | ±0.010 |
| 17 | 1.667 | 1.812 | ±0.024 |
| 18 | 1.250 | 1.327 | ±0.067 |
| 19 | 0.833 | 0.909 | ±0.016 |

Take the No.7# & No.14# Former as examples. We propose the nominal radius of No.7# is 70.000mm (low strain). The former is produced by Geoff Gannaway and Geoff Simpson in Workshop, School of Physics, Queen Mary University of London. I measure the surface profile of the produced former by optical profilometer. The profilometer does not calculate radius of curvature. It only measures and records the surface profile data. Hence, the data have to be exported from the software of the profilometer. The radius of curvature is obtained by fitting to the data by using the *Mathematica*© software, as shown in Fig.4.5 In (a), the 3D plot of the surface profile is illustrated. The former is mounted on the rig. The sensor scan the former along the X-axis. The steps of X-axis is scan length in mm. Each former is scanned 5 times produce 5 parallel lines with different Y-axis value. The Z-axis is the height of the surface profile in nm. Each line of the data is fitted by *Mathematica*© separately, as shown in (b). The light blue line is the measured surface profile data, while the red line from the fitting of *Mathematica*© software. Then the value of the radius can be obtained by the fitting value. The deviations of the fitting are checked as well, as shown in (c). The values of data points are subtracted from the value of fitting curvature. The deviations residuals of most data points are within 2μm. This check shows that the fitting to the curvature by the *Mathematica*© software is sufficiently precise. We repeat the same fitting procedure to the five scans. The average result is the final measured radius, and the tolerance is calculated as well, as shown in Table 1.

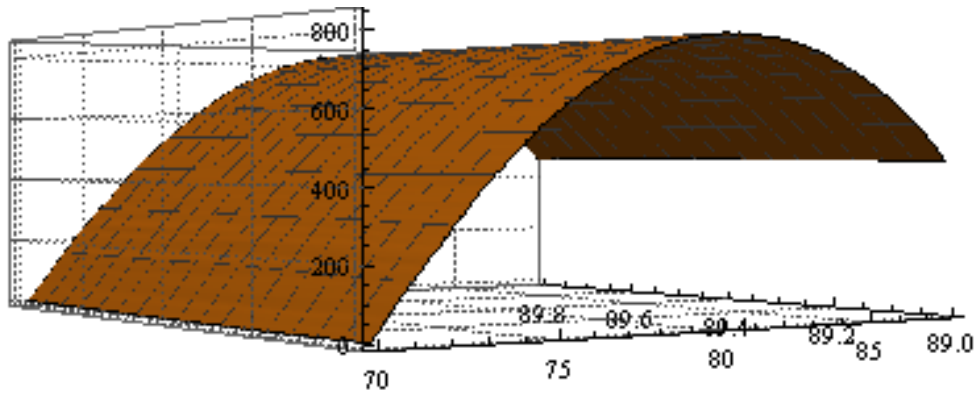


**(a)**

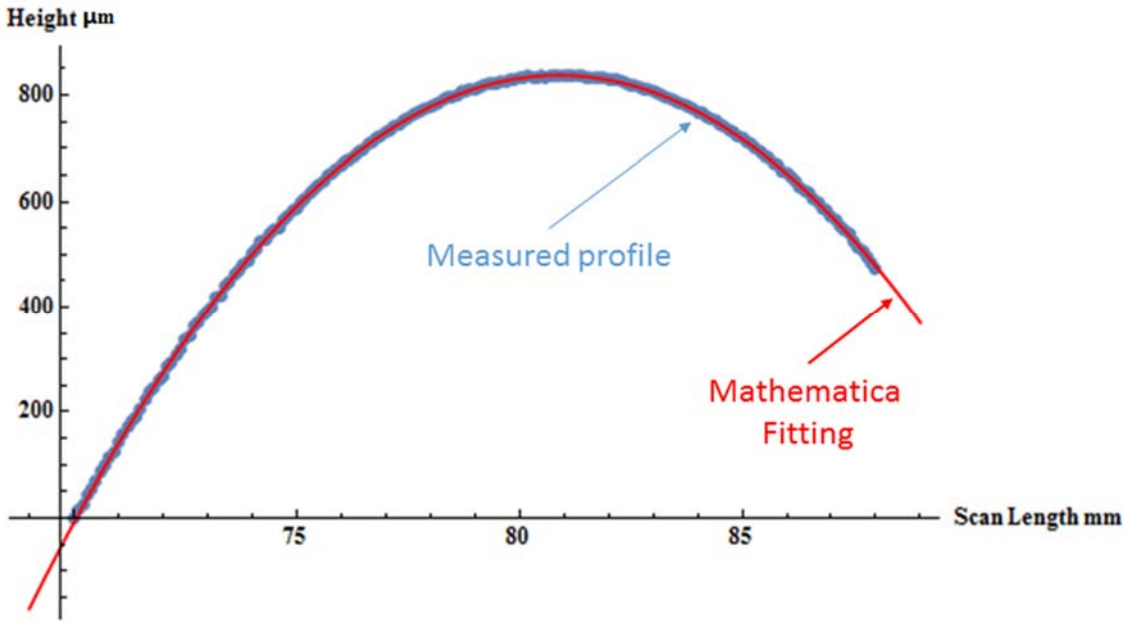


**(b)**

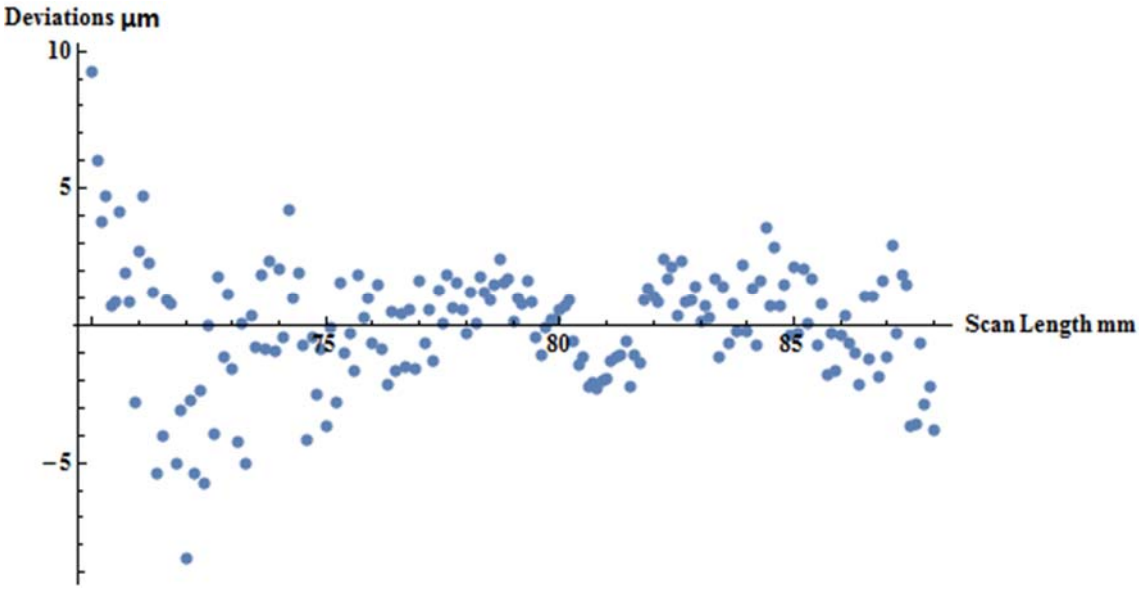


**(c)**

**Fig.4.5 (a) 3D plot of the surface profile of No.7# Former (low strain). X-axis is scan length in mm, Y-axis is the different scanned line, Z-axis is the height of the surface profile in μm. (b) Fitting of each line of data. The light blue line is the measured surface profile data, while the red line from the fitting of Mathematica© software. (c) The deviations check of the fitting demonstrates the fitting is relatively accurate.**

Fitting of the No.14# Former (high strain) is shown in Fig.4.6. The fitting process is exactly the same with No.7# Former. One more step is the cutting of the measured profile. Because the high strain former has a smaller radius, the whole measured profile is consist of one circle part and two tangent lines on each side of the circle. The fitting to the profile is focus on the circle component, two fitting tangent lines are used to determine the cutting range of the profile data.

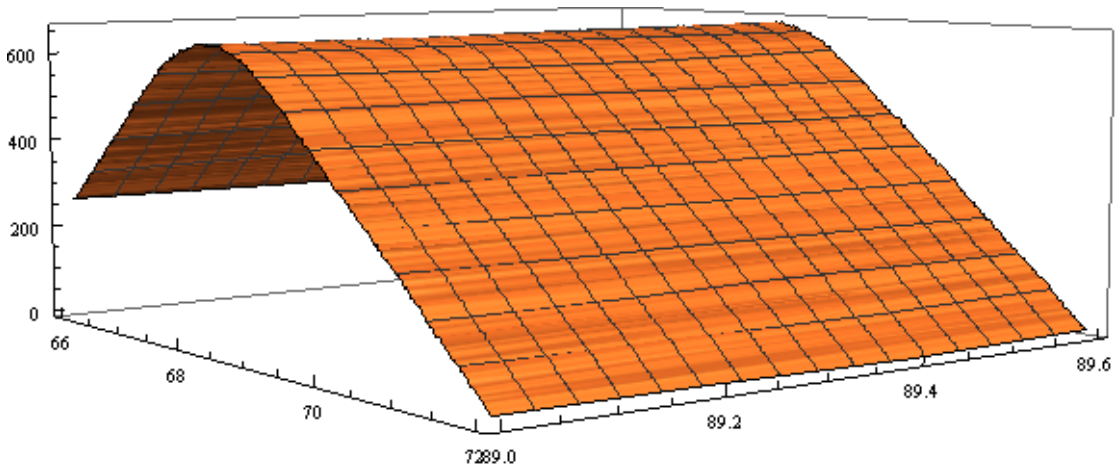


**(a)**

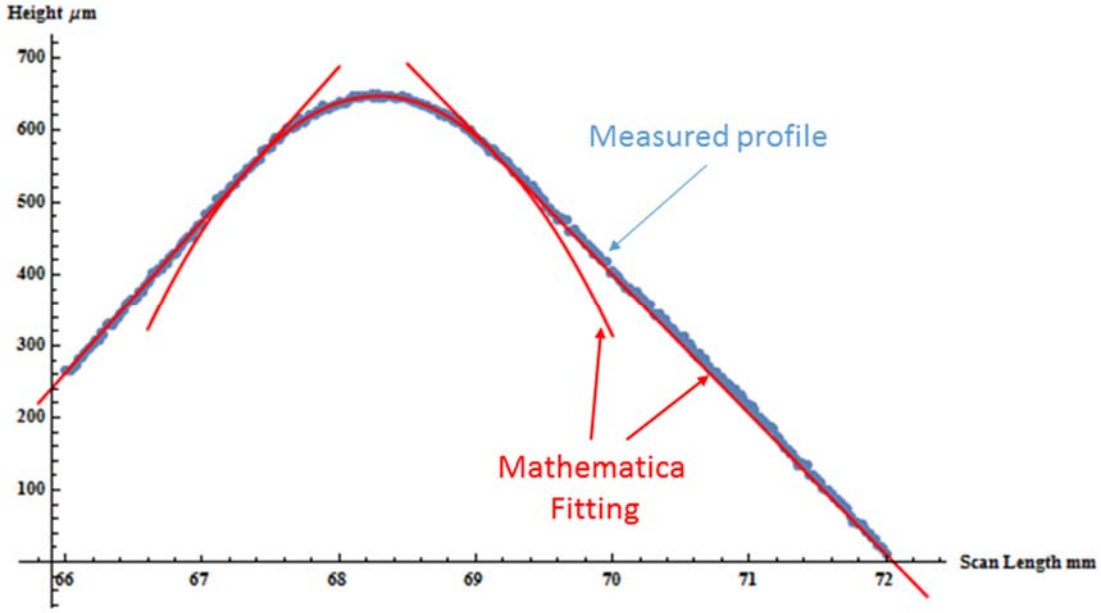


**(b)**

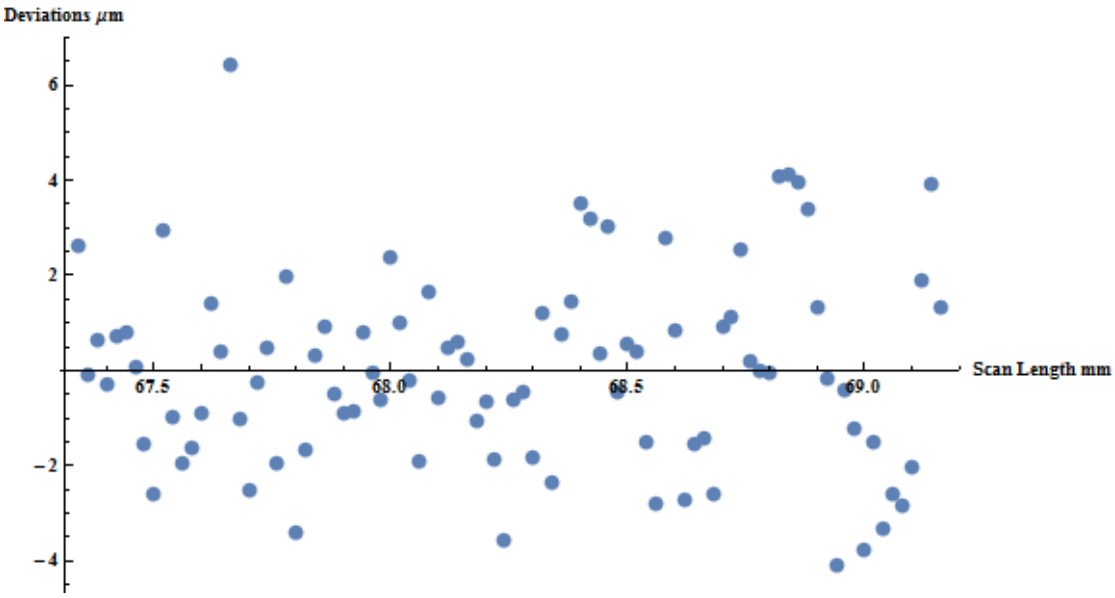


**(c)**

**Fig.4.6 The Mathematica fitting of the surface profile of No.14# Former (high strain). The fitting to the profile is focus on the circle component, two fitting tangent lines are used to determine the cutting range of the profile data.**

## 4.3 Experimental design

### 4.3.1 Rapid thermal anneal (RTA)

The rapid thermal anneal is used to modify the crystal structure and surface profile of the thin metal foils [100]. It was built and operated by school of physics, Queen Mary, University of London. A schematic of the RTA chamber is shown in Fig.4.7. The chamber can obtain a rough vacuum by using the vacuum pump. Nitrogen gas is supplied by the pipe under the chamber. Hence, the samples can be annealed in either vacuum environment or inert $N_2$ gas atmosphere to prevent oxidation of the samples. The annealing components consist of electric terminals and graphite carbon strips. There are screws on both side of the graphite carbon strips to fix them on the electric terminal. When annealing is in progress, the thin metal foil samples are sandwiched by two carbon strips, electric current raises the temperature of the resistive graphite strips.

A water cooling system prevents overheating of the electric terminal and the chamber. The monitoring feedback is achieved by the sapphire rod taking light to the pyrometer located under the graphite carbon strips and the electric terminal. This is used via a Proportional-Integral-Derivative (PID) to control the temperature of the graphite and samples. The accuracy of the control is ±1°C. A thermocouple is used for monitoring the temperature of the electric terminal and whole chamber to prevent overheating.

The whole annealing process is controlled by program and software. The software was written by Prof. Willian Gillin from school of physics, Queen Mary, University of London. The most significant ability of the RTA is rapid temperature rise slope. The duration of heating from room temperature to 1000°C is 15s. This capacity is fully important for small dimensions samples. In the traditional furnace, different diffusion rates of the surface and bulk material can produce a rough surface. RTA's shorter times and higher temperatures are expected to reduce surface roughening significantly.

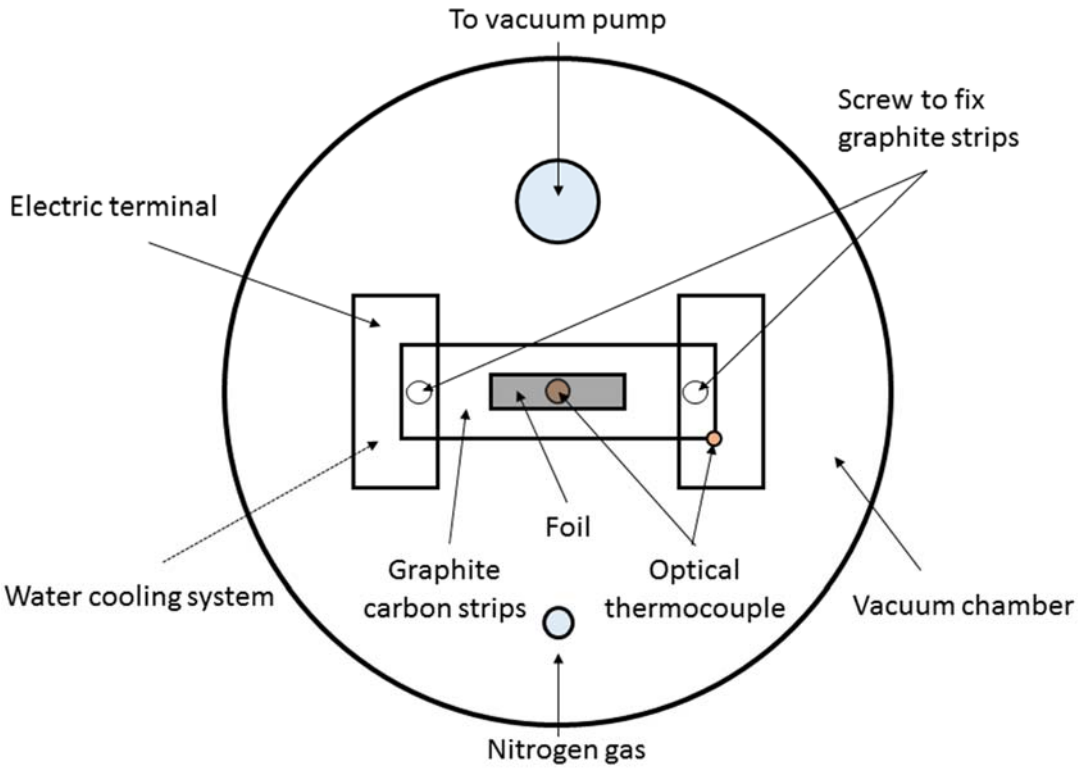


**Fig.4.7 Schematic of the main components of the RTA. The foil samples are placed between two graphite strips and the temperature is measured and controlled by optical thermocouple. The samples are annealed in either high vacuum environment or inert Nitrogen gas atmosphere to prevent oxidation.**

### 4.3.2 Micro-foil bending test method

We adopt load-unload micro-foil bending test method which was proposed by Stolken and Evans [8], as described in the literature review. The bending equipment are the new designed load-unload Formers Rig introduced in section 4.2. Schematic of the load-unload bending test process is shown in Fig.4.8. The metal foil is loaded round the former with rubber. We have known the former radius as introduced in Table 4.1. Here we assume the former radius is $R_1$. The width of the rubber and foil are exactly the same but slightly less than the middle of rig cover plate. Since the distance between the two stopping plate is calculated precisely to make sure the former and thin foil fully contact, we could consider that the load radius is the former radius $R_1$. The surface strain of the foil in the loaded state is then expressed by

$$\varepsilon_S = \frac{h}{2R_1} \tag{4.1}$$

where $\varepsilon_S$ is surface strain, $h$ is the thickness of the foil. In the fully loaded state, the stress contains both elastic and plastic component. The foil is then unloaded, it elastically recovers to a larger radius $R_2$. It contains only the plastic component of strain in the unload state together with residual internal stresses. The normalized bending moment is expressed as

$$M_n = \frac{Eh}{12}\left(\frac{1}{R_1} - \frac{1}{R_2}\right) \tag{4.2}$$

where $E$ is the Young's modulus of the material, $h$ is the thickness of the foil, $R_1$ is former radius and $R_2$ is relaxed foil radius in unload state.

By substituting the formers successively from large radius to smaller radius, this bending test can give brilliant data over a wide range of surface strain. We plot normalized moment versus strain. The whole range of strain from elasticity, yield to high plasticity of the foil can be obtained.

When the strain is too small to get plasticity, the foil will elastically recover to flat which means $R_2$ is $\infty$. In this case, $1/R_2$ is null and $M_n$ is expressed by

$$M_n = \frac{Eh}{12}\left(\frac{1}{R_1}\right) = \frac{E}{6}\frac{h}{2R_1} = \frac{E}{6}\varepsilon_S \tag{4.3}$$

Then the plot of the normalized moment versus strain is a straight line. The slope is a constant *E/6*. This straight line is the theoretical elastic line of the material.

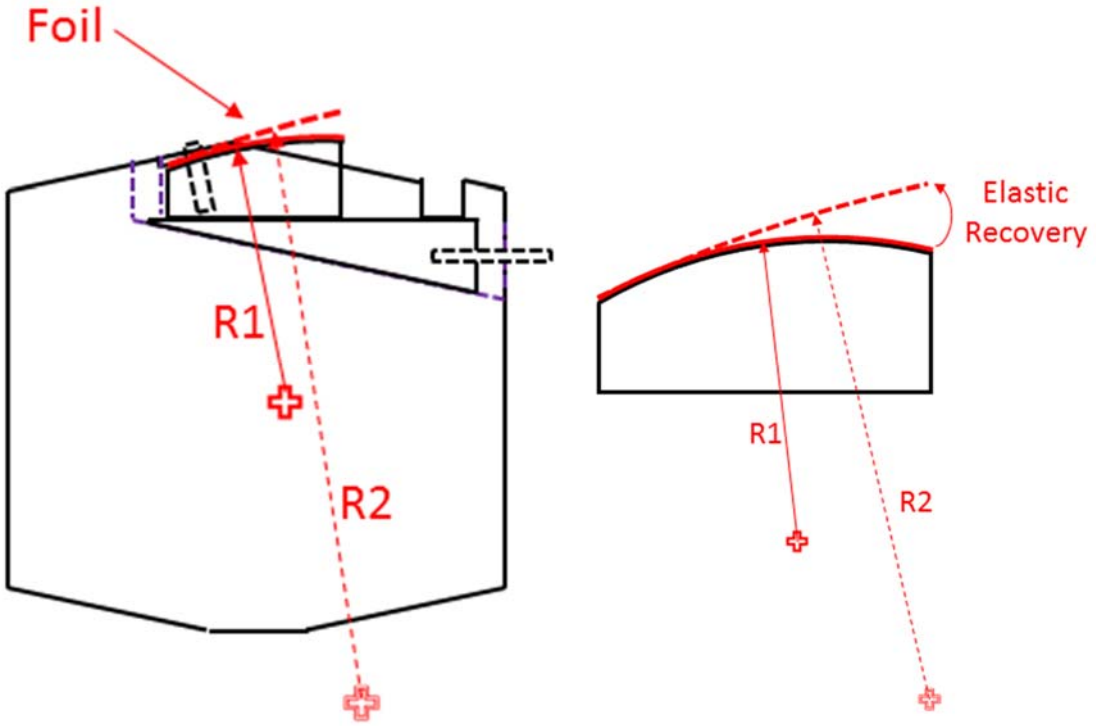


**(a)** **(b)**

**Fig.4.8 Schematic of the load-unload bending test process. (b) is the zoom in detail of the foil. Since the former and thin foil fully contact, load radius is the former radius $R_1$. The foil is then unloaded, it elastically recover to a larger radius $R_2$.**

# 4.4 Experimental procedure

## 4.4.1 Sample preparation

Nickel foils of three different thickness ($h$=10, 50 and 125 μm) were obtained from Goodfellows Cambridge Limited, UK, with purity of 99.9%. The 125 μm thickness foil was un-annealed rolled sheet, while the thinner foils were electrodeposited with very small grain size. Hence, the initial microstructure and grain size of the foils is

substantially different. We know that the strength of polycrystalline metals depends on the microstructure significantly. Therefore, the annealing process was used to modify the microstructure. Before the annealing and foil bending, the 5mm*20mm samples were cut from the original metal sheet by using a scalpel. Scissors can't be used for cutting, they will bend the foil samples because of the shearing involved. The samples were annealed by using the RTA described in section 4.3.1. The annealing process is in the inert nitrogen gas atmosphere with temperatures from 700-1000$^{o}$C. Annealing times from 15s to 900s are used to obtain different grain sizes.

After annealing, the foils were etched to show the grain size. The etching solution is a mixture of acetic and nitric acid with a ratio of 5 to 1. Because the etching process damages the foil, for each annealing process, we prepare two samples, one is used for the bending test while another one is for the grain size measurement.

### 4.4.2 Load-unload test

Before the load process, the initial radius of the foil was measured by profilometer. Then the largest radius of former was mounted and the foil was loaded by using a rubber. The load rubber was covered with clean plastic film to avoid sticking on the foil. The foil was then unloaded, the unload radius of the foil was also measured by profilometer. Next, the next smaller former was substituted, the repeat load-unload procedure was carried out to get the new unload radius. The measurement of the curvature of the foil was the same as for the formers as introduced in section 4.2.3.

## 4.5 Initial results

### 4.5.1 Grain size measurement

To test feasibility of the new experimental method, the nickel foil samples were prepared and annealed at the published data annealing conditions [98]. Some typical annealing conditions in the old data were adopted, as shown in table 4.2.

**Table 4.2. The typical annealing conditions and grain sizes on different thickness of the foils**

| No. | Thickness /μm | Annealing Temperature/ ºC | Annealing Time /s | Grain size /μm | Published data grain size/μm |
|---|---|---|---|---|---|
| (1) | 125 | 1000 | 5 | 76 | 85 |
| (2) | 50 | 1000 | 120 | 51.5 | 50 |
| (3) | 50 | 700 | 30 | 4.7 | 14 |
| (4) | 10 | 1000 | 300 | 20.4 | 12 |

The micro-structure of the samples were measured by SEM, the examples of SEM images are shown in Fig.4.9. The grain size measurements were adopted Average Grain Intercept (AGI) method [101, 102]. The results are illustrated in table 4.2. The initial grain sizes of the different thickness of the foils are various because the different fabrication method. The thickest foil (125μm) was un-annealed rolled sheet with large grains, while the thinner foils (50μm, 10μm) were electrodeposited with very small grains. Annealing results confirm the expectation that the grain growth rate of the 10μm foil is very slow, while 125μm foil grain growth rate is very fast.

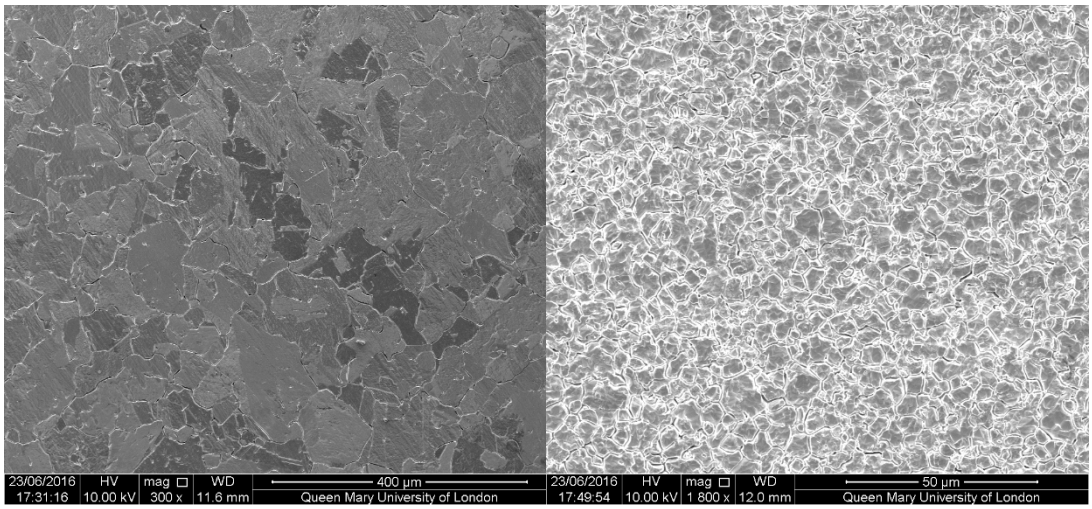


**(a)** **(b)**

**Fig.4.9 The examples of SEM images of the annealed Ni foil samples. (a) The 125μm thickness, annealing temperature 1000ºC, annealing time 5s. (b) The 50μm thickness, annealing temperature 700ºC, annealing time 30s.**

I compared the sample grain sizes of my data with the published data, which is shown in Table 4.2. Annealing the 125 μm (thickest) thickness foil at 1000ºC (high temperature) for 5s (short time) and the 50μm thickness sample at 1000ºC (high temperature) for 120s, my data corresponding well with the published data. The 50μm thickness foil annealed at 700ºC (low temperature) for 30s (short time), my data has a much smaller grain size than the published data, while the 10μm (thinnest) thickness foil annealed at 1000ºC (high temperature) for 300s (long time), my data has a larger grain size than the expected value. The results show that sample annealed at the lower temperature and less time has a smaller grain sizes, while the higher temperature and more annealing time sample has a larger grain than the expected values. I attribute this difference results to the temperature feedback and control system of the RTA.

## 4.5.2 Curvature measurement

The curvature of the unload foils were measured by non-contact optical profilometer. The sample rate of the sensor is 300MHz, the scan rate is 0.02mm in X-axis and 0.2mm in Y-axis. Take the 50μm thickness foil annealed at 1000ºC for 120s as an example, the load radius is 4.214 mm. The foil was deformed in the high strain and then unloaded. The measured unload surface profile is shown in Fig.4.10. X-axis is the scan length of the sample in mm, Y-axis is different scan of the sample. The profile of the sample is represented by Z-axis in micron. The smooth surface profile of the sample explains the load-unload process is relatively good. The data is qualified for the fitting of the curvature. The fitting process has been introduced in Section 4.2.3.

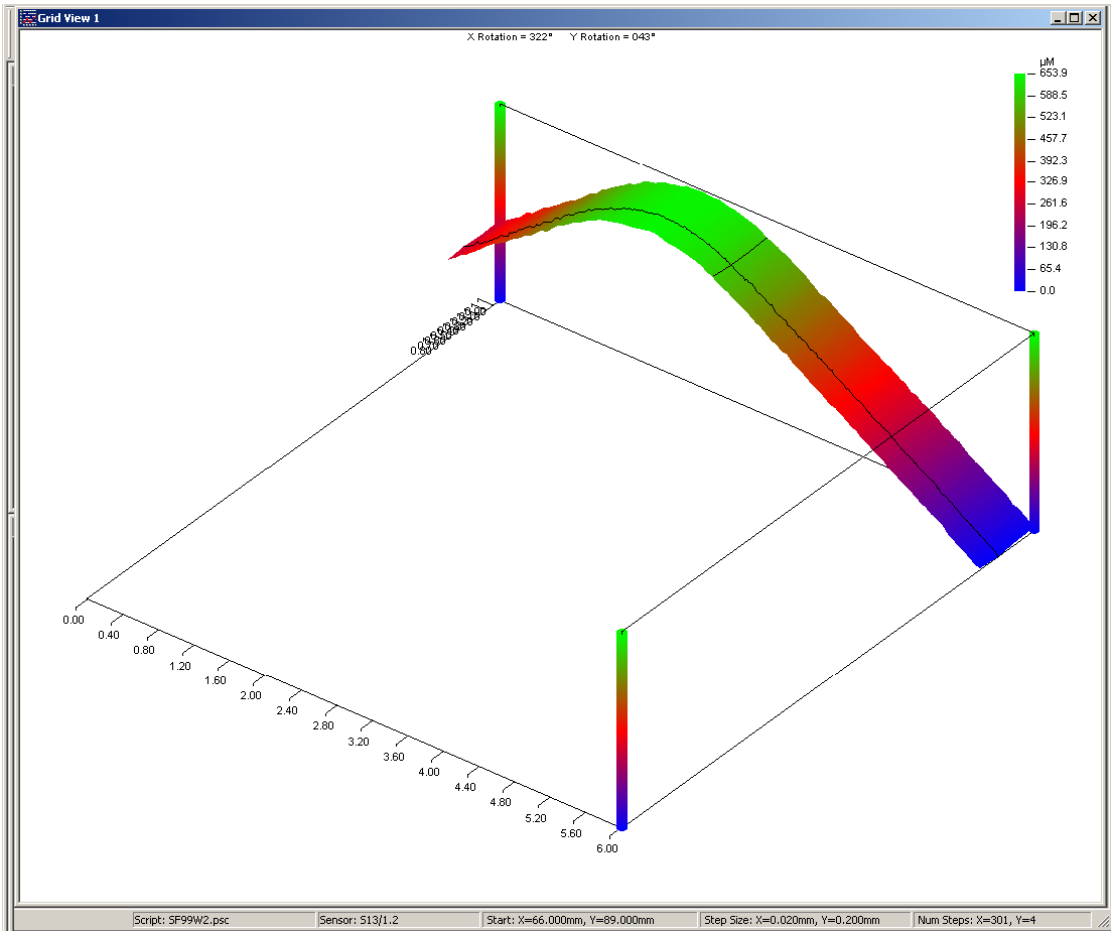


**Fig.4.10 The measured surface profile of the unload sample. X-axis is the scan length of the sample in mm, Y-axis is different scan of the sample. Z-axis represented the profile in micron.**

### 4.5.3 Mechanical property

The surface strain and the normalized bending moment of the samples were calculated by Eq.4.1 & Eq.4.2. The mechanical tests results were shown in Fig.4.11 (a), (b). The normalized bending moment was plotted against the surface strain. Fig.4.11 (b) expands the small strain region, then we can observe more detail clearly from Fig.4.11 (b). Before the load process, the curvature of flat foil was measured (very large but is a specific value), which is called un-deformed curvature. During the load process under very large radii formers, the foil is recovered to its initial un-deformed curvature. We define this behaviour as elastic deformation. The blue line in the Fig.4.11 is the elastic modulus line calculated by the young's modulus of Ni. When the curvature of the unload radius $R_2$ is smaller than initial un-deformed curvature, the foil displays plasticity. In this figure, the red data is my new data, the blue data is the old published data. The red data points are much more numerous than the blue data points, because the radii of formers are designed fully covered the whole region of the bending test. From Fig.4.11b, we can find that there are no old data points around the onset of plastic deformation, while the new data points covered that region. In the elastic-plastic transition region, the new data points can display more detail behaviour, hence, the more accurate results about the yield points will be obtained.

Generally, the new datasets are corresponding well with the published old data. The thickest 125μm foils (Symbol: Cross) are very weak and have already yielded at the largest former radius. The size effect is observed clearly when the sample thicknesses decreased below 50μm. The 50μm thickness sample is stronger than the 10μm thickness samples in this figure, because the very small grain size. One abnormal dataset is red triangle samples (50μm thickness and 52μm grain size). It is much weak than the expected behaviour. I cannot explain this dataset, it is attribute to the experimental operations. This dataset should be repeated.

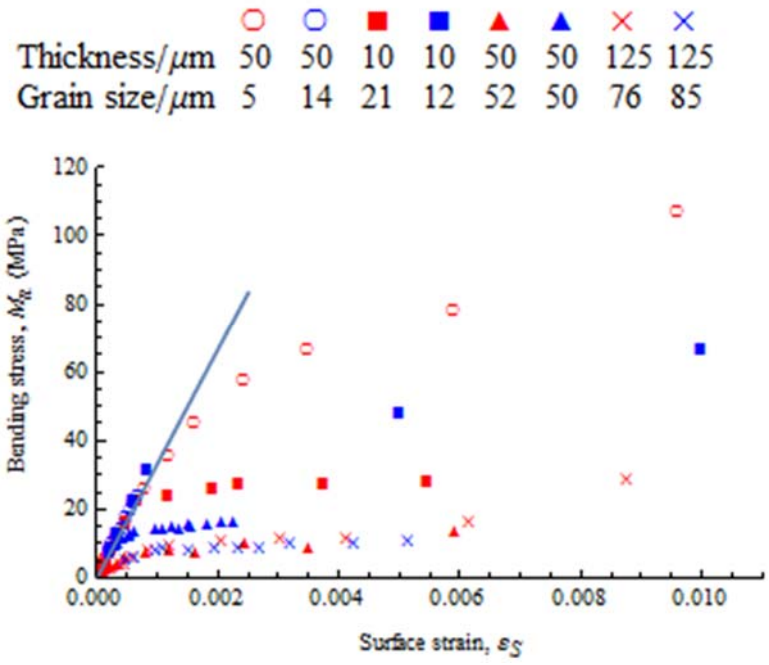


**(a)**

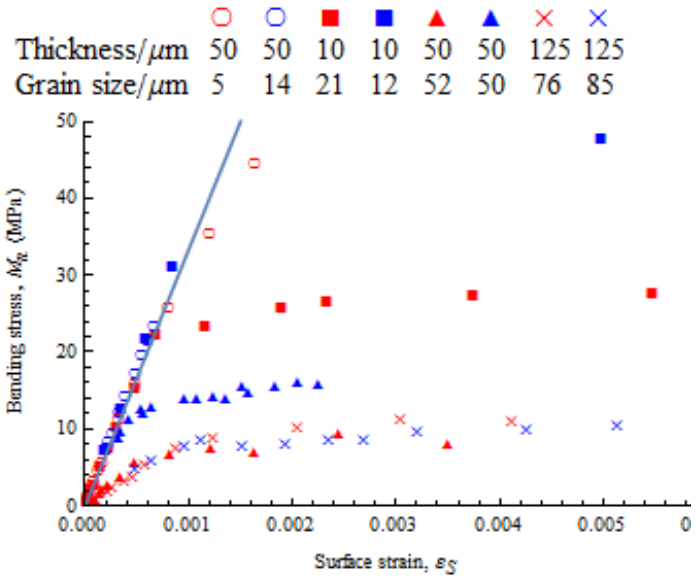


**(b)**

**Fig.4.11 (a) The normalized bending moment was plotted against the surface strain. The red data is the new data, the blue data is the old published data. The sample thicknesses of filled squares, circle, triangle and cross are 10μm, 50μm, 50μm and 125μm, respectively. Thinner foils are stronger than thicker foils.**

## 4.6 Future work

It is clear that this new designed load-unload formers bending method works well. There are two main works needed to be done in the future with the new method and rig:

(1) It is necessary to obtain more datasets of pure metal samples contain various grain sizes and thicknesses to complete the datasets. Because the new rig can produce more testing data points, the detail information around yield point will display. The grain size effect theories could be tested with more accurate data.

(2) To test the SGP theory, the sandwich structure samples will be fabricated and be tested with the new rig. The sandwich structure samples will be made by gluing pairs of foils together with paper between them. The paper is soft which can barely affect the strength of the whole samples. Hence, by adjusting the thickness of the paper between the foils, we can obtain the sandwich structure samples with various foil thicknesses but with a fixed sample thickness. This sample design make it possible to separate the effects of size and of strain gradient. Then the SGP theory will be tested by this new experimental design. The new rig will provide more accurate results.

## 4.7 Conclusion

In this new load-unload former equipment, the un-deformed thin metal foil is mounted only once. During the whole load-unload process, the foil sample is fixed on the rig and measured by non-contact optical profilometer. The precise design of the rig can make sure that the former and foil are fully contacted during the load process. Only the former substitution is done before each new load-unload operation. Compare to the traditional mandrel method equipment, this new method eliminates the complex operations of mounting and dismounting the foil between each measurement. Repeated handling

risks deforming the foil itself; the new method avoids the unnecessary handling of the sample and make sure that more accurate data could be obtained.

We designed and made the large number of formers which the radii ranging from more than 300 mm (even flat) to less than 1mm (quite high strain). By substituting different formers, we can get the discrete data from the elastic region through the yield point and to high plastic strain area, i.e. the whole region information of deformed foil can be obtained. More testing data points around the elastic-plastic transition region can reveal the yield behaviour.

It is clear that the initial results from the new designed load-unload formers bending method corresponding well with the published data. The initial results test the feasibility of the new experimental method. The new experimental device create a good foundation for future mechanical property testing experiments.

# 5. Summary

Generally, there are two main sections in this thesis. The first section is a comprehensive review on the Hall-Petch relationship. The second section is a new experimental design on micro-foil bending test. I will summarize the conclusions separately below.

Firstly, in total, 61 typical Hall-Petch datasets were collected from the classic references. These datasets included all of the general metals. They were digitized and fitted with the Hall-Petch equation (both $\sigma_0$ and $k_{HP}$ treated as free fitting parameters), free exponent of Hall-Petch equation and dislocation curvature equation. The scaling exponent values are scatted from 0 to 1. There is no rigorous inverse square-root power law on Hall-Petch relationship. We summarized the $k_{HP}$ values of these 61 datasets. They are widely scattered even for a single metal, hence, Hall-Petch equation is not qualified as an empirical formula for predicting the material mechanical behaviour. The four classic models all fail to predict the parameter $k_{HP}$. The data fit both Hall-Petch and dislocation curvature equations equally well, but the fully Bayesian analysis strongly supports the latter. There is a trend that the smaller grain sizes have a higher value of the $k_{HP}$. This is evidence that the dislocation curvature equation is correct. We conclude that the Hall-Petch effect is not a special behaviour with its own unique parameters. Actually, it is another manifestation of the general size effect.

Secondly, on micro-foil bending test, we designed and fabricated a new device based on the classic load-unload method. Because the thin foils are soft and fragile, repeated handling in classic experimental design deformed the foil to some extent. Repeated operations of mounting the foil risk error of the data. The brilliant design of the new equipment is that the foil sample is mounted only once before the mechanical testing process. The new devices overcome the difficulty for obtaining accurate data. Our initial results show that the new device worked well. We made a large number of formers which the radii covered the gap between the elastic and plastic strain. Hence, in the elastic-plastic transition region, the new device can produce more testing data points to show the yield strain and stress clearly. The new datasets contains more data

points with smaller error bar which make it possible to test the Hall-Petch and SGP theories precisely in the further work.

# Publications

Li Y, Bushby AJ, Dunstan DJ. The Hall–Petch effect as a manifestation of the general size effect. Proc R Soc A: The Royal Society; 2016. p. 20150890.

Li Y, Bushby AJ, Dunstan DJ. Quantitative explanation of the reported values of the Hall-Petch parameter. Acta Materialia, submitted

# References

[1] Zhu TT, Bushby AJ, Dunstan DJ. Materials mechanical size effects: a review. Materials Technology. 2008;23:193-209.
[2] Ashby MF. The deformation of plastically non-homogeneous materials. Philosophical Magazine. 1970;21:399-424.
[3] Taylor GI. The mechanism of plastic deformation of crystals. Part I. Theoretical. Proceedings of the Royal Society of London Series A, Containing Papers of a Mathematical and Physical Character. 1934;145:362-87.
[4] Fleck NA, Muller GM, Ashby MF, Hutchinson JW. Strain gradient plasticity: theory and experiment. Acta Metallurgica et Materialia. 1994;42:475-87.
[5] Bragg W. A theory of the strength of metals. Nature. 1942;149:511-3.
[6] Liu D, He Ym, Tang X, Ding H, Hu P, Cao P. Size effects in the torsion of microscale copper wires: Experiment and analysis. Scripta Materialia. 2012;66:406-9.
[7] Liu D, He Ym, Dunstan DJ, Zhang B, Gan Z, Hu P, et al. Anomalous plasticity in the cyclic torsion of micron scale metallic wires. Physical Review Letters. 2013;110:244301.
[8] Stölken JS, Evans AG. A microbend test method for measuring the plasticity length scale. Acta Materialia. 1998;46:5109-15.
[9] Spary IJ, Bushby AJ, Jennett NM. On the indentation size effect in spherical indentation. Philosophical Magazine. 2006;86:5581-93.
[10] Xu L, Pang JH. Nano-indentation characterization of Ni–Cu–Sn IMC layer subject to isothermal aging. Thin Solid Films. 2006;504:362-6.
[11] Zong Z, Lou J, Adewoye O, Elmustafa A, Hammad F, Soboyejo W. Indentation size effects in the nano-and micro-hardness of fcc single crystal metals. Materials Science and Engineering: A. 2006;434:178-87.
[12] Fleck NA, Hutchinson JW. A phenomenological theory for strain gradient effects in plasticity. Journal of the Mechanics and Physics of Solids. 1993;41:1825-57.
[13] Begley MR, Hutchinson JW. The mechanics of size-dependent indentation. Journal of the Mechanics and Physics of Solids. 1998;46:2049-68.
[14] Rinaldi A, Peralta P, Friesen C, Sieradzki K. Sample-size effects in the yield behavior of nanocrystalline nickel. Acta Materialia. 2008;56:511-7.
[15] Kiener D, Motz C, Schöberl T, Jenko M, Dehm G. Determination of mechanical properties of copper at the micron scale. Advanced Engineering Materials. 2006;8:1119-25.
[16] Volkert CA, Lilleodden ET. Size effects in the deformation of sub-micron Au columns. Philosophical Magazine. 2006;86:5567-79.
[17] Greer JR, Oliver WC, Nix WD. Size dependence of mechanical properties of gold at the micron scale in the absence of strain gradients. Acta Materialia. 2005;53:1821-30.
[18] Gladman T. Precipitation hardening in metals. Materials Science and Technology. 1999;15:30-6.

[19] Wei L, Dunlop G, Westengen H. Precipitation hardening of Mg-Zn and Mg-Zn-RE alloys. Metallurgical and Materials Transactions A. 1995;26:1705-16.
[20] Afrin N, Chen D, Cao X, Jahazi M. Strain hardening behavior of a friction stir welded magnesium alloy. Scripta Materialia. 2007;57:1004-7.
[21] Del Valle J, Carreño F, Ruano OA. Influence of texture and grain size on work hardening and ductility in magnesium-based alloys processed by ECAP and rolling. Acta Materialia. 2006;54:4247-59.
[22] Hall EO. The deformation and ageing of mild steel: II characteristics of the lüders deformation. Proceedings of the Physical Society Section B. 1951;64:742.
[23] Petch NJ. The cleavage strength of polycrystals. J Iron Steel Inst. 1953;174:25-8.
[24] Eshelby JD, Frank FC, Nabarro F. XLI. The equilibrium of linear arrays of dislocations. The London, Edinburgh, and Dublin Philosophical Magazine and Journal of Science. 1951;42:351-64.
[25] Conrad H, Jung K. Effect of grain size from millimeters to nanometers on the flow stress and deformation kinetics of Ag. Materials Science and Engineering: A. 2005;391:272-84.
[26] Keller C, Hug E. Hall–Petch behaviour of Ni polycrystals with a few grains per thickness. Materials Letters. 2008;62:1718-20.
[27] Hansen N. The effect of grain size and strain on the tensile flow stress of aluminium at room temperature. Acta Metallurgica. 1977;25:863-9.
[28] Hansen N, Ralph B. THE STRAIN AND GRAIN-SIZE DEPENDENCE OF THE FLOW-STRESS OF COPPER. Acta Metallurgica. 1982;30:411-7.
[29] Aldrich JW, Armstrong.R.W. GRAIN SIZE DEPENDENCE OF YIELD, FLOW AND FRACTURE STRESS OF COMMERCIAL PURITY SILVER. Metallurgical Transactions. 1970;1:2547-&.
[30] Narutani T, Takamura J. GRAIN-SIZE STRENGTHENING IN TERMS OF DISLOCATION DENSITY MEASURED BY RESISTIVITY. Acta Metallurgica et Materialia. 1991;39:2037-49.
[31] Evans AG, Hutchinson JW. A critical assessment of theories of strain gradient plasticity. Acta Materialia. 2009;57:1675-88.
[32] Dunstan DJ, Bushby AJ. Theory of deformation in small volumes of material. Proceedings of the Royal Society a-Mathematical Physical and Engineering Sciences. 2004;460:2781-96.
[33] Nye J. Some geometrical relations in dislocated crystals. Acta Metallurgica. 1953;1:153-62.
[34] Arsenlis A, Parks DM. Crystallographic aspects of geometrically-necessary and statistically-stored dislocation density. Acta Mater. 1999;47:1597-611.
[35] Nix WD, Gao HJ. Indentation size effects in crystalline materials: A law for strain gradient plasticity. Journal of the Mechanics and Physics of Solids. 1998;46:411-25.
[36] Frank F, Van der Merwe J. One-dimensional dislocations. II. Misfitting monolayers and oriented overgrowth. Proceedings of the Royal Society of London A: Mathematical, Physical and Engineering Sciences: The Royal Society; 1949. p. 216-25.
[37] Matthews JW, Mader S, Light TB. ACCOMMODATION OF MISFIT ACROSS INTERFACE TEBWEEN CRYSTALS OF SEMICONDUCTING ELEMENTS OR

COMPOUNDS. Journal of Applied Physics. 1970;41:3800-&.
[38] Matthews J, Crawford J. Accomodation of misfit between single-crystal films of nickel and copper. Thin Solid Films. 1970;5:187-98.
[39] Dunstan DJ. Strain and strain relaxation in semiconductors. Journal of Materials Science-Materials in Electronics. 1997;8:337-75.
[40] Fitzgerald E. Dislocations in strained-layer epitaxy: theory, experiment, and applications. Materials science reports. 1991;7:87-142.
[41] Adams AR. Strained-Layer Quantum-Well Lasers. Ieee Journal of Selected Topics in Quantum Electronics. 2011;17:1364-73.
[42] O'Reilly EP. Valence band engineering in strained-layer structures. Semiconductor Science and Technology. 1989;4:121.
[43] Cordero ZC, Knight BE, Schuh CA. Six decades of the Hall–Petch effect – a survey of grain-size strengthening studies on pure metals. International Materials Reviews. 2016;61:495-512.
[44] Hall EO. The deformation and ageing of mild steel: III discussion of results. Proceedings of the Physical Society Section B. 1951;64:747.
[45] Li Y, Bushby AJ, Dunstan DJ. The Hall–Petch effect as a manifestation of the general size effect. Proceedings of the Royal Society A: Mathematical, Physical and Engineering Science. 2016;472.
[46] Antolovich SD, Armstrong RW. Plastic strain localization in metals: origins and consequences. Progress in Materials Science. 2014;59:1-160.
[47] Cottrell AH, Bilby B. Dislocation theory of yielding and strain ageing of iron. Proceedings of the Physical Society Section A. 1949;62:49.
[48] Li J, Chou Y. The role of dislocations in the flow stress grain size relationships. Metallurgical and Materials Transactions. 1970;1:1145-59.
[49] Li JC. Petch relation and grain boundary sources. Transactions of the Metallurgical Society of AIME. 1963;227:239-&.
[50] Murr L. Some observations of grain boundary ledges and ledges as dislocation sources in metals and alloys. Metallurgical Transactions A. 1975;6:505-13.
[51] Cotterell A. Dislocation and plastic flow in crystals. 1953.
[52] Conrad H. Effect of grain size on the lower yield and flow stress of iron and steel. Acta Metallurgica. 1963;11:75-7.
[53] Conrad H, Feuerstein S, Rice L. Effects of grain size on the dislocation density and flow stress of niobium. Materials Science and Engineering. 1967;2:157-68.
[54] Chia KH, Jung K, Conrad H. Dislocation density model for the effect of grain size on the flow stress of a Ti-15.2 at.% Mo beta-alloy at 4.2-650 K. Materials Science and Engineering a-Structural Materials Properties Microstructure and Processing. 2005;409:32-8.
[55] Hirth JP. The influence of grain boundaries on mechanical properties. Metallurgical Transactions. 1972;3:3047-67.
[56] Meyersm MA, Ashworth E. A model for the effect of grain size on the yield stress of metals. Philosophical Magazine A. 1982;46:737-59.
[57] Dunstan DJ, Bushby AJ. The scaling exponent in the size effect of small scale plastic deformation. International Journal of Plasticity. 2013;40:152-62.

[58] Dunstan DJ, Bushby AJ. Grain size dependence of the strength of metals: The Hall–Petch effect does not scale as the inverse square root of grain size. International Journal of Plasticity. 2014;53:56-65.
[59] Aghaie-Khafri M, Honarvar F, Zanganeh S. Characterization of grain size and yield strength in AISI 301 stainless steel using ultrasonic attenuation measurements. Journal of Nondestructive Evaluation. 2012;31:191-6.
[60] Rhines FN. Geometry of grain boundaries. Metallurgical and Materials Transactions. 1970;1:1105-20.
[61] Griffith AA. The phenomena of rupture and flow in solids. Philosophical transactions of the royal society of london Series A, containing papers of a mathematical or physical character. 1921;221:163-98.
[62] Armstrong RW, Codd I, Douthwaite RM, Petch NJ. The plastic deformation of polycrystalline aggregates. Philosophical Magazine. 1962;7:45-58.
[63] Taylor GI. Analysis of plastic strain in a cubic crystal. Stephen Timoshenko 60th Anniversary Volume. 1938:218-24.
[64] Douthwaite RM. RELATIONSHIP BETWEEN HARDNESS, FLOW STRESS, AND GRAIN SIZE OF METALS. Journal of the Iron and Steel Institute. 1970;208:265-+.
[65] Douthwaite RM, Evans JT. Microstrain in polycrystalline aggregates. Acta Metallurgica. 1973;21:525-30.
[66] Kashyap BP, Tangri K. Hall-Petch relationship and substructural evolution in boron containing type 316L stainless steel. Acta Materialia. 1997;45:2383-95.
[67] Bassett W, Davis C. Comparison of grain size measurements and Brinell hardness of cartridge brass. Trans AIME. 1919;60:428-57.
[68] Babyak W, Rhines F. The relationship between the boundary area and hardness of recrystallized cartridge brass. Trans Metall Soc AIME. 1960;218:21-3.
[69] Jindal PC, Armstrong RW. The dependence of the hardness of cartridge brass on grain size. AIME MET SOC TRANS. 1967;239.
[70] Armstrong RW, Elban WL. Hardness properties across multiscales of applied loads and material structures. Materials Science and Technology. 2012;28:1060-71.
[71] Mathewson CH. Trans TMS-AIME. 1919;60:451.
[72] Feltham P, Meakin J. On the mechanism of work hardening in face-centred cubic metals, with special reference to polycrystalline copper. Philosophical Magazine. 1957;2:105-12.
[73] Hansen N, Ralph B. The strain and grain size dependence of the flow stress of copper. Acta Metallurgica. 1982;30:411-7.
[74] Vashi UK, Armstrong RW, Zima GE. The hardness and grain size of consolidated fine tungsten powder. Metallurgical Transactions. 1970;1:1769-71.
[75] Brittain CP, Armstrong RW, Smith GC. Hall-Petch dependence for ultrafine grain size electrodeposited chromium. Scripta Metallurgica. 1985;19:89-91.
[76] Hu H, Cline R. Mechanism of reorientation during recrystallization of polycrystalline titanium. Trans Met Soc AIME. 1968;242.
[77] Jones R, Conrad H. THE EFFECT OF GRAIN SIZE ON THE STRENGTH OF ALPHA- TITANIUM AT ROOM TEMPERATURE. Trans Met Soc AIME.

1969;245:779-89.
[78] Emery RD, Povirk GL. Tensile behavior of free-standing gold films. Part I. Coarse-grained films. Acta Materialia. 2003;51:2067-78.
[79] Thompson AW. Effect of grain size on work hardening in nickel. Acta Metallurgica. 1977;25:83-6.
[80] Keller C, Hug E. Hall-Petch behaviour of Ni polycrystals with a few grains per thickness. Materials Letters. 2008;62:1718-20.
[81] Carreker RPH, W.R. Wright Air Development Center Technical Report. 1955:55.
[82] Tsuji N, Ito Y, Saito Y, Minamino Y. Strength and ductility of ultrafine grained aluminum and iron produced by ARB and annealing. Scripta Materialia. 2002;47:893-9.
[83] Yu CY, Kao PW, Chang CP. Transition of tensile deformation behaviors in ultrafine-grained aluminum. Acta Materialia. 2005;53:4019-28.
[84] Brown L. Indentation size effect and the Hall-Petch 'Law'. Materials Science Forum: Trans Tech Publ; 2011. p. 13-26.
[85] Kocks U. Laws for work-hardening and low-temperature creep. Journal of engineering materials and technology. 1976;98:76-85.
[86] Rosenberg J, Piehler H. Calculation of the Taylor factor and lattice rotations for bcc metals deforming by pencil glide. Metallurgical Transactions. 1971;2:257-9.
[87] Balint D, Deshpande V, Needleman A, Van der Giessen E. Discrete dislocation plasticity analysis of the grain size dependence of the flow strength of polycrystals. International Journal of Plasticity. 2008;24:2149-72.
[88] Lim H, Lee M, Kim J, Adams B, Wagoner R. Simulation of polycrystal deformation with grain and grain boundary effects. International Journal of Plasticity. 2011;27:1328-54.
[89] Lim H, Subedi S, Fullwood D, Adams B, Wagoner R. A Practical Meso-Scale Polycrystal Model to Predict Dislocation Densities and the Hall–Petch Effect. Materials Transactions. 2014;55:35-8.
[90] Berger JO. Statistical decision theory and Bayesian analysis: Springer Science & Business Media; 2013.
[91] Schiøtz J, Vegge T, Di Tolla F, Jacobsen KW. Atomic-scale simulations of the mechanical deformation of nanocrystalline metals. Physical Review B. 1999;60:11971.
[92] Wolf D, Yamakov V, Phillpot S, Mukherjee A. Deformation mechanism and inverse Hall–Petch behavior in nanocrystalline materials. Zeitschrift Fur Metallkunde. 2003;94:1091-7.
[93] Phaniraj M, Prasad M, Chokshi A. Grain-size distribution effects in plastic flow and failure. Materials Science and Engineering: A. 2007;463:231-7.
[94] Conrad H, Jung K. Effect of grain size from millimeters to nanometers on the flow stress and deformation kinetics of Ag. Materials Science and Engineering a-Structural Materials Properties Microstructure and Processing. 2005;391:272-84.
[95] Chia K-H, Jung K, Conrad H. Dislocation density model for the effect of grain size on the flow stress of a Ti–15.2 at.% Mo β-alloy at 4.2–650K. Materials Science and Engineering: A. 2005;409:32-8.
[96] Kelly A. Strong solids. 84 Oxford , UK: Clarendon Press. 1966.

[97] Dunstan DJ, Ehrler B, Bossis R, Joly S, P'ng KMY, Bushby AJ. Elastic limit and strain hardening of thin wires in torsion. Physical Review Letters. 2009;103:155501.
[98] Moreau P, Raulic M, P'ng* KMY, Gannaway G, Anderson P, Gillin WP, et al. Measurement of the size effect in the yield strength of nickel foils. Philosophical Magazine Letters. 2005;85:339-43.
[99] Wyant JC, Koliopoulos CL, Bhushan B, George OE. An optical profilometer for surface characterization of magnetic media. ASLE transactions. 1984;27:101-13.
[100] Wee S, Chai M, Homewood K, Gillin W. The activation energy for GaAs/AlGaAs interdiffusion. Journal of Applied Physics. 1997;82:4842-6.
[101] Thompson AW. Calculation of true volume grain diameter. Metallography. 1972;5:366-9.
[102] Han J-H, Kim D-Y. Determination of three-dimensional grain size distribution by linear intercept measurement. Acta Materialia. 1998;46:2021-8.